Submerged floating tunnel

The dynamic response due to fluid structure interaction

Mart-Jan Hemel
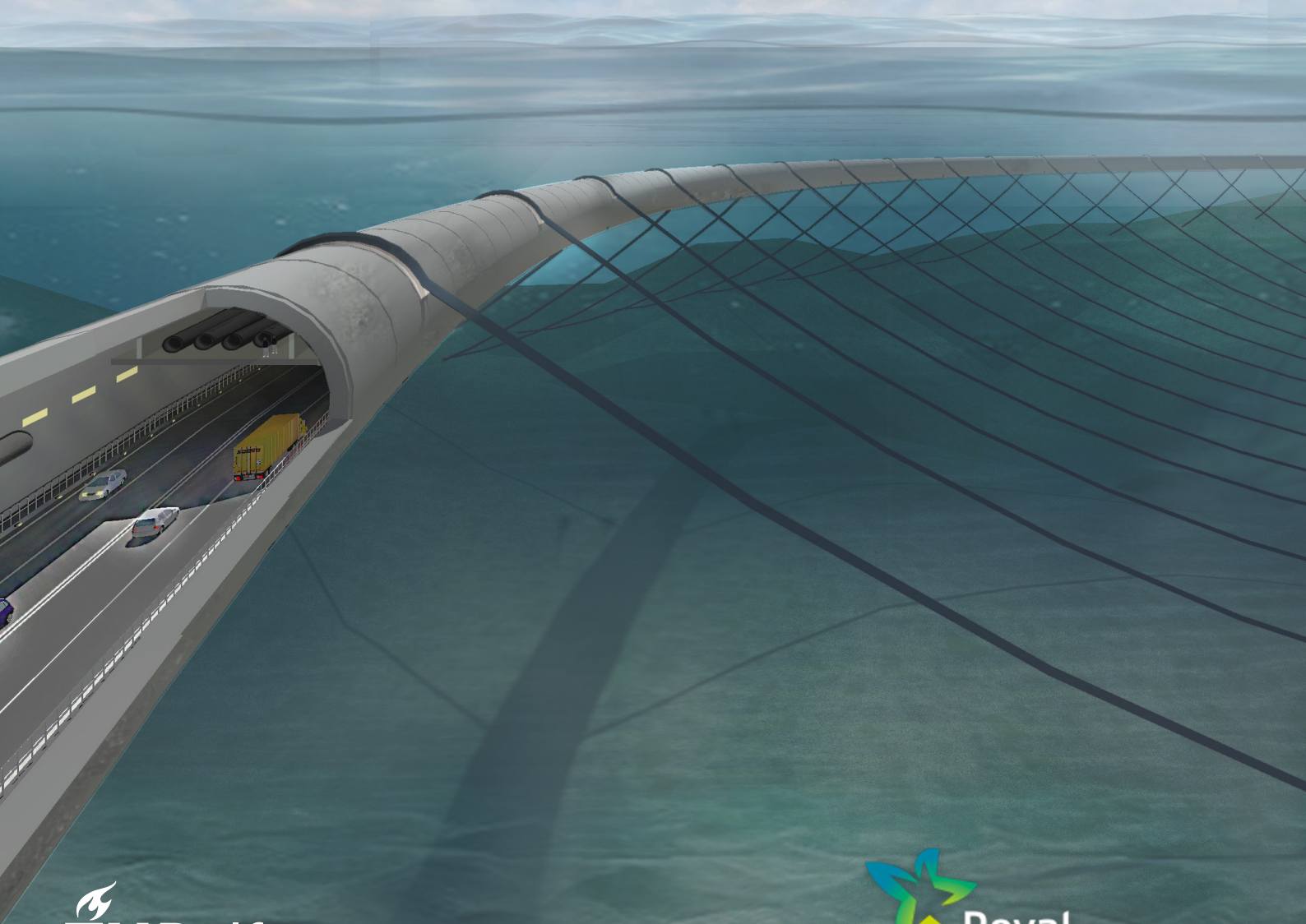
Submerged floating tunnel

The dynamic response due to fluid structure interaction

by

Mart-Jan Hemel

Date:	22 October 2019	
Project duration:	January 2019 – October 2019	
Supervisors:	Prof. dr. ir. Wim Uijttewaal,	TU Delft
	Dr. ir. Dirk Jan Peters,	TU Delft/Royal HaskoningDHV
	Dr. ir. Karel van Dalen,	TU Delft
	Dr. ir. Xuexue Chen,	Royal HaskoningDHV

TUDelft

Royal
HaskoningDHV
Enhancing Society Together

Preface

"At its heart engineering is about using science to find creative practical solutions. It's a noble profession."
Queen Elizabeth II

This thesis presents my research into the dynamic response of a submerged floating tunnel element due to fluid-structure interaction. Throughout history humans have developed various ways of crossing a waterbody. In a time that technology develops at such a high rate, innovative solutions have become more complicated than ever before. The idea of crossing an ocean through a submerged floating tunnel might still sound outlandish. However, it will not be long before all research will be turned into reality. Since many research has already been done prior, it can be concluded that this thesis is not the end of the story.

This thesis contributes to the final part of my master program of Hydraulic Engineering at Delft University of Technology. The research has been carried out in collaboration with Royal HaskoningDHV, for which I am very grateful. This tunnel adventure started with a conversation with Dirk Jan Peters, who invited me for this very interesting and challenging study. I started in January 2019 and now I can look back on a successful research of which I hereby proudly present the results.

Completing this research could never have been possible without the help of the members of my thesis committee and therefore I would like to express my sincere thanks to all of them. I would like to thank Wim Uijttewaal for chairing the committee. Your guidance and experience during the meetings provided me a lot of support. Furthermore I would like to thank Dirk Jan Peters for being the creative and understanding input. Our discussions did not only result in solutions, but also in great, new insights which brought the both of us further. Following, I would like to thank Karel van Dalen for helping me out with the complicated dynamic issues encountered along the way. Last but not least, I would like to express my thanks to Xuexue Chen, who acted as my daily supervisor. You were my closest helpline and nearest colleague at Royal HaskoningDHV.

To my family and friends I would like to say a big thank you for all the support. Special thanks go to my parents, brother and girlfriend who have helped my out during tough periods; not only for the unconditional aid during this thesis, but also during the past six years of studying. Now let us enjoy the engineering life!

Mart-Jan Hemel, October 2019

Executive summary

The submerged floating tunnel (SFT), also known as the Archimedes bridge or suspended tunnel, is a conceptual idea for a tunnel that floats in the water, supported by its buoyancy. The tunnel would be placed underwater, not too deep in order to avoid high water pressures, but deep enough for it not to be exposed to extreme weather conditions or obstruct shipping traffic. The tunnel is kept in position with tethers that are anchored to the sea bed or floating pontoons at the water surface. This thesis focuses on the tether supported SFT. The dynamic response of a tether supported SFT, in a hydrodynamic environment, is different from the tunnels that are widely used nowadays. The SFT is always in contact with open water in which it is moving due to the hydrodynamic environment. The dynamic response of the tether supported SFT is still a gap in our engineering knowledge and this contributes to the fact that world-wide no tether supported SFT has ever been constructed. Many research has been performed in the last years. A broad range of models has been used to study the dynamic behaviour of the tether supported SFT. The key in all these models is to capture the fluid structure interaction. Waves and current exert forces on the tunnel body but at the same time, the presence and motion of the tunnel body affects the wave-current environment.

To model the dynamic response of a tethered SFT incorporating fluid-structure interaction, a new model has been developed. The dynamic SFT model describes the cross sectional motion and tether forces of a rectangular tubular tunnel which is pinned down by two inclined tethers, excluding longitudinal effects. The tunnel is forced by waves and current only. When assuming the SFT system to be linear, the motion of the SFT can be seen as a superposition of the motion of the tunnel body in still water and the forces on the restrained tunnel body in waves and current. The tunnel motion in still water is modelled with a dynamic module while the hydrodynamic forces on a restrained tunnel body are computed with a wave force module. The two independent modules are combined in a coupling module which makes it possible to describe the dynamic response of a tether supported SFT in a wave-current environment. The advantages of this model choice are the fast computational time and the convenience of physical interpretation.

The wave force module computes the wave-current forces on the restrained tunnel body with a modified Morison formulation. This formulation is capable of computing, besides vertical and horizontal wave-current forces, the rotational wave force. Rotational wave forces are essential in the determination of tunnel roll motion and cannot be determined with the classical Morison theory. Just like the classical Morison theory, the modified Morison formulation does not take into account wave field deformation due to the presence of the tunnel structure. Therefore, for waves that are short compared with the dimensions of the SFT, diffraction effects cannot be taken into account. The absence of the diffraction effect is corrected for by integrating the dynamic pressures, water accelerations and water velocities with respect to the tunnel height and width. It should be noted that the applicability for short waves is only valid in case of structures that are submerged at a depth of at least 1.5-2 times the structure height. For shallowed submergence depths, the diffraction effects in combination with wave deformation become too large which cause prediction errors in the force determination. The force on the restrained SFT due to a uniform current can be modelled with the drag force expression from the classical Morison equation. To correct for the wave current interaction, the hydrodynamic mass coefficients are adapted as function of the Keulegan-Carpenter number.

The dynamic module describes the oscillation of the SFT, in still water, with a dynamic system. A free floating tunnel has three degrees of freedom which are roll, sway and heave. This dynamic system assumes the tunnel is connected with two in-extensible tethers. Adding two rigid constrains to the free floating tunnel reduces the SFT to a single degree of freedom system. This single degree of freedom system describes a coupled translational (sway) and rotational (roll) motion around an instantaneous rotational point which can be found at the intersections of the tether axes. When assuming small vibrations, the instantaneous rotational point remains fixed at the intersection of the tether axes when the tunnel is at rest. The moment of inertia of the SFT is obtained by using the Lagrangian approach which is based on energy conservation. Because the structure is submerged in water, added damping and mass terms are used in the equation of motion. The magnitude of these damping and mass terms is calibrated with physical model experiments.

The coupling module combines the wave force module and the dynamic module, which makes it possible to formulate a full equation of motion, describing the oscillation of the SFT in a wave current environment.

From the equation of motion the sway and roll motions, containing accelerations, velocities and displacements, can be obtained. Apart from the motions, the tether forces can be predicted. The dynamic SFT model is validated with physical model experiments.

With this dynamic SFT model, a parametric study has been performed. The first part of the parametric study focuses on the motion of the SFT. The second part examines the tether forces. Furthermore, the slack-taut transition and the safety against fatigue have been investigated. The parametric study does not take into account current. The most important findings and implications are in summary:

- Each SFT configuration has a different response to the wave environment. Hence, every configuration has a different critical wave length for which the dynamic response is maximum. This critical wave length is independent of the wave height. It should be noted that the dynamic response is a comprehensive term which consists of many variables. These are; tether forces, sway motions and roll motions of which both motions contain accelerations, velocities and displacements. The most dominant parameters to influence the dynamic response are the buoyance to weight ratio (BWR), tether angle and submergence depth.

- The BWR increases the stiffness of the dynamic SFT system which causes a decrease in the roll motions and sway displacement. Due to the stiffness increase, sway accelerations and velocities become larger. The natural frequency of the SFT is increased by increasing the BWR, which makes it more sensitive to shorter waves.

- Configurations with large tether angles have the character to be very flexible and sway dominant, while configurations with small tether angles are stiffer and roll dominant. Tether forces for configurations with large tether angles are more sensitive to long waves, while tether forces for configurations with small tether angles are more sensitive to short waves.

- A decrease in submergence depth increases all tunnel motions and tether forces, as the tunnel becomes more exposed to the wave environment. The dynamic response of the SFT becomes more sensitive to short waves.

- An increase in anchorage depth results in larger tunnel motions. The increase in tether forces is negligible.

- Placing the tether connection sideways of the tunnel body results in smaller roll motions and larger sway motions. Lowering the tether connection with respect to the tunnel bottom is favourable for all tunnel motions. The manner of how the tether connection is orientated, with respect to the tunnel body, has small influence on the tether forces.

- Increasing the BWR, submergence depth or both reduces the risk of snapping lines and tether fatigue. Configurations with small tether angles have a smaller risk of having line snapping and tether fatigue compared to configurations with large tether angles.

This study gives a supplement to the classical Morison theory. Morison's theory is modified which makes it possible to compute rotational moments due to wave loading. Also the applicability to short waves is enlarged. A new dynamic schematization is developed which makes it possible to describe the dynamic response of a SFT as a single degree of freedom (SDOF) system. The advantages of this dynamic schematization are the fast computational time and the convenience of physical interpretation. The results obtained from this research study can be used as a preliminary design tool. In an early design stage, motions and tether forces can be predicted. Also measures to reduce these motions and tether forces can be investigated using the dynamic SFT model. Design graphs to estimate the snap-taut transition and for safety against tether fatigue are provided. It should be noted that this dynamic SFT model should not be used for detailed computations in later design stages.

Contents

List of symbols

In this section a list of relevant symbols is provided. The list does not include symbols from the literature study and the appendices.

Latin symbols

Symbol	Description	Unit
A	Surface area	m^2
$a(t)$	Sway acceleration of SFT	m^2/s
$2a$	Width of SFT	m
b	Height of SFT	m
$C_{d,i}$	Morison drag coefficient in i direction	-
C_{dc}	Morison current drag coefficient	-
$C_{m,i}$	Morison hydrodynamic mass coefficient in i direction	-
c	Wave celerity	m/s
c_a	Added mass coefficient	-
c_r	Roll damping	Nms/rad^2
c_s	Sway damping	Ns^2/m
D	Dimension of submerged body	m
d	Water depth (literature study)	m
F_b	Buoyancy force	N
$F_{c,x}$	Horizontal damping force	N
$F_{cur,x}$	Horizontal forcing due to current	N
$F_{drag,i}$	Drag component of wave force in i direction	N
$F_{hydrod,i}$	Hydrodynamic component of wave force in i direction	N
$F_{Krylov,i}$	Krylov component of wave force in i direction	N
$F_{w,i}$	Total wave force in i direction	N
g	Gravitational acceleration	m/s^2
H	Wave height	m
h_1	Water depth	m
J	Inertia of SFT	m^2
KC	Keulegan-Carpenter number	-
k	Wave number	rad/m
L	Wave length	m
$M_{drag,y}$	Drag component of wave moment in i direction	Nm
$M_{hydrod,y}$	Hydrodynamic component of wave moment in i direction	Nm
$M_{Krylov,y}$	Krylov component of wave moment in i direction	Nm
$M_{c,y}$	Rotational damping moment	Nm
$M_{w,y}$	Rotational wave moment	Nm
M_w	Resultant wave moment at fictive rotational point	Nm
M_s	Resultant stabilizing moment at fictive rotational point	Nm
M_c	Resultant damping moment at fictive rotational point	Nm
m	Mass SFT	kg
m'	Hydrodynamic mass	kg
$\vec{n}$	Outward normal vector	-
R	Ratio between maximal and minimal tether force	-
$\vec{r}$	Position vector	N/m
p	Dynamic pressure	Pa
S	Surface	-
s_1	Submergence depth (Still water level to top of tunnel)	m

T	Wave period	s
T_{inner}	Inner tether force	N
T_{outer}	Outer tether force	N
t	Time	s
u_c	Current velocity	m/s
u_x	Water particle velocity in x direction	m/s
u_z	Water particle velocity in z direction	m/s
V	Volume of submerged body	m^3
$v(t)$	Sway velocity of SFT	m/s
x	Horizontal axis	m
$x(t)$	Sway SFT	m
z	Vertical distance from still water	m

Greek symbols

Symbol	Description	Unit
$\alpha(t)$	Roll acceleration of SFT	rad^2/s
α_T	Tether angle	°
γ	Connection width of SFT tether	m
ϵ	Connection height of SFT tether	m
ζ	Wave amplitude	m
θ_1	Angular rotation of tether	rad
θ_2	Angular rotation of SFT around virtual rotation point	rad
ω	Wave frequency	rad/s
$\omega(t)$	Roll velocity of SFT	rad/s
ρ	Density of the fluid	kg/m^3
ρ_t	Density of the SFT	kg/m^3
λ	Scaling parameter between θ_1 and θ_2	-
Φ	Velocity potential function	m^2/s
$\phi(t)$	Roll SFT	rad

Acronyms

DOF   degrees of freedom

SDOF single degree of freedom

MDOF multi degrees of freedom

SFT   submerged floating tunnel

BEM   boundary element method

BWR   buoyance to weight ratio

ODE   ordinary differential equation

RAO   response amplitude operator

EOM   equation of motion

CFD   Computational Fluid Dynamics

FSM   Finite Strip Method

RANS Reynolds-averaged Navier-Stokes

FEM   Finite Element Method

1

Introduction

1.1. Background

The submerged floating tunnel (SFT), also known as the Archimedes bridge or suspended tunnel, is a conceptual idea for a tunnel that floats in the water, supported by its buoyancy and support structure. The tunnel would be placed underwater, not too deep in order to avoid high water pressures, but deep enough for it not to be exposed to extreme weather conditions or obstruct shipping traffic. The tunnel is kept in position with a support mechanism. Globally four different SFT crossings can be defined; the free, column, pontoon and tether supported SFT. The four crossing types are schematized in figure 1.1. The free supported tunnel has no support mechanism along the tunnel tube. It is anchored at the abutments and the tunnel itself is free floating. The concept is only applicable for small crossing lengths because with longer spans, the forces in the cross section become too large. A column supported design uses columns to support the tunnel segment. Actually the tunnel is not floating but simply supported like a bridge. These underwater bridges are limited by the water depth. The pontoon tunnel type is supported by pontoons. The pontoons float on the water surface and via cables the tunnel is kept on its position. This variant is very sensitive to tide, wind, waves and currents. Another negative aspect of this variant is the risk of collision with vessels. However this design is not limited by water depths. Important to realise is the fact that the tunnel segment should have a downward directed resultant force. The buoyancy should not be greater than the weight of the tunnel. The last type of SFT is the tether type. In this variant, the tunnel tends to float upward. However, tethers are anchored in the seabed and pull the floating tunnel down. Opposite form the previous variant, this design needs to have a upward directed resultant force. The buoyancy should be greater than the weight of the tunnel.

A SFT anchored to the seabed with tethers seem to be a promising alternative for long-span bridges and tunnels. Fjords, lakes and sea-straights can be crossed with this floating type of structure. The latter mentioned tether supported SFT is the only crossing type to be considered in this thesis.

Free supported | Column supported

Pontoon supported | Tether supported
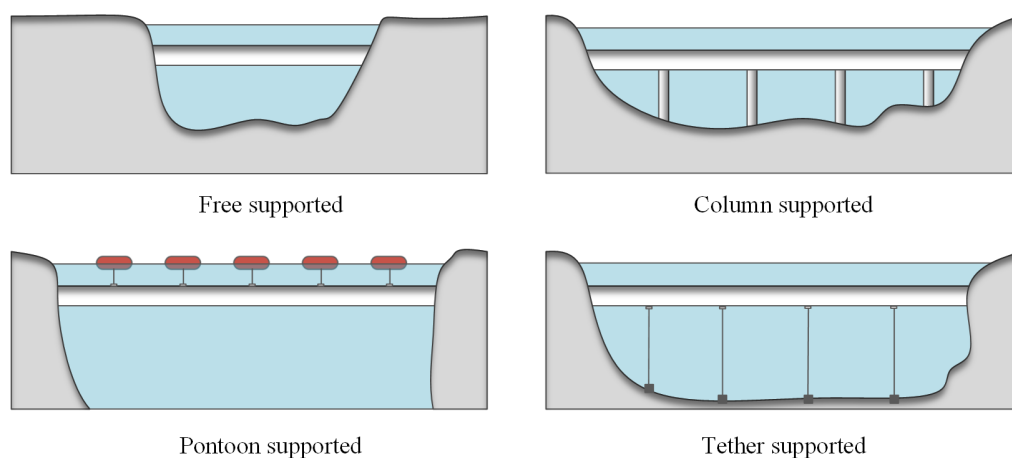
Figure 1.1: Schematization of different SFT types. *(Own figure)*

1.2. Problem statement

The dynamic response of a tether supported SFT, in a hydrodynamic environment, is different from the tunnels that are widely used nowadays. The SFT is always in contact with open water in which it is moving due to, for example, waves and current. The dynamic response of the tether supported SFT is still a gap in our engineering knowledge and this contributes to the fact that world-wide no tether supported SFT has ever been constructed. Many research has been performed in the last years. A broad range of models has been used to study the dynamic behaviour of the tether supported SFT. The key in all these models is to capture the fluid structure interaction. Waves and current exert forces on the tunnel body but at the same time, the presence and motion of the tunnel body affects the wave-current environment. Models to determine the dynamic response of the SFT vary from simple dynamic models to complicated Computational Fluid Dynamics (CFD) models. Various dynamic systems are combined with different forcing types. A too simple dynamic model is not capable of capturing the characteristic dynamic behaviour of the tether supported SFT while a too complicated dynamic model would result in high development costs, long computational time and the inconvenience of physical interpretation. Combining a simple dynamic system with a relative simple forcing method, which is capable of capturing the fundamentals of the dynamic response of the tether supported SFT, would result in a fast and well interpretive dynamic model. Such a model does not yet exist.

1.3. Research objective

In this master thesis, a dynamic model is created to develop a better understanding of the effect of hydrodynamics from waves and current on the dynamic response of a tether anchored SFT. The dynamic model can be validated with measured data which is obtained during physical experiments by (Drost, 2019). An extensive elaboration of these experiments can be found in appendix D.

1.3.1. Research questions

Based on this research objective, research questions and related sub-questions can be formulated.

1. **How can forces on a SFT in a wave-current environment be predicted?**

   (a) *What is an appropriate method to model the forces on a restrained SFT in a wave-current environment?*

   (b) *What is the effect of surface wave pressures due to short waves?*

   (c) *Is this method suitable for cases in which motion and position-change is relevant?*

2. **How can the dynamic response of a tethered supported SFT be modelled in a wave-current environment?**

   (a) *How can fluid structure interaction between a wave-current environment and a moving SFT be modelled?*

   (b) *What kind of dynamic system can be used to simulate the dynamic response of a SFT?*

3. **How can structural parameters be used to reduce the dynamic response of a tethered supported SFT in a wave-current environment.**

   (a) *Which structural parameters are dominating the dynamic response of the SFT structure?*

   (b) *How do structural parameters influence the dynamic response of a SFT in terms of tunnel motions and tether forces?*

   (c) *How does this study contributes to the research field of SFT?*

1.4. Scope

- This thesis only focuses on the tether supported SFT. The other three variants are not be elaborated. As explained in the previous section, this type of SFT consist of a cable configuration which is anchored at the sea bottom and a hollow tube which tends to float upwards.

- Because the tunnel is submerged, it will be affected by all kinds of loads (Faggiano et al., 2005). These are (1) permanent loads (self-weight, hydro-static pressures, buoyancy forces), (2) service loads (rail/road traffic, loads during construction), (3) hydrodynamic loads (waves, streams, tides) and (4) exceptional loads (earthquakes, fire, explosions, flood, collisions, encrustations due to underwater organisms). In this research only the permanent loads and hydrodynamic loads are taken into account.

- The dynamic response of the SFT is analysed only in the cross sectional plane.

- This thesis only focuses on rectangular SFT cross sections.

- This thesis only focuses on a SFT that in anchored with two inclined tethers.

- The dynamic model is validated with measured data which is obtained during physical small scale model experiments by (Drost, 2019).

1.5. Thesis outline

The outline of this research thesis consists of six chapters of which this introduction is the first. The second chapter is a literature study in which an overview of fundamental background theory is given. The literature study provides the necessary information which is required to develop a suitable dynamic SFT model. The literature study consist of several sections, starting with the basic theory of waves and current. Second, a brief overview of different hydrodynamic loading theories is given. These theories can be used to determine the hydraulic loading on submerged bodies. The dynamic response of vessels to hydraulic loading is closely related to the behaviour of a SFT. Vessel behaviour in waves can be found in the fourth section of the literature study. Relevant theory on structural dynamics is provided in the next section. The last two sections provide a META-analysis on the research of SFT dynamics and some reference projects.

The third chapter describes the dynamic SFT model that is used to analyse the dynamic response of the SFT. In the first five sections, the model and its modules are described. The modules are than explained separately in different sections. Extensive background information of these modules can be found in appendix A (wave force module), B (dynamic module) and C (coupling module).

The dynamic SFT model is validated in the fourth chapter. The validation is performed with data from physical model experiments which can be found in appendix D.

The fifth chapter contains a parametric study in which the dynamic response of the SFT is studied with the dynamic SFT model. The influence of several parameters on tunnel motions and tether forces is investigated. Furthermore, design graphs to estimate the snap-taut transition and safety against tether fatigue are provided.

In the last chapter of this thesis the conclusion, discussion and recommendation is given. The outline of this thesis can be found in figure 1.2.
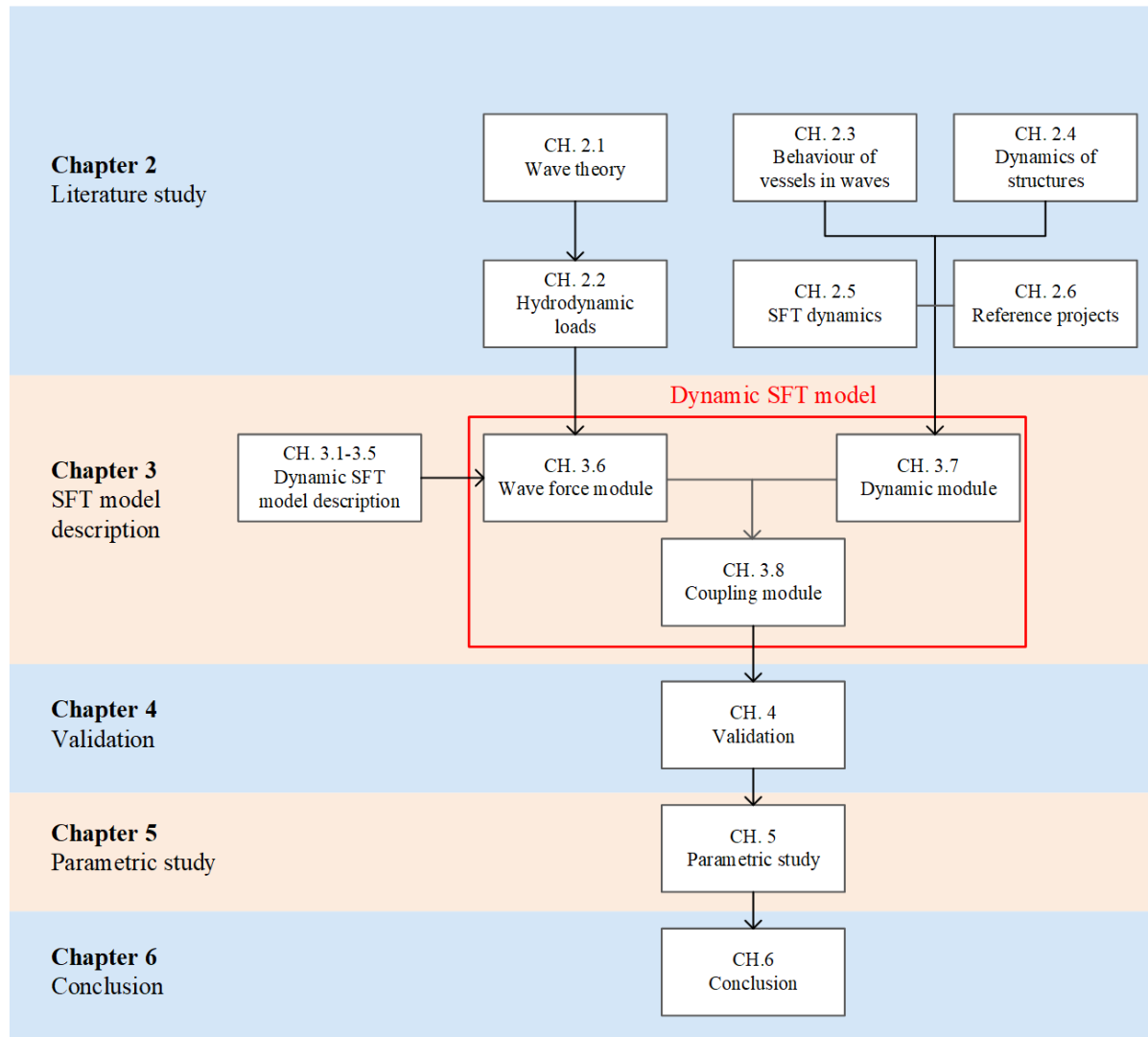
Figure 1.2: Thesis outline

2

Literature study

2.1. Wave theory

The governing external load on a submerged floating tunnel (SFT) is due to waves and current. To understand the dynamic behaviour of the tunnel, the wave and current need to be understood and analysed. The behaviour of waves and current is elaborated in this section.

2.1.1. Linear wave theory

To describe waves in water, the airy wave theory is often used (Airy, 1841). The airy wave theory, also called the linear wave theory, gives a linearized description of the propagation of gravity waves. The linear wave theory is a solution based on two equations: the mass balance equation and the momentum equation. The flow field in the domain can be depicted by a velocity potential satisfying the two dimensional Laplace equation shown in eq 2.1. In this equation, the vertical axis is described by z and the horizontal axis by x.

$$\frac{\partial^2 \Phi}{\partial x^2} + \frac{\partial^2 \Phi}{\partial z^2} = 0 \tag{2.1}$$

A solution to the Laplace equation can be found in the form of a propagating harmonic wave with constant and relatively small amplitude assuming that the fluid is inviscid, incompressible, and the motion irrational and periodic. The flow field domain is bounded by the water surface, no water particles can escape from the water surface, and the bottom, no water particles can penetrate the bottom. The external forcing is only due to gravity (Holthuijsen, 2007). The solution for eq 2.1 is found in the velocity potential function (eq 2.2) for which the spatial derivatives are equal to the velocities of the water particles.

$$\Phi = \frac{\omega \zeta}{k} \frac{\cosh[k(d+z)]}{\sinh(kd)} \cos(\omega t - kx) \tag{2.2}$$

$$u_x = \frac{\partial \Phi}{\partial x}, u_z = \frac{\partial \Phi}{\partial z} \tag{2.3}$$

In eq 2.2, k is the wave number which is determined by the dispersion relation presented in eq 2.4.

$$L = \frac{gT^2}{2\pi} \tanh(\frac{2\pi d}{L}) \quad or \quad \omega^2 = gk \tanh(kd) \tag{2.4}$$

Taking the derivatives of the velocity potential in x and z direction will give the horizontal and vertical water particle velocities presented in eq 2.5 and eq 2.6.

$$u_x = \omega \zeta \frac{\cosh[k(d+z)]}{\sinh(kd)} \sin(\omega t - kx) \tag{2.5}$$

$$u_z = \omega \zeta \frac{\sinh[k(d+z)]}{\sinh(kd)} \cos(\omega t - kx) \tag{2.6}$$

The propagation speed of the wave is the relation between the wave frequency and the wave number which represents the number of wave lengths per unit length. The wave propagation speed is shown in eq 2.7.

$$c = \frac{g}{\omega} \tanh(kd) \tag{2.7}$$

The particle motions which are described in eq 2.5 and eq 2.6 imply accelerations that can only be caused by a certain force acting on those particles. In the case of a fluid, these forces are exited by gradients in the pressure. The analytical solution for the wave induced pressure can be obtained by substituting the velocity potential into the two dimensional Bernoulli equation which can be found in eq 2.8.

$$\frac{\partial \Phi}{\partial t} + \frac{1}{2}\left[\left(\frac{\partial \Phi}{\partial x}\right)^2 + \left(\frac{\partial \Phi}{\partial z}\right)^2\right] + \frac{p}{\rho} + gz = 0 \tag{2.8}$$

or in vector notation,

$$\frac{\partial \phi}{\partial t} + \frac{1}{2}|\nabla \Phi|^2 + \frac{p}{\rho} + gz = 0 \tag{2.9}$$

$$\frac{\partial \Phi}{\partial t} = -\frac{\omega^2 \zeta}{k} \frac{\cosh[k(d+z)]}{\sinh(kd)} \sin(\omega t - kx) \tag{2.10}$$

Substituting eq 2.10, combined with the dispersion relation, into the linearized Bernoulli equation will give an analytical expression for the pressure in the water column. The linearized Bernoulli equation can be obtained by removing the quadratic terms. This expression is shown in eq 2.11.

$$p = \underbrace{-\rho gz}_{\text{Hydrostatic pressure}} + \underbrace{\rho g\zeta \frac{\cosh[k(d+z)]}{\cosh(kd)} \sin(\omega t - kx)}_{\text{Wave-induced pressure}} \tag{2.11}$$

The first part of this expression for the total pressure is the hydro static pressure which is linear over the water depth. The second part is due to the wave and therefore represents the wave-induced pressure. It should be noted that the dynamic pressure has similarity with the expression for the orbital velocity. The wave-induced pressure formula is valid in the small-amplitude approximation of the linear wave theory. Waves will always have finite amplitude for which the theory breaks down near the water surface. Above the still water line, the pressure is sometimes approximated as hydro static. An overview of the pressure is given in figure 2.1.
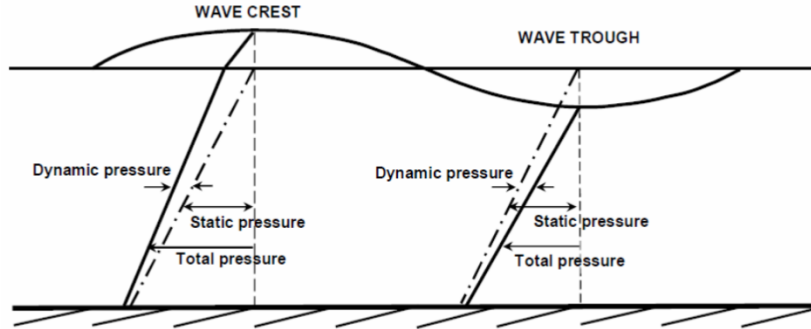
Figure 2.1: Wave-induced pressure combined with hydrostatic pressure (Reniers & Tissier, 2018).

The pressure field in the domain, acting as a force, will accelerate the water particles. The acceleration of the water particles can be determined by taking the time derivative of the water particle velocity. The water particle accelerations are presented in eq 2.12 and eq 2.13.

$$\frac{\partial u_x}{\partial t} = \omega^2 \zeta \frac{\cosh[k(d+z)]}{\sinh(kd)} \cos(\omega t - kx) \tag{2.12}$$

$$\frac{\partial u_z}{\partial t} = -\omega^2 \zeta \frac{\sinh[k(d+z)]}{\sinh(kd)} \sin(\omega t - kx) \tag{2.13}$$

2.1.2. Breaking waves

In figure 2.2, the ranges of applicability of various wave theories is presented. In here two important wave breaking criteria can be observed, the one in shallow water and in deep water. The shallow water wave breaking criteria is based on the depth ($\frac{H}{d} = 0.88$) while in deep water this is based on the steepness of the wave ($\frac{H}{L} = 0.142$).
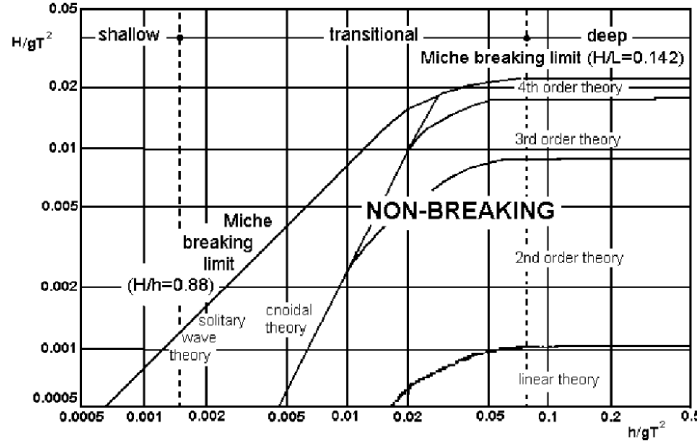
Figure 2.2: The ranges of applicability of the various wave theories (Méhauté, 1969).

2.1.3. Effect of depth current profile on wave parameters

In regions where a depth varying current is present, waves start to deform. The current wave interaction changes the wave properties which also affects the forcing on the SFT. In the case of a depth linear shear current, the dispersion relation and the relationship for wavelength and wave height can be obtained analytically. The application for this analytical solution is mainly for practical use (Kantardgi, 1995).

Gravity waves that are propagating on a stream of velocity $U(z)$ change the kinematic boundary conditions for solving the Laplcae equation. To describe the kinematic problem, a Rayleigh equation of a hydro-dynamic stability theory for the vertical velocity $w(z)$ is used (Peregrine, 1976).

$$\frac{\partial^2 w}{\partial z^2} - \left(k^2 + \frac{1}{U-c}\frac{\partial^2 U}{\partial z^2}\right)w = 0 \qquad -d \leq z \geq 0 \tag{2.14}$$

The boundary value problem for $w(z)$ is presented in eq 2.14 together with the boundary conditions presented in eq 2.15 and eq 2.16.

$$(U-c)^2\frac{\partial w}{\partial z} = \left[g + (U-c)\frac{\partial U}{\partial z}\right]w \qquad z = 0 \tag{2.15}$$

$$w = 0 \qquad z = -h \tag{2.16}$$

For a linear depth varying current, two different profiles can be distinguished. These are the depth linear shear current 2.3a and the linear surface shear jet 2.3a. The current for the depth linear shear profile is present at each water depth. For the surface shear jet profile, the current is only present at the surface of the domain. Both profiles have a different solution for determining the wave number and wave height.

The solution for the wave number and wave height influenced by a depth linear shear profile current has been written by (Kantardgi et al., 1989). The relation $\frac{k}{k_0}$, in which k_0 is the wave number without current and k is the wave number influenced by current, is given in eq 2.17.

$$\frac{U_s}{c_0}\frac{k}{k_0} - \frac{1}{2}\tanh(kd) + \frac{1}{2}\left[\left(\frac{\Lambda}{k_0 c_0}\right)^2\tanh^2(kd) + 4\frac{k}{k_0}\tanh(kd)\tanh^{-1}(k_0 d)\right]^{0.5} - 1 = 0 \tag{2.17}$$

The relation $\frac{H}{H_0}$, in which H_0 is the wave height without current and H is the wave height influenced by current, is given in eq 2.18.

(a) Depth linear shear current

(b) Linear surface shear jet
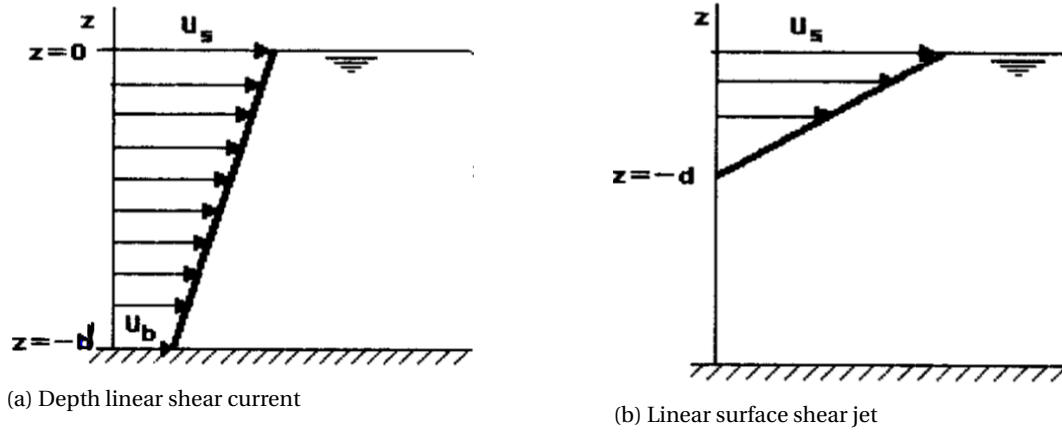
Figure 2.3: Definition sketches for current depth profiles. (Kantardgi, 1995)

$$\left(\frac{H}{H_0}\right) = \left(\frac{\omega_{rs}}{\omega_0}\right)\left(\frac{C_{g0}}{C_g}\right)\left(1 - \frac{1}{2}\frac{\Lambda}{g}c_{rs}\right)^{-1} \tag{2.18}$$

in which Λ is the constant vorticity of the current velocity profile.

$$\Lambda = \frac{U(z) - U_s}{z} \tag{2.19}$$

In eq 2.18 & 2.19, U_s is the current surface velocity, $\omega_{rs} = \omega - kU_s$ is the wave frequency that is related with the current surface velocity, $c_{rs} = \omega/k - U_s$ is the wave speed related with the current surface velocity, C_g is the wave group velocity and index "0" refers to the quantities in the domain without the presence of currents.

2.2. Hydro dynamic loads

The wave force acting on a structures in a fluid has been investigated for many years. In these years, many theories have been developed to compute the wave forces on these structures. Some of these methods do not only compute the wave forces on the structure but are also able to compute the hydrodynamic coefficients including added mass and damping coefficients. The different methods can be subdivided into global traditional methods (Pan et al., 2012). These methods will be elaborated in separate sections.

- Velocity potential

- Morison's equation

- Computational Fluid Dynamics (CFD)

- Physical model experiments

2.2.1. Velocity potential

To compute the wave forces on a fixed submerged body, the velocity potential theory can be used. In case of an infinitely long structure, the velocity component parallel to the axis of the cylinder disappears and the motion becomes two dimensional. The fluid can be described by a velocity potential satisfying the two dimensional Laplace equation. To determine the wave force on the submerged body, two velocity potential functions need to be defined. An incident velocity potential and diffracted (stream) potential (Ursell, 1948).

$$\Phi = \Phi_I + \Phi_D \tag{2.20}$$

The incident velocity potential is the undisturbed potential function. The diffracted potential takes into account the effect of the structure on the fluid. The velocity potential for the incident wave and for the diffracted wave need to satisfy the boundary conditions in the domain. For the incident velocity potential, these are known from the linear wave theory. For the diffracted velocity potential, the boundary conditions are determined by the shape of the submerged body. The potential problem can be solved in many ways. The

most common ways are: boundary element method (BEM) and Finite Strip Method (FSM) (Kunisu, 2010), Green's function (Weoncheol & K.Jun-Dong, 2015) and eigenfunction expansion matching method, for different domains, using the conditions of continuity (Zheng et al., 2006). In figure 2.4, the dimensionless wave forces, including the incident and diffracted potential fields, on a restrained rectangular submerged cylinder subjected to a linear wave train are presented..
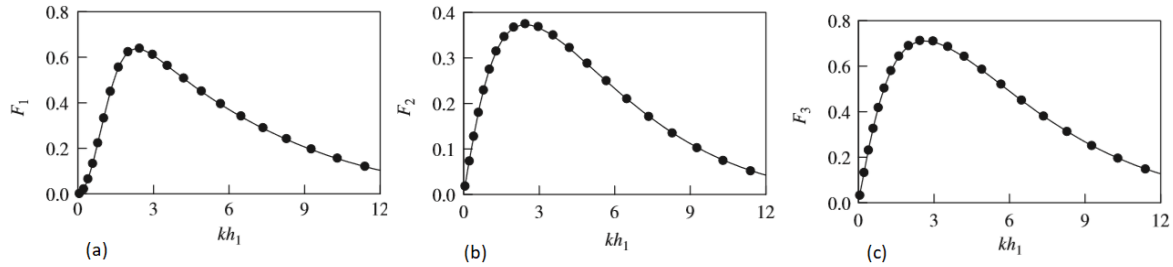
Figure 2.4: Dimensionless wave force on rectangular submerged cylinder by eigenfunction expansion matching method - and by BEM • (Zheng et al., 2006). F_1 = vertical force , F_2 = horizontal force and F_3 =rotational moment.

In case the submerged body is not fixed but free floating, the velocity potential should be expanded. In case of a two dimensional motion domain, three motions become possible. These are horizontal, vertical and rotational motions. For each motion, a radiated potential is added to the total potential as shown in eq 2.21. In this formulation, L = 1 stands for the vertical motion, L = 2 stands for the horizontal motion and L = 3 for the rotational motion.

$$\Phi = \Phi_I + \Phi_D + \sum_{L=1}^{3} \Theta_R^{(L)} \tag{2.21}$$

Each of these potentials need to fulfill requirements and boundary conditions in the fluid which will be elaborated in detail.

Laplace Equation

$$\frac{\partial^2 \Phi}{\partial x^2} + \frac{\partial^2 \Phi}{\partial z^2} = 0 \tag{2.22}$$

Sea Bed Boundary Condition
The velocity normal to the seabed can not penetrate the bottom.

$$\frac{\partial \Phi}{\partial z} = 0 \qquad for : z = -d \tag{2.23}$$

Free Surface Boundary Condition
Combining the free surface dynamic boundary condition with the free surface kinematic boundary condition results in Cauchy Poisson condition for finite water depths.

$$\frac{\partial^2 \Phi}{\partial t^2} + g\frac{\partial \Phi}{\partial z} = 0 \qquad for : z = 0 \tag{2.24}$$

Oscillating Body Surface Kinematic Boundary Condition
The velocity normal to the surfaces of the submerged body are equal to the velocity of the body itself.

$$\frac{\partial \Phi}{\partial n} = v_n(x, z; t) = \sum_{L=1}^{3} v_L f_L(x, z; t) \tag{2.25}$$

Radiation Condition
At a large distance D_b from the submerged body, the radiated potential due to the body motion tends to go to zero.

$$\lim_{D_b \to \infty} \Phi = 0 \tag{2.26}$$
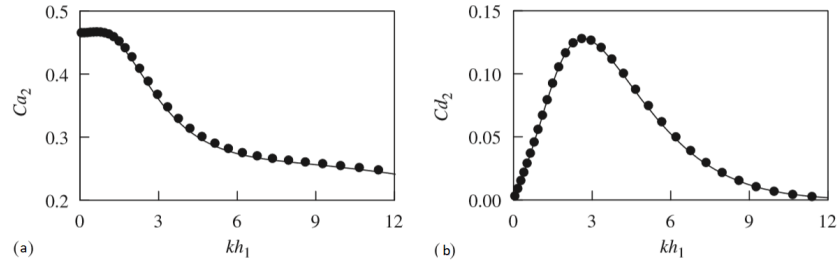
Figure 2.5: Dimensionless hydrodynamic coefficients on rectangular submerged cylinder by eigenfunction expansion matching method - and by BEM • (Zheng et al., 2006). C_{a2} = horizontal added mass , C_{d2} = horizontal damping

Again the boundary-value problem can be solved by applying different solution methods. Because the submerged body is moving in the fluid, hydrodynamic coefficients including the added mass and the damping can be determined. In figure 2.5, the added mass and damping for the horizontal motion are presented.

Integrating the pressures on each surface S of the submerged body gives the forces and moments on the body.

$$\vec{F} = -\iint_S (p\,\vec{n})\,dS \tag{2.27}$$

$$\vec{M} = -\iint_S p(\vec{r} \times \vec{n})\,dS \tag{2.28}$$

In which $\vec{n}$ is the outward normal vector on surface dS and $\vec{r}$ is the position vector of surface dS in the x,z coordinate system. The pressure p can be found by inserting the velocity potential into the linearized Bernoulli equation (eq 2.29).

$$
\begin{aligned}
p &= -\rho \frac{\partial \Phi}{\partial t} - \rho g z \\
&= -\rho \left(\frac{\partial \Phi_I}{\partial t} + \frac{\partial \Phi_D}{\partial t} + \frac{\partial \Phi_R}{\partial t} \right) - \rho g z
\end{aligned}
\tag{2.29}
$$

It should be noted that the potential flow theory does not include all the characteristics of flow. The potential flow theory can not be applied for viscous internal flows (Batchelor, 1973). Flows that include a boundary layer cannot be accounted for by the potential flow theory.

Summary

Advantages of velocity potential:

- The solution can be found analytically which gives fast computational time.

- Analytical solutions give great insight in the fundamental background of the problem

- The wave forces and hydrodynamic coefficients can be determined via one system of equations

- Wave forces and hydrodynamic coefficients can be computed for all ranges of wave lengths.

- The effect of the structure on the wave field can be computed. Transmission coefficients and reflection coefficients can be determined.

Disadvantages of velocity potential:

- To solve the boundary-value problem analytically, extensive mathematics is needed.

- Potential flow theory cannot be applied for viscous internal flows.

- Potential flow theory only applicable for certain geometries.

2.2.2. Morison's equation

Morrison's equation is based on both inertia and drag terms with empirical coefficients. These coefficients are based on Reynold's number and Kuelegan-Carpenter number (OBrien et al., 1950). It should be taken into account that the Morison equation has limitations. One of these limitation is that the the flow acceleration need to be more or less uniform at the location of the tunnel body. This requires that the tunnel dimensions should be much smaller than the wavelength of the incident wave. The tunnel dimension can be assumed slender to the wave length if $kD \approx 0$, in which D is the dimension of the tunnel (Bai, 1975). In case the structure dimensions are not slender compared to the wave length, diffraction effects have to be taken into account (Patel & Witz, 2013).

The Morison's equation is originally used to estimate the force acting on a vertically submerged cylinder. The equation is based on only the horizontal velocity and acceleration at the location of the object. The Morison's equation is shown in eq 2.30.

$$F_M = \underbrace{\frac{1}{2}\rho D C_d u|u|}_{\text{Drag force}} + \underbrace{\rho A C_m \frac{du}{dt}}_{\text{Inertia force}} \tag{2.30}$$

in which

F_M	=	Morison force
ρ	=	density fluid
u	=	velocity of fluid
D	=	object dimension
A	=	area

The equation includes two coefficients, C_d and C_m corresponding to the drag and the inertia force. The magnitude of these coefficients is based on the shape of the submerged object. The drag force is proportional to the velocity squared of the water particles along the submerged structure. The drag coefficient for rectangular prisms has been investigated in many studies. In figure 2.6, the drag coefficients for rectangular prisms, according to four different studies, are presented.
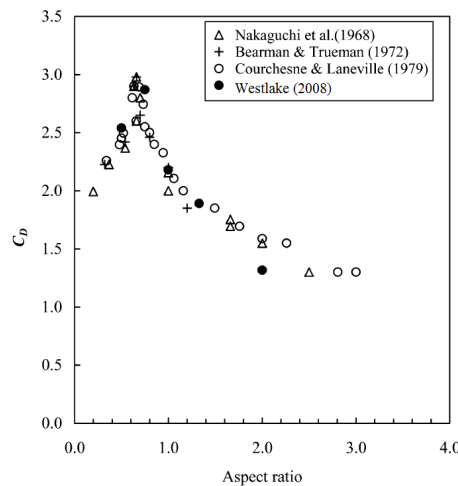
Figure 2.6: Steady flow drag coefficients for rectangular prisms (Venugopal et al., 2008) in which the aspect ratio (D/B) is defined by the ratio between the normal flow width D and the parallel flow width B of the submerged structure.

The inertia force consist of two terms, the Krylov force eq 2.31 and the hydrodynamic mass force eq 2.32. The Krylov force is caused by a horizontal pressure gradient in an undisturbed flow. The hydrodynamic mass force describes the force on the submerged object due to accelerating water around the object.

$$F_{Krylov} = \rho A \frac{du}{dt} \tag{2.31}$$

$$F_{Hydrodynamic} = m' \frac{du}{dt} = \rho A C_a \frac{du}{dt} \qquad (2.32)$$

in which

C_a = added mass coefficient
m' = hydrodynamic mass

The inertia coefficient C_m from eq 2.30 can be written as $C_m = (1 + C_a)$. The full formulation for the in-line force than reads:

$$F_M = \underbrace{\frac{1}{2}\rho D C_d u|u|}_{\text{Drag force}} + \underbrace{\rho A \frac{du}{dt}}_{\text{Krylov force}} + \underbrace{\rho A C_a \frac{du}{dt}}_{\text{Hydrodynamic force}} \qquad (2.33)$$

The hydrodynamic force is due to inertia and therefore also named inertia force. An accelerating fluid around an object will create inertia forces. To better understand the idea of added mass due to an accelerating flow, the interaction between body and fluid is reversed. Lets assume that the body is accelerating in still water. A submerged object that is accelerated in a stationary fluid will induce acceleration in its immediate neighborhood. The fluid that is accelerated around the submerged object will act as added mass (Dong, 1978). An impression is given in figure 2.7. Relations are found by (Dong, 1978) to estimate the magnitude of the added mass. These formulations are frequency independent which is in reality not the case (Vugts, 1971). The hydraulic added mass can be computed by means of the strip theory, in which for each motion, heave roll and pitch, the frequency depended added mass is determined. For estimation of the inertia wave force on the structure, a frequency independent added mass coefficient is used.
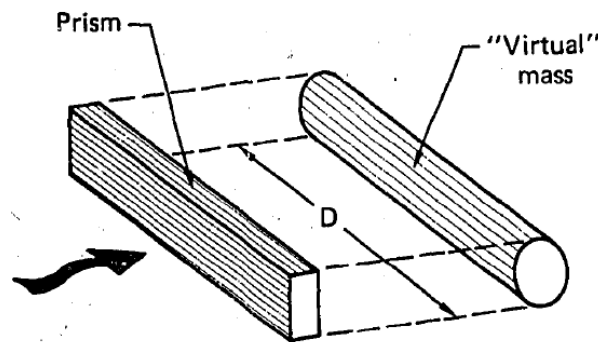
Figure 2.7: Submerged body and its virtual mass (Dong, 1978).

The hydrodynamic mass, described in figure 2.7, is proportional to the body volume and fluid density and is given by $m' = \rho V C_a$. The magnitude of the hydrodynamic mass coefficient C_m is dependent on the shape of the accelerated body and can be found in table 2.1.

Table 2.1: Hydrodynamic-mass coefficient C_m for two-dimensional infinitely long rectangular body (Sumer & Fredsoe, 1997).

Section through body	direction of motion	$\frac{a}{b}$	C_m	A
		∞	1.00	
		10.0	1.14	
		5.0	1.21	
	$\uparrow$	2.0	1.36	
	vertical	1.0	1.51	πa^2
	$\downarrow$	0.5	1.70	
		0.2	1.98	
		0.1	2.23	

If the submerged object is placed horizontally, the vertical velocity component will become relevant as well. According to (Sumer & Fredsoe, 1997), the Morison equation can be modified for a horizontal placed submerged object and is shown in eq 2.34 and eq 2.35.

$$F_x = \frac{1}{2}\rho C_{dx} D u_x \sqrt{u_x^2 + u_z^2} + \rho C_{Mx} A \frac{du_x}{dt} \tag{2.34}$$

$$F_z = \frac{1}{2}\rho C_{dz} D u_z \sqrt{u_x^2 + u_z^2} + \rho C_{Mz} A \frac{du_z}{dt} \tag{2.35}$$

In case of a flexible mounted vertical body, the body will move relative to the flow in the in-line direction. In this case, the Morison equation needs some adaptation. The adapted Morison equation is shown in eq 2.36.

$$F_M = \frac{1}{2}\rho D C_d (u - u_b)|u - u_b| + \rho A \frac{du}{dt} + \rho A C_a \left(\frac{du}{dt} - \frac{du_b}{dt} \right) \tag{2.36}$$

In here u_b is the velocity of the body in the in-line direction. It can be observed that the inertia force is divided into two parts. The Krylov force is based on $\frac{du}{dt}$ because this force is associated with the absolute motion of the fluid and not to the motion of the fluid body (Sumer & Fredsoe, 1997). The hydrodynamic force is depending on the absolute flow and the motion of the body. In this way both terms are not depending on the same acceleration and therefore the inertia force needs to be divided in the Krylow force and hydrodynamic force.

From eq 2.5 and eq 2.6 it can be observed that the velocity and acceleration are 90° out of phase. Because drag and inertia are related to the velocity and acceleration, the drag and inertia will always have a phase difference of 90°. To study the ratio between the drag force and the inertia force, the Keulegan-Carpenter number is often used. The KC number is defined in eq 2.37. In here u_m is the maximum in-line flow velocity and T the period of the oscillatory flow.

$$KC = \frac{u_m T}{D} \tag{2.37}$$

The numerator of eq 2.37 shows the length scale of the orbital wave motion and the denominator the length scale D of the submerged object. For a cylinder this can be the diameter, for a rectangle structure this can be the width. For small KC numbers it can be said that the orbital motion of the water particles around the submerged object is small with respect to the dimension of the object itself. This means that for small KC numbers no separation of flow behind the object will occur. In this case the drag will become negligible and inertia will dominate the system. However when the orbital motion of water particles will become large with respect to the object dimensions drag will become important. Flow separation and probably vortex shedding will be present. For large KC numbers, the flow will become a steady current for each half period of the orbital motion. The system will be drag dominant.

Summary
Advantages of Morison's equation:

- Very power full tool to estimate wave loads in the design of offshore structures.

- No extensive mathematical computations need to be performed and fast computational times are reached.

Disadvantages of Morison's equation:

- Morison can only be used in the situation that the submerged body is slender with respect to the wave length $kD \approx 0$.

- No moment due to short waves can be obtained by Morison's equation.

- The effect of the structure on the wave field is not taken into account, Morison's equation does not take into account diffraction effects or radiated waves in case of a moving object.

- Morison's equation is semi-empirical.

- The applicability of Morison is limited to simple object shapes.

2.2.3. Computational Fluid Dynamics (CFD)

Another method for determining the wave forces on a submerged object is CFD modeling. In this method, computers are used to compute the free-stream flow of the fluid and the interaction with the surfaces in this fluid. The surfaces are defined by boundary conditions. The basis of many CFD models is the Navier-Stokes equation. The in compressible Reynolds-averaged Navier-Stokes (RANS) equations are given by:

$$\frac{\partial u_i}{\partial x_i} = 0 \tag{2.38}$$

$$\frac{\partial u_i}{\partial t} + u_j \frac{\partial u_i}{\partial x_j} = f_i - \frac{1}{\rho}\frac{\partial p}{\partial x_i} + \nu \frac{\partial^2 u_i}{\partial x_i \partial x_j} \tag{2.39}$$

In which eq 2.38 is the continuity equation and eq 2.39 the momentum equation. The RANS equations are non-linear partial differential equations which makes it hard to solve. Numerical solving is often used. With CFD modeling, the fluid structure interaction can be computed on a detailed level. By applying moving boundary conditions, the motion of structures in fluids can be modelled. An research example simulation is presented in figure 2.8 in which a vessel is sailing perpendicular to the incident waves. The vessel is moved by the waves, and the wave field is deformed by the sailing vessel.
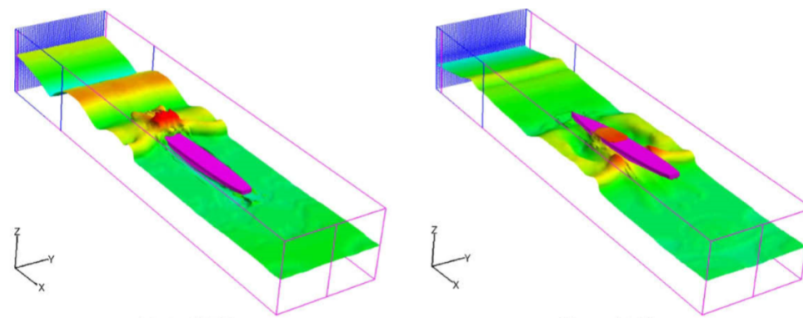
Figure 2.8: CFD simulation of wave-current-vessel interaction at two different moments in time (Chen & Yu, 2008).

Summary

Advantages of CFD:

- High accuracy.

- Object motions can be simulated.

- Simulations for all ranges of wave lengths can be performed.

- Applicable for complicated non-standard object shapes.

Disadvantages of CFD:

- High computational time.

- Complex modelling (long developing time).

2.2.4. Physical model experiments

The forcing on a submerged object due to wave forcing can also be determined by means of physical models (small scale) models. In this literature study, two small scale physical flume experiments are elaborated. The first one for a circular tunnel cross section which is compared with results from the BEM. The second experiment which is elaborated is for a rectangular tunnel cross section. For the last one, no other methods are used to compare the measurements with.

Circular cross section

(Kunisu, 2010) has done a study on the diffraction theory by BEM and the effect of the size and the shape of the SFT. Later on the drag and inertial forces where studied based on Morison's equation. The results of this study where compared with experimental data. The experimental set-up for the circular cross section is presented in figure 2.9. The results of the experiment are presented in figure 2.10. In these figures, the horizontal and vertical wave forces are measured for different wave numbers. The experiments are plotted together with the potential velocity theory which was computed by means of BEM. The experimental data matches the computed data quite well. Note that the shape of the BEM method has a similar shape as the results from the velocity potential method for the squared submerged cylinder elaborated in section 2.2.1.
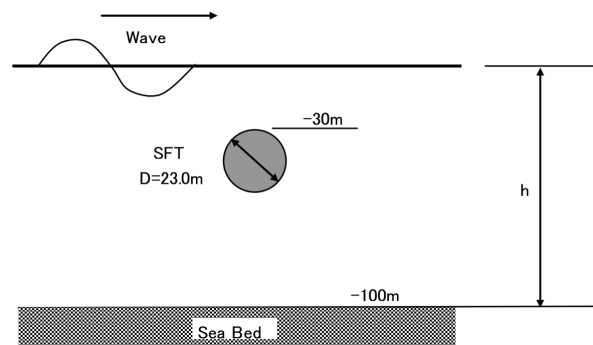
Figure 2.9: 2D side view flume experiment set-up circular tunnel cross section (Kunisu, 2010).
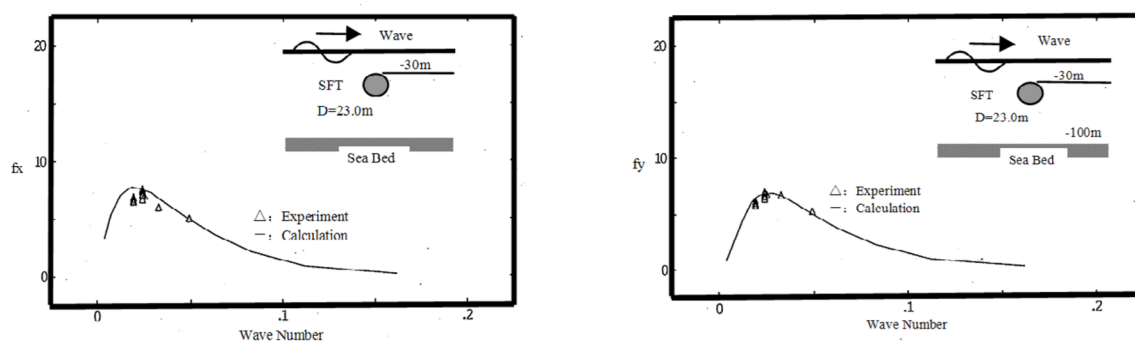
Figure 2.10: Experimental results vs BEM. Left figure: horizontal force, right figure vertical force (Kunisu, 2010).

Rectangular cross section

Experiments on a rectangular prism has been executed by (Drost, 2019). In these experiments, a fixed rectangular cross section is exposed to waves, current or a combined wave current environment. For the wave experiments a passive absorber dissipates the energy from the waves in such a way that no waves will reflect to the submerged body domain. A visualization of this experimental set-up is presented in figure 2.11.

The current is caused by a inflow in combination with a weir. During the experiments, the horizontal, vertical and rotational force on the object are measured. The experiment is executed on two submerged depths, $s_1 = 0.35m$ and $s_1 = 0.175m$. An extensive elaboration of this research can be found in appendix D. In this appendix, the forces on the fixed model due to current and a combination of waves and current are presented as well.
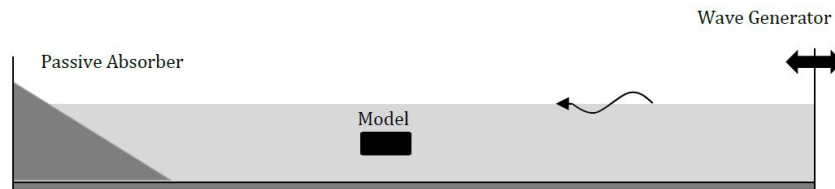
Figure 2.11: 2D side view wave flume experimet set-up rectangular tunnel cross section (Drost, 2019).

Summary

Advantages of model experiments:

- Good representation of reality.

- Validation material for mathematical model.

Disadvantages of model experiments:

- Physical scaling problems.

- Time consuming and costly.

- Not economical at the preliminary design stage.

- Requires special facilities and equipment.

2.2.5. Hydro static loads

An submerged body in a fluid will be subjected to an upward buoyant force which is equal to the weight of the fluid that is displaced by the body. This force is can be determined with the Archimedes principle which can be found in eq 2.40.

$$F_b = \rho g V \tag{2.40}$$

in which

F_b	=	Buoyancy force
ρ	=	Density fluid
g	=	Gravitational acceleration
V	=	Displaced volume

The resultant static force on the submerged body can be obtained by subtracting the self weight of the tunnel cross section from the buoyancy force which is directed perpendicular to the self weight. For the SFT, the buoyancy force must always be bigger than the self weight of the tunnel otherwise the tunnel will not float up.

2.3. Behaviour of vessels in waves

The motion of a vessel can be split into three mutually perpendicular translations of the centre of gravity and three rotations around the centre of gravity. These motions are illustrated in figure 2.12. The behaviour of a vessel in waves is thus a six-degree-of-freedom system that can be described by equations of motion (Faltinsen, 1990). The physics involved with vessel motions in waves in shallow water are complex in character. That make them difficult to predict accurately, especially for moored vessels.
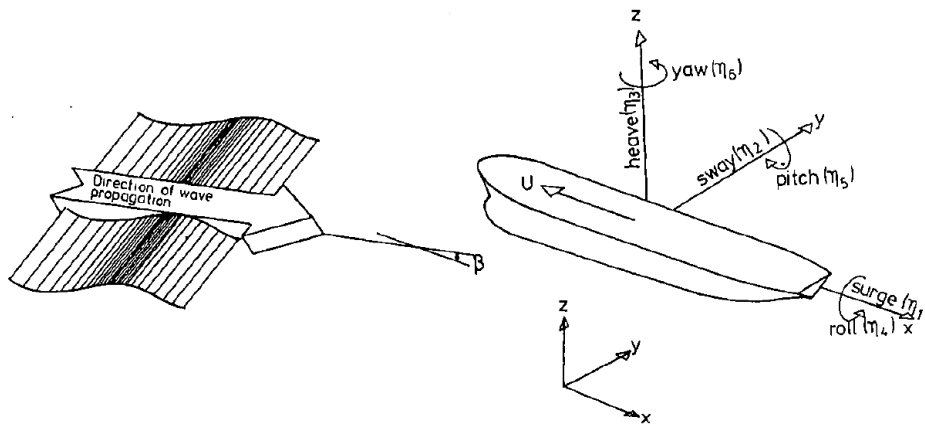
Figure 2.12: Definitions of coordinate system, rigid-body motion modes and wave propagation direction. U is the forward speed of the vessel (Faltinsen, 1990).

2.3.1. Single linear mass-spring system

Since the system can be assumed linear, the motion of a vessel van be seen as a superposition of the motion of the body in still water and the forces on the restrained body in waves (Journée & Massie, 2001). This is illustrated in figure 2.13. Let us consider a single linear mass-spring system that represents the heave motion of a floating object in linear waves.
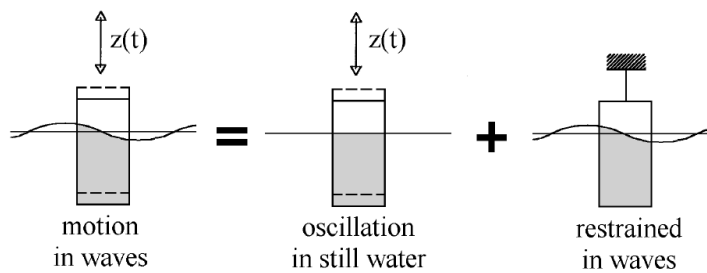
Figure 2.13: Superposition of hydro-mechanical and wave loads (Journée & Massie, 2001).

The first part of the superposition is described by a free decay test in still water in which the floating body will be released and the motion can die out freely. The object has a mass m and the vertical displacement is expressed as z. The sum of all forces on the object is given as $m\ddot{z}$. From eq 2.41 it can be seen that the motion of the object will result in forces on the object, a damping term and a spring term. The damping term b will give the decay for the amplitude of the vertical motion.

$$(m + a)\ddot{z} + b\dot{z} + cz = 0 \tag{2.41}$$

in which

a = hydrodynamic mass coefficient
b = hydrodynamic damping coefficient
c = restoring spring coefficient, based on the Archimedes force.

The second part of the superposition is described by forces on the restrained body due to waves. The wave load is described by a deep water wave. Let us assume that the body is slender compared to the wave length ($kd \approx 0$). In this case the force at the bottom of the body becomes: $F = (\rho g \zeta_a e^{-kW} \cos(\omega t) + \rho g W) A_b$. In here W is the draft of the object, ζ_a the wave elevation and A_b the surface area of the bottom of the object. The harmonic part of this force is called the Froude-Krilove force which is obtained from integration of the pressures on the body in the undisturbed wave (Journée & Massie, 2001). This force can be expressed as
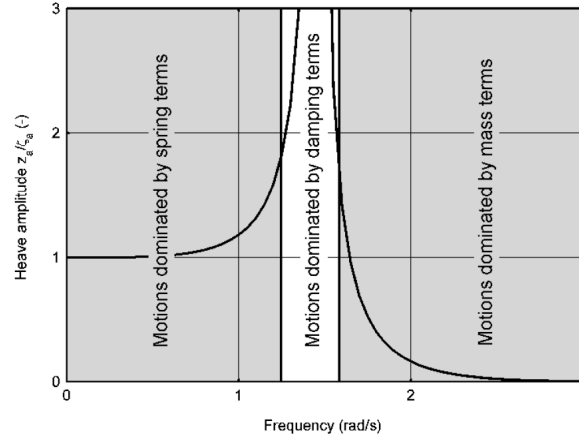
Figure 2.14: Example of the influence of frequency on the RAO for heave. There are three frequency areas with a different terms dominating the equations of motion. Please note that the vertical axis shows the heave RAO (Z_c/ζ_c), not the heave amplitude (Z_c) (Journée & Massie, 2001).

a spring coefficient c (which is the same found in eq 2.41) times a reduced wave elevation ζ^*. Because of diffracted waves, a correction of the Froude-Krilov force is needed. Additional force components can be found in the form of vertical acceleration and vertical velocity. The total wave force is shown in eq 2.42.

$$F_w = a\ddot{\zeta}^* + b\dot{\zeta}^* + c\zeta^* \tag{2.42}$$

The reduced wave elevation is given by $\zeta^* = e^{-kW}\cos(\omega t)$. Combining the equation of motion (EOM) from eq 2.41 and the forcing from eq 2.42, the heave equation of motion can be obtained shown in eq 2.43.

$$(m+a)\ddot{z} + b\dot{z} + cz = a\ddot{\zeta}^* + b\dot{\zeta}^* + c\zeta^* \tag{2.43}$$

Solving this second order differential equation will lead to the following relation between heave amplitude and wave elevation shown in eq 2.44.

$$\frac{z}{\zeta_a} = e^{-kW}\sqrt{\frac{\{c - a\omega^2\}^2 + \{b\omega\}^2}{\{c - (m+a)\omega^2\}^2 + \{b\omega\}^2}} \tag{2.44}$$

It can be seen that the ratio between vertical object displacement (heave) and the wave amplitude is determined by the wave frequency. This ratio is referred to as response amplitude operator (RAO). The response of a vessel to wave forcing can be assumed linear (Journée & Pinkster, 2002): the ratio between response amplitude and wave amplitude is constant. Each degree of freedom has its own RAO. A graphical visualization of the RAO from eq 2.44 is shown in figure 2.14.

Figure 2.14 shows that with respect to the motional behaviour three frequency areas can be distinguished (Journée & Massie, 2001):

- The low frequency area where the ship follows the wave motions. $\omega^2 << c/(m+a)$. These waves generally have a wavelength that is much larger than the length of the ship. The RAO have a value of 1: the amplitude of ship motions is equal to the wave amplitude.

- The natural frequency area with motions in resonance: ship motion amplitudes in this frequency range are larger than the corresponding wave amplitude. $\omega^2 \approx c/(m+a)$. The RAO have a value larger than 1.

- The high frequency area with very small vessel motions. $\omega^2 >> c/(m+a)$. The high frequency waves generally have a wavelength that is smaller than the length of the vessel, so wave forces are averaged out. The RAO have a value of 0.

RAO can be obtained using model tests or by model simulation. When a RAO has been obtained, the motions of the vessel can be calculated using the following equation:

$$S_z(\omega) = \left|\frac{Z_a}{\zeta_a}(\omega)\right|^2 \cdot S_\zeta(\omega) \tag{2.45}$$

in which:

$S_z(\omega)$	=	the motion spectrum of the vessel	$[\text{m}^2/\text{Hz}]$
Z_a/ζ_a	=	the RAO	$[\text{m}/\text{m}]$
$S_\zeta(\omega)$	=	the wave spectrum	$[\text{m}^2/\text{Hz}]$

The significant motion is then: $Z_s = 4\sqrt{m_0}$, where m_0 is the spectral moment of the vessel motion spectrum. This calculation can be done for all ship motions.

2.3.2. Nonlinear damping

There are some cases (especially for roll motions) that viscous effects influence the damping on the structure in motion. This could result in strongly non-linear damping coefficients (Journée & Massie, 2001). In case of roll, the roll damping gives a rotational moment which can be described by eq 2.46 in which b^i are the damping coefficients.

$$M_r = b^{(1)}\dot{\phi} + b^{(2)}|\dot{\phi}|\dot{\phi} + b^{(3)}\dot{\phi}^3 \tag{2.46}$$

2.4. Dynamics of structures - relevant theory

In order to gain insight in the dynamic response of a system due to dynamic loads, schematization is needed. To understand the dynamic response of a SFT in a wave current environment, first the response of a single degree of freedom (SDOF) system is elaborated. Later on the Lagrangian method is explained followed by the schematization of a tether as a spring.

2.4.1. SDOF

Two SDOF systems will be elaborated, the mass spring system and the pendulum system. The first system describes a transverse motion while the pendulum system describes a rotational motion. Figure 2.15a shows a mass spring system with mass m, spring k and damping c loaded by a random time dependent load $M(t)$. The system describes the horizontal motion $x(t)$ in time.
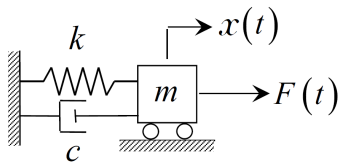
(a) Mass spring system (van Dalen, 2018).
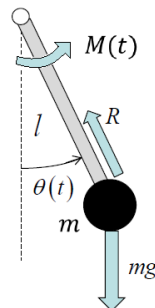
(b) Pendulum (van Dalen, 2018).

Figure 2.15: SDOF systems

From Newton's second law, the equation of motion can be formulated. The equation of motion for the mass spring system is shown in eq 2.47.

$$m\ddot{x} + c\dot{x} + kx = F(t) \tag{2.47}$$

In figure 2.15b, the pendulum system is shown. The system consist of a pendulum with length l, a mass m, rotational damping c_r and loaded by a random time dependent moment $M(t)$. The system describes the rotational moment $\theta(t)$. The equation of motion is presented in eq 2.48.

$$ml^2\ddot{\theta} + c_r\dot{\theta} + mgl\theta = M(t) \tag{2.48}$$

Both equations of motion presented in eq 2.47 and eq 2.48 can be reformulated into the Canonical form shown in eq 2.49 in which $\psi(t)$ is the degree of freedom of the system.

$$\ddot{\psi} + 2\zeta\omega_0\dot{\psi} + \omega_0^2\psi = f(t) \tag{2.49}$$

Unforced motion

In case the external forcing $f(t)$ is absent, equation 2.49 reduces to a homogeneous differential equation for which the general solution is given by eq 2.50. The corresponding eigenvalues are given in eq 2.51.

$$\psi(t) = \exp(-\zeta \omega_0 t) \left[\Psi_1 \exp(\omega_0 t \sqrt{\zeta^2 - 1} + \Psi_2 \exp(-\omega_0 t \sqrt{\zeta^2 - 1} \right] \tag{2.50}$$

$$s^2 + 2\zeta \omega_0 s + \omega_0^2 = 0$$
$$s_{1,2} = -\zeta \omega_0 \pm \omega_0 \sqrt{\zeta^2 - 1} \tag{2.51}$$

There are two types of motion possible, this is dependent on the damping ratio ζ. (van Dalen, 2018)

- $\zeta > 1$ (over-critically damped system) **aperiodic motion**

- $\zeta = 1$ (critically damped system) **aperiodic motion**

- $\zeta < 1$ (sub-critically damped system) **damped vibration**

An example of a free vibrating sub-critically damped system is presented in figure 2.16.
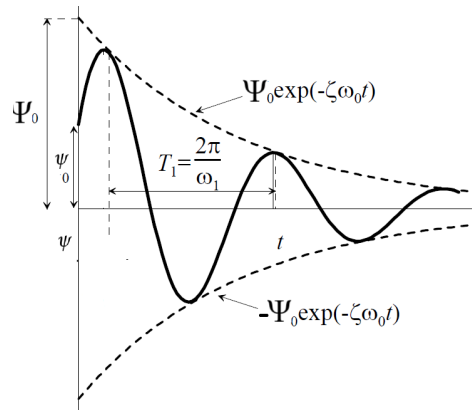
Figure 2.16: Free vibration of a sub-critically damped SDOF system (Metrikine, 2006)

.

Forced motion

In case of external forcing, the general solution consists of a homogeneous and a particular solution. The homogeneous solution is found in eq2.50. The particular solution is found by guessing a solution in the same form as the load with unknown constants. The unknown constants can be solved by inserting the particular solution in the differential equation. (equation of motion). The initial conditions will gradually subside in time and the steady stake solution remains. This can be seen in eq 2.52.

$$\psi_{steady}(t) = \lim_{t \to \infty} \psi(t) \tag{2.52}$$

2.4.2. Lagrange

Motions of particles and rigid bodies are described by Newton's law. Equations of motions can be found with the displacement method. The sum off all forces on the body is equal to the acceleration times the mass of that body. An alternative approach to find the equation of motion for a dynamic system is the Lagrangian formalism (Metrikine, 2006). This formalism is based on the Lagrangian equations which can be found in eq 2.53. The Lagrange's Equations are based upon conservation of energy (Widnall, 2009).

$$\frac{d}{dt} \frac{\partial L}{\partial \dot{q}_s} - \frac{\partial L}{\partial q_s} = Q_s \tag{2.53}$$

where

$$L = E_K - E_P \tag{2.54}$$

in which

L	=	Lagrange function
q_s	=	generalized coordinates and velocities
Q_s	=	generalized forces acting on the system
E_k	=	Kinetic energy
E_p	=	Potential energy

The Lagrangian formalism can be very convenient in case of complex coordinate systems. However Newton's law and Lagrange's equations are fully compatible. (Widnall, 2009).

2.4.3. Tether as a spring

Tethers are flexible construction tension elements which are not able to resist bending loads and can only take axial loads. Because the tether has no bending stiffness, it will deform in a parabolic shape. A 'hanging' tether will reduce the axial stiffness and thus the resistance against displacement, Δl_s, of one of the ends of the tether. The larger the parabolic deformation, the smaller the resistance against displacement of one of the ends. The relation between tether force and displacement of one of the ends is therefore non-linear (Peters, 1993). The non-linear expression between tether force and displacement can be found by using a second order ordinary differential equation (ODE) eq 2.55 which describes the equilibrium of a tether under tension.

$$q(x) = -T\frac{d^2 w}{dx^2} \tag{2.55}$$

For clarification, an overview of symbols is given in figure 2.17.
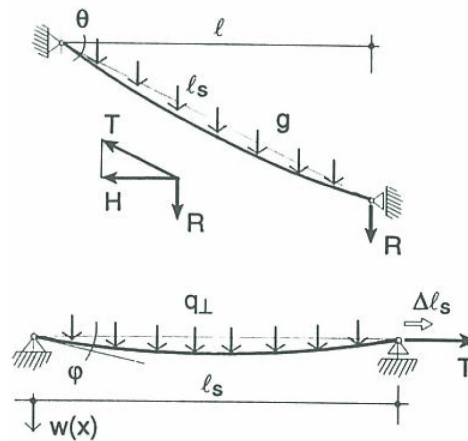
Figure 2.17: Tether definitions of symbols (Peters, 1993).

Because the cable is loaded only by its own weight, which is a constant load, the solution of the displacement $w(x)$ can be found in the form of a parabola found in eq 2.56.

$$w(x) = \frac{g}{2T}(\frac{1}{4}l^2 - x^2) \tag{2.56}$$

The displacement f in the middle of the tether is therefore $w(0.5l) = f = \frac{ql^2}{8T}$. The length of the tether, in this case the parabola, can be determined using eq 2.57

$$s = \int_{-0.5l}^{0.5l} \sqrt{1 + (\frac{dw}{dx})^2}\,dx = l(1 + \frac{8}{3}(\frac{f}{l})^2) \tag{2.57}$$

The actual length of the tether consist of its initial length and the tether elongation. This is expressed in eq 2.58.

$$s = s_0 + \Delta s_e \tag{2.58}$$

To form a relation between tether force and displacement Δl_s, eq 2.56, eq 2.57 and 2.58 are used. The relation is presented in 2.59 (Peters, 1993).

$$T^3 + T^2 EA(1 - \frac{l_s + \Delta l_s}{s_0} = \frac{EA(ql)^2 l\cos\theta}{24 s_0}$$

(2.59)

It should be noted that eq 2.59 is a cubic formula (non-linear!). In figure 2.18, the relation between tether force and displacement Δl_s for a cable is shown. In this figure, (a) represents the relation between elongation and cable force. The axial cable stiffness is indicated with (d).
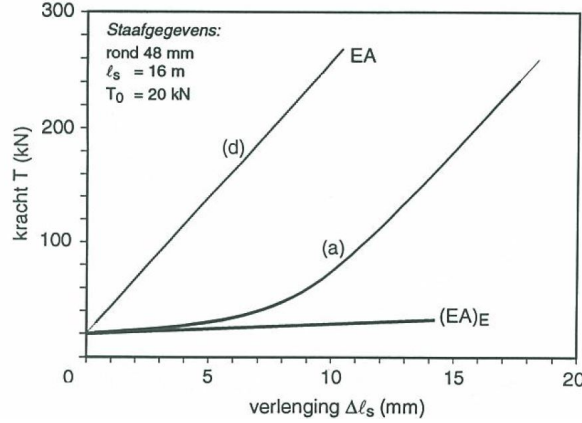
Figure 2.18: Relation tether force T and displacement Δl_s (Peters, 1993).

It can be observed that with small displacements, the resistance will almost stay the same. However when the displacement becomes large, the tether will start to become more and more straight. The slope $\frac{dT}{d\Delta l_s}$ will approach EA, the axial stiffness of the cable.

Analytical solution
Applying the non-linear spring to a dynamic model will give problems in analytically solving. The coupled non-linear second order ODE's can no longer be solved by using homogeneous and particular solutions as used in the 1degrees of freedom (DOF). Analytical solutions give great insight in the mathematical background like natural frequencies, movements, damping etc. To find an analytical solution, the tether spring system can be linearized in the point of interest. The point of interest is defined by the range in which the tether forces can be present. If this range matches with the calculated displacement, the chosen linearized spring is correct. It should be noted that this process is iterative. According to (Peters, 1993), the linearized spring expressed as $(EA)_{sec}$ can be computed with eq 2.60.

$$(EA)_{sec} = \frac{EA}{1 + EA\frac{(gl)^2(T_i + T_j)}{24 T_i^2 T_j^2}}$$

(2.60)

in which

EA	=	Axial stiffness of tether (not of the steel)
T_i	=	Lower bound tether force
T_j	=	upper bound tether force

Please note that if the range of T_i , T_j becomes large, the less accurate the model outcome will be. This could lead to errors and underestimation.

2.4.4. Numerical solutions for non-linear differential equation

A non-linear coupled multi order differential system can be solved numerically. In case that the range of T_i, T_j becomes too large or to control the analytical solution, a numerical computation can be use full. A numerical ODE solver is used to solve the ODE's. The matlab function ode45 can be used (Senan, n.d.). This function implements a Runge-Kutta method with a variable time step for efficient computation. Please note that ode45 is possible for a system of first order ODE's. The equations of motion will be a coupled non-linear second order ODE system which should therefore first be converted to a coupled non-linear first order ODE system. This can be done by means of substitution (Boyce & DiPrima, 2012). An example is done below. Let us define a coupled non-linear second order ODE system of variables $x(t)$ and $y(t)$:

$$\begin{cases} x'' + x' - 5yx = 4 \\ y'' - 5y' - 25x = 5 \end{cases}$$

Now let us define the variables of these functions as follows:

$$\begin{cases} x = x_1 \\ x_1' = x_2 \\ y = x_3 \\ x_3' = x_4 \end{cases}$$

If the previous variables are substituted in the original differential system and all first order terms are separated from the rest of the variables, the following first order non-linear ODE system can be obtained.

$$\begin{cases} x_1' = x_2 \\ x_2' = -x_2 + 5x_3x_1 + 4 \\ x_3' = x_4 \\ x_4' = 5x_4 + 25x_1 + 5 \end{cases}$$

2.5. SFT dynamics

First some common technical SFT terms are explained. Subsequently, the SFT motions and its coordinate system are discussed followed by a META-analysis elaborating studies which modelled the dynamic response of the SFT.

2.5.1. Technical SFT terms

- The buoyance to weight ratio (BWR) ratio is the ratio between the Archimedes force and the mass of the structure. This BWR can be computed with eq. 2.5.1.

$$BWR = \frac{V\rho}{m} \tag{2.61}$$

in which

ρ =   Density of water
m =   Mass of tunnel
V =   Displaced water volume

- Tethers are mooring cables which are connected to the SFT and anchored in the soil to prevent the tunnel from floating up.

2.5.2. SFT coordinate system and motions

The SFT is connected by tethers which are anchored at the seabed. The tethers are fexible which makes it possible for the tunnel to move in multiple directions below the water surface. Observing a 3D SFT system, six degrees of freedom are possible. The multi degrees of freedom (MDOF) and its coordinate system are shown in figure 2.19.
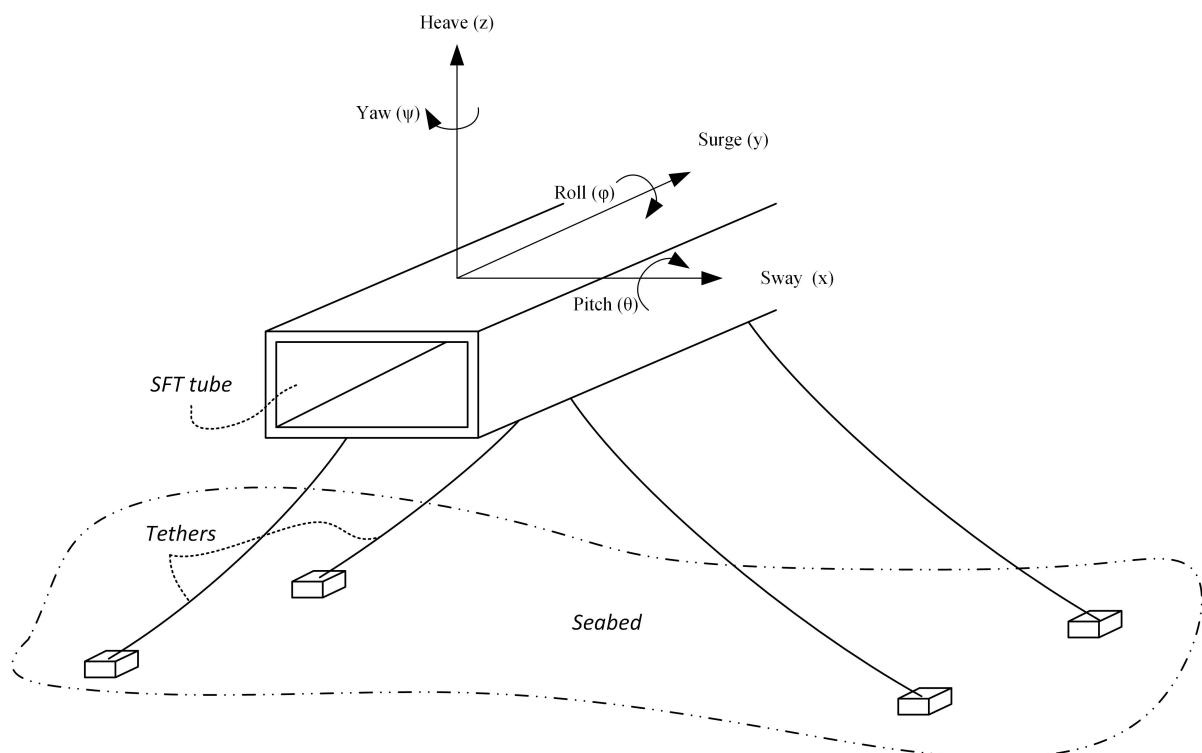
Figure 2.19: schematization of SFT as MDOF system *(own figure)*

2.5.3. META-Analysis on dynamic modelling SFT

In this section, multiple scientific studies addressing the dynamic response of a SFT are analysed. The research that has been performed is widely spread. The scope of this META-Analysis is on a SFT that is hydraulic forced. Traffic loads, explosions, pure seismic loading or other special loads are not included. The most important differences between all these studies is:

- **Forcing**
  Globally three different forcing types are applied on the dynamic models. The first one is a modified Morison's equation often combined with a vortex induced vibration. The second forcing type that is common used are the RANS equations. This forcing type is mostly a CFD model combined with a dynamic model. With these models, the fluid structure interaction can be analysed in great detail. The third forcing type is used in laboratories where small scale flume experiments are executed. In section 2.2.1, the velocity potential theory was used to determine the forcing on a submerged body. However no dynamic response study has been executed based on this theory.

- **Dynamic system**
  Globally three types of dynamic systems are used to simulate motions or forces on the SFT. The first common type dynamic model is a 3DOF model that contains sway, heave and roll. The EOM is obtained by the displacement method or the Lagrangian method. The second type of dynamic system is the Finite Element Method (FEM). The tunnel cross-section is described by a mesh in which the object is subdivided into smaller finite elements. The third dynamic model that is widely studied is the beam model. The Euler Bernoulli beam model is used to describe the longitudinal behaviour of the tunnel under hydrodynamic loading. The beam is supported by springs, representing the tethers. In some research studies, the tethers are also decoupled from the tunnel body and investigated separately.

- **Solution method** The dynamic system can be solved analytical or numerical. This is also depending on the chosen forcing and dynamic system. A CFD model needs to be solved numerically because of its complexity. However continues systems or 1 - 3 DOF systems can be solved analytically if the behaviour is linear. The analytical solution helps to better understand the behaviour of the system.

- **Research objective** Globally two types of objectives can be found in all studies. The response of the tunnel body in terms of displacements and the response of the tethers in terms of forces.

In table 2.2 - 2.4 an overview of the most diverse researches on the dynamic response of a SFT is given.

Table 2.2: META-Analysis on dynamic modelling SFT

Summary	Equation of motion	Model schematization
(Lu et al., 2011) This research investigates the slack of a SFT. Under severe sea wave conditions, mooring tethers could have no tension and this could cause struture failure during the service lifetime. In this study, the SFT is anchored by four inclined tethers which give a nonlinear problem. Lagrange is used to form the equations of motions. This consist of a horizontal, vertical and rotational coupled system of equations. The forcing of the system is due to wave loads, described by Modified Morison. Effects of two fundamental structure parameters is investigated, the BWR and the inclined mooring angle. The solution of the problem is found analytically.	$$\begin{cases} m\ddot{x} + \frac{1}{2}\sum_{i=1}^{4} K_i(\Delta L_i)\frac{\partial(\Delta L_i^2)}{\partial x} = f_x a \\ m\ddot{y} - \left(w - \frac{1}{2}\sum_{i=1}^{4} K_i(\Delta L_i)\frac{\partial(\Delta L_i^2)}{\partial y} \right) = f_y a \\ \frac{1}{2}mR^2\ddot{\varphi} + \frac{1}{2}\sum_{i=1}^{4} K_i(\Delta L_i)\frac{\partial(\Delta L_i^2)}{\partial \varphi} = f_\varphi a \end{cases}$$ Wave forcing: *Modified Morison*	
(Peng et al., 2013) This research studies the interactions of water waves with a submerged floating breakwater moored by inclined tethers. A dynamic model is used consisting of 3 degrees of freedom, surge, heave and pitch. Two different breakwater shapes are elaborated, circular and rectangular. The effect of the breakwater on the wave field is investigated. The wave field around the submerged breakwater is modelled by the Navier-Stokes equations. The dynamic model combines a direct-forcing immersed boundary method, volume of fluid method and the dynamic breakwater model. The system is solved numerically and can be seen as a CFD model.	$\sum M_{c,g} = \sum M_{cg,x} + \sum M_{cg,z} + \sum M_{cg,T} = J_{FB}\alpha_{FB}$ $\sum F_X = m\alpha_x = H_1 + H_3 - H_2 - H_4 + 2(T_2\cos\theta_2 - T_1\cos\theta_1)$ $\sum F_Z = m\alpha_z = V_1 + V_3 - W - V_2 - V_4 - 2(T_2\sin\theta_2 + T_1\sin\theta_1)$ Wave forcing: *Reynolds-averaged Navier–Stokes equations* $\frac{\partial u_i}{\partial x_i} = Q$ $\frac{Du_i}{Dt} = -\frac{1}{\rho}\frac{\partial p}{\partial x_i} + 2\nu\frac{\partial D_{ij}}{\partial x_j} - \frac{2\nu}{3}\frac{\partial Q}{\partial x_i} - g_i - \gamma u_i\delta_{i2} + L_i$	
(Mandara et al., 2016) The behavior of a SFT to a water current is investigated in this research. This is done based on complex numerical analyses based on the CFD and the FEM method. Two cross-sections are investigated, circular and elliptical. The tunnel cros-section is anchored by 4 tethers to the sea bottom. The wave loading on the tunnel is done with the RANS equations. Displacements and cross-sectional hull stresses can be computed numerically.	Wave forcing: *Reynolds-averaged Navier–Stokes equations*	
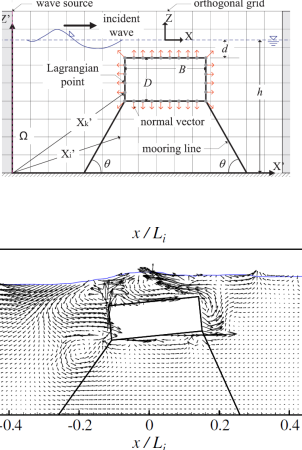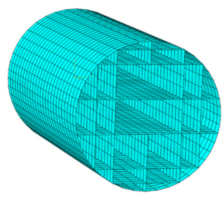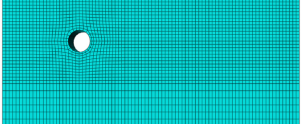
Table 2.3: META-Analysis on dynamic modelling SFT

Summary	Equation of motion	Model schematization
(Xiang & Yang, 2017) In this research, the SFT is treated as a beam on elastic foundation under impact load. The beam has three degrees of freedom, horizontal, vertical and torsion. The equation of motion are obtained by Hamilton principle. The hydraulic loading is established with Morison's equation. With the model parameters such as, cable angle, BWR anchorage stiffness and hydraulic resistance the dynamic response is studied. The model is validated with a CFD model. A similar research is done by (Xiang et al., 2018) which used the same model to predict the effect of a snapping tether line.	$$\begin{cases} EI_z\frac{\partial^4 y}{\partial x^4} + \frac{\partial^2 y}{\partial t^2} + c_y\frac{\partial y}{\partial t} + k_y y = P_y(t)\hat{\delta}(x-\xi) - \frac{1}{2}\rho_l C_D\frac{\partial y}{\partial t}\left|\frac{\partial y}{\partial t}\right| \\ EI_y\frac{\partial^4 z}{\partial t^4} + m\frac{\partial^2 y}{\partial t^2} + c_z\frac{\partial z}{\partial t} + k_z(z - r\varphi\cos\beta) = P_z(t)\hat{\delta}(x-\xi) - \frac{1}{2}\rho_l C_D\frac{\partial z}{\partial t}\left|\frac{\partial z}{\partial t}\right| \\ m_0 a^2\frac{\partial^4 \varphi}{\partial t^4} - GI_p\frac{\partial^2 \varphi}{\partial x^2} + c_\varphi\frac{\partial \varphi}{\partial t} + k_\varphi\varphi - k_z rz\cos\beta = P(t)\lambda\hat{\delta}(x-\xi) \end{cases}$$ Wave forcing: *Morison equation*	1(a) Front view 1(b) Side view
(Oikou, 2014) The goal of this research is to study the vortex-induced vibrations on a slender cylindrical cylinder. The slender submerged cylinder is modelled as a Euler Bernoulli beam which is pinned at the boundaries and placed in a uniform stationary flow. The forces on the cylinder are modelled with Morison equation in which a cross-flow vortex force is implemented. The response frequencies and displacements are obtained by model simulations. Also the normal mode shapes of the cylinder are investigated.	$$(m + m_a)\frac{\partial^2 w_x}{\partial t^2} + b\frac{\partial w_x}{\partial t} + EI\frac{\partial^4 w_x}{\partial z^4} - T\frac{\partial^2 w_x}{\partial z^2} = F_{VX},$$ $$(m + m_a)\frac{\partial^2 w_y}{\partial t^2} + b\frac{\partial w_y}{\partial t} + EI\frac{\partial^4 w_y}{\partial z^4} - T\frac{\partial^2 w_y}{\partial z^2} = F_{VY},$$ Wave forcing: *Morison equation + Vortex (distributed wake oscillator)*	
(Muhammad et al., 2017) In this research, the effect of cable stiffness on the displacement of the SFT is evaluated. To model the SFT, a part of the tunnel is analysed. The left and right boundary are pinned and can only rotate while the mid of the beam is able to move by extending the cables. The equations of motion are obtained by the displacement method. The forces on the SFT are permanent loads, hydrodynamic loads and seismic loads. The hydrodynamic load is described by modified Morison and the seismic load is described by a time signal.	$$[M + M_a]\{\ddot{q}\} + [C]\{\dot{q}\} + [K_e + K_m]\{q\} = \{f\} + \{f(q,t)\} - [M + M_a]\{I\}\{\ddot{q}_g\}$$ Wave forcing: *Modified Morison* Seismic forcing: *Time signal*	

Table 2.4: META-Analysis on dynamic modelling SFT

Summary	Equation of motion	Model schematization
(Remsheth et al., 2005) The behaviour of the SFT to wave loading is studied based on a stochastic dynamic respose analyses. An earthquake response analysis is studied by finite element modelling of the bridge and its surrounding fluid. The effect of the wave angle and shortcrestedness of waves is investigated. The need for integrated versus simplified modelling in earthquake response modelling is the main scope of the research. The fluid around the structure is described by the RANS equations and the earthquake is described by a time signal of an earthquake in Canada 1985. The SFT that is modelled has a radius of curvature of $12000m$ and the cross sectional profile of the crossing is of arbitrary shape.	$$\int_0^{+\infty} \mathbf{M}(t-\tau)\ddot{\mathbf{r}}d\tau \;+\; \int_0^{+\infty} \mathbf{C}(\mathbf{r},\dot{\mathbf{r}},t-\tau)\dot{\mathbf{r}}d\tau$$ $$+\;\; \mathbf{K}(\mathbf{r})\mathbf{r}(t) = \mathbf{Q}(t)$$ Wave forcing: *Reynolds-averaged Navier–Stokes equations* Seismic loading: *Nahanni earthquake (Canada 1985) time signal.*	
(Yan et al., 2016) In this research, the vibration response of a SFT anchoring tether under the action of current and parametric vibration is studied. The dynamic system consist out of a partial differential equation which describes the cable vibration and a equation of motion describing the tunnel body as a rigid mass. The forcing on the cable is described by a vortex induced vibration and the damping on and added mass of the cable described by Morison.	$$\begin{cases} \ddot{y} + \left[\omega_n^2 + \frac{EA(n\pi)^2 Z}{\bar{m}L^3}\right]y + \frac{C}{m}\dot{y} + \frac{2D_n}{L\bar{m}} + \frac{EA\pi^4}{4\bar{m}L^4}y^3 = \\ \qquad\qquad \frac{2}{\pi\bar{m}}\rho DC_L(v\sin\theta)^2\cos\omega_v t \\ \ddot{Z} + 2\omega_M\xi_M\dot{Z} + \omega_M^2 Z + \frac{EA\pi^2}{4ML^2}y^2 = 0 \end{cases}$$ Wave forcing: *Vortex induced vibration* Water body damping force and additional mass force: *Morison equation*	
(Drost, 2019) An experimental study on the hydrodynamics and kinematics of a submerged rectangular cylinder in a wave-current environment has been performed. The first part of the study consist of multiple flume experiments on a fixed submerged rectangular cylinder subjected to a current, regular wave and combined wave-current environment. The second part of the study consist of multiple flume experiments on a tethered supported submerged rectangular cylinder subjected to a current, regular wave and combined wave-current environment. The tethered supported SFT consists of two inclined tethers. Several parameters are varied during both tests. A elaborated summary of this research can be found in appendix D.	Wave forcing: *Wave generator* Current forcing: *Current inflow + weir*	Fixed flume experiment Tethered supported flume experiment
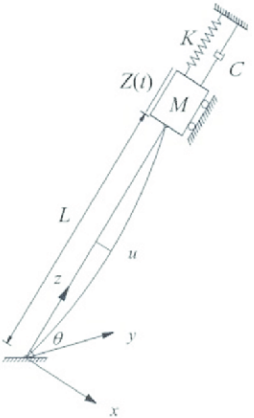
2.6. Reference projects
The concept of a SFT is still under development and this type of structure has never been built so far. Offshore structures like floating wind turbines, single buoy mooring stations and wave energy converters are based on the same well-known technology and a lot of experience is gathered in the past years. A short description of these offshore structures is given in this section.

2.6.1. Floating wind turbine
The fluid structure interaction in combination with mooring tethers can be observed in many offshore structures, for example in the offshore wind industry (Savenije et al., 2010). In figure 2.20a, a spar-type floating wind turbine is shown. It can be observed that the tethers are parabolic shaped, which is because of the self weight of the mooring tethers. The wind turbine can be schematized for the different reaction forces. These schematized systems are presented in figure 2.20b. Because the turbine is floating at the water surface, it has a buoyancy reaction force acting as a spring. The mooring tethers act as springs preventing the platform from drifting of. The dynamics of the turbine rotor result in aerodynamic damping. The dynamics of the submerged structure results in hydrodynamic damping.

(a) Fixed and floating wind turbine

(b) Dynamic system spar-type wind turbine
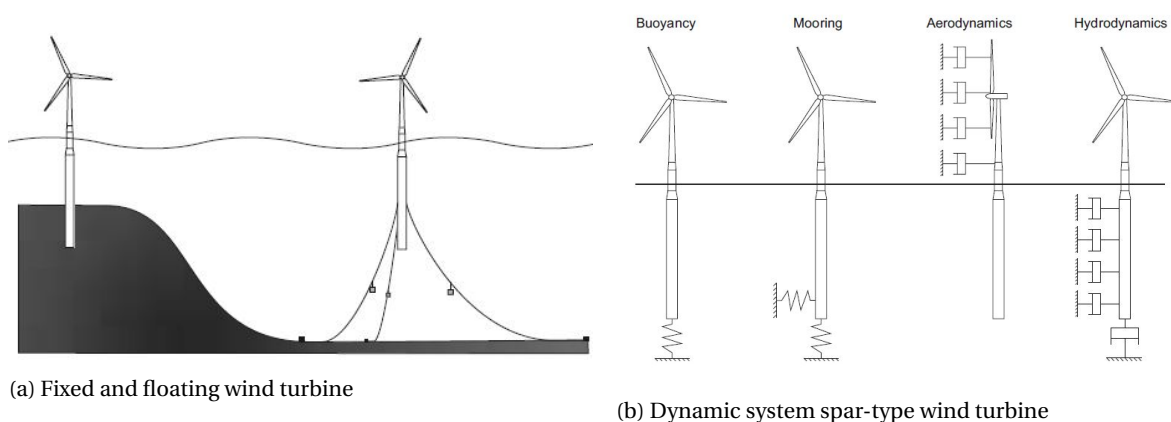
Figure 2.20: Spar-type floating wind turbine (Savenije et al., 2010).

It should be noted that a floating wind turbine is physically different from a SFT. The buoyancy of a submerged body is constant in time because it will always stay below the water surface and thus displace the same amount of water. A buoyancy spring is therefore not present in SFT model. Because the structure is submerged, there will be no aerodynamic reaction forces. The mooring and hydrodynamic reaction forces can be modeled in a similar way for a SFT.

2.6.2. Single buoy mooring
Ocean mooring systems can be divided into single and multi-point mooring systems. An impression of a single buoy mooring configuration is present in figure 2.21a. These mooring systems exhibit nonlinear behaviour which are due to the non-linearity of the tethers, due to the damping, due to the excitation force or a combination of them. The non-linearity of the system leads to a complex dynamic response. A moored vessel will be excited by waves, wind and current which gives slack and taut in the mooring tethers. These flexible offshore structures are investigated in multiple studies. (Umar & Datta, 2002) studied the nonlinear dynamic response of a moored buoy. To model the dynamic response, a single degree of freedom system (sway) is used in combination with a 5th order anti-symmetric polynomial which describes the behaviour of the mooring tethers. The buoy is excited by first and second order wave forces. A schematization of the mooring system is presented in figure 2.21b.

The behaviour of the single buoy mooring and the SFT is similar. Both systems are anchored with long mooring tethers and forced by waves and current. The largest differences are: the forcing of the vessel on the buoy is not present on the SFT. The buoyancy force on the SFT is constant in time while the buoyancy force of the buoy is dependent on the heave motion.

(a) Impression single buoy mooring configuration (Umar & Datta, 2002).
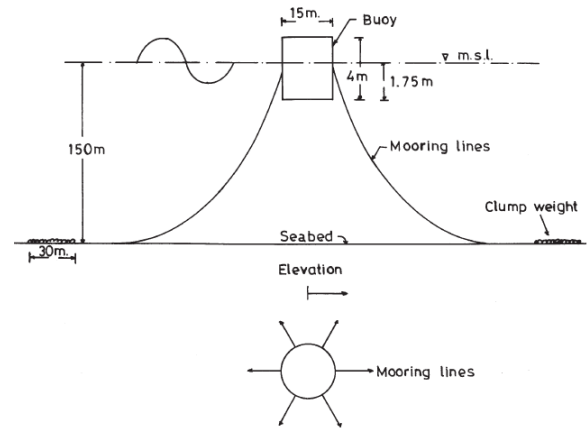
(b) Model schematization single buoy mooring (Umar & Datta, 2002).

Figure 2.21: Single buoy mooring

2.6.3. Wave energy converter

The wave energy converter is very similar to the SFT. Multiple types of wave energy converters have been developed the last years. The wave energy converter as a submerged buoy will be used as reference project, an impression is presented in figure 2.22a. This type of converter converts the motion of the buoy into energy. The wave energy converter and the SFT have a different function but the dynamic behaviour is similar, both systems tend to float up but mooring tethers keep the structure fully submerged. Both systems are forced by waves and current and no other external forcing is present. The largest difference is the length of the structures, the SFT is a long structure while the wave energy converter is more or less cubic. Multiple studies are carried out to model the dynamic response of the submerged wave-energy converter. (Rijnsdorp et al., 2018) studied the wave-induced response of a submerged wave energy converter using a non-hydro static wave-flow model. This study provides the first step towards simulating the interaction between waves and current and the wave energy converter in a numerical model. The fluid forces are modelled by the RANS equations. A model schematization is presented in figure 2.22b.
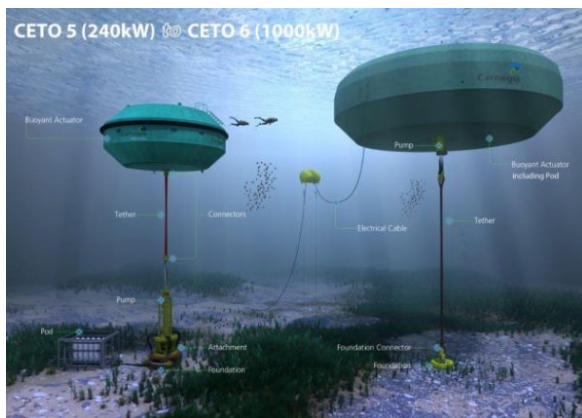
(a) Impression wave energy converter (Korane, 2017).
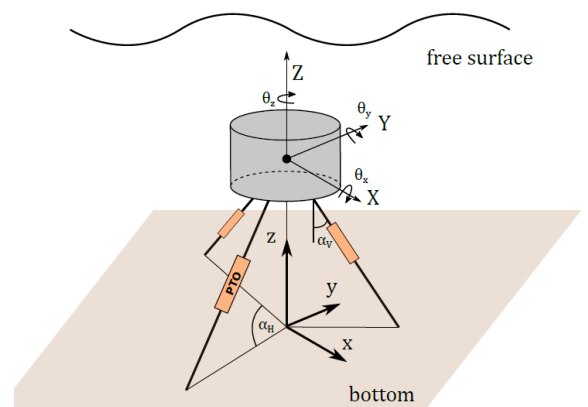
(b) Model schematization wave energy converter (Rijnsdorp et al., 2018).

Figure 2.22: Wave energy converter

3

Model description

In this chapter the dynamic model, that will be used to compute the dynamic response of the submerged floating tunnel (SFT), is elaborated. First an introduction is given on research that has been performed on the dynamic response of the SFT. Second, a research overview and opportunities are visualized followed by the dynamic model choice that is used in this research. The model set-up is explained with a flow diagram. Finally the different modules of the model are explained. Background information on the wave module is provided in appendix A. The background of the dynamic module is provided in B. The background of the coupling module is provided in appendix ??.

3.1. Introduction
Many research is done on dynamic modelling of a SFT in a wave-current environment. Various methods are applied to obtain a suitable dynamic model. In these models the main differences are the forcing model, dynamic system, the solution method and the research objective. (Remsheth et al., 2005) studied the dynamic response based on a Finite Element Method (FEM) model with Reynolds-averaged Navier-Stokes (RANS) equations and earthquake forcing. A similar model was applied by (Mandara et al., 2016), however in this research not only the displacements but also the cross-sectional hull stresses are computed. The cross-sectional dynamic response is often studied with a 3degrees of freedom (DOF) system. (Lu et al., 2011) used a 3 DOF dynamic model with modified Morison forcing to investigate the slack of a circular SFT. (Peng et al., 2013) used a similar 3DOF model with a rectangular shape but with a RANS forcing. Besides the cross-sectional dynamic response studies, also the longitudinal dynamic behaviour has been studied. (Oikou, 2014) treated the SFT as a beam on elastic foundation with horizontal and vertical deflection and applied a combined Morison cross-flow vortex induced vibration forcing. (Xiang & Yang, 2017) added a torsion beam equation and investigated impact loading. The effect of a snapping tether line with a identical model was studied by (Xiang et al., 2018). (Muhammad et al., 2017) modeled the beam as a multi degrees of freedom (MDOF) system with Morison forcing in combination with a seismic forcing signal to analyse the effect of cable stiffness on the displacement. The behaviour of the tether due to vortex induced vibration is investigated by (Yan et al., 2016). Besides mathematical models, also physical model experiments are applied to study the dynamic behaviour. (Drost, 2019) performed an experimental study on the hydrodynamics and kinematics of a submerged rectangular cylinder in a wave-current environment.

3.2. Research overview and opportunities
All research that has been done to analyse the dynamic response of a SFT in a wave-current environment can be categorized based on forcing model and dynamic system. In table 3.1 an overview is given. In this table, a green check mark means that the combination of forcing model and dynamic system is already studied. Symbols for computational time, mathematical complexity, costs and wave length applicability are inserted in the table to show the properties of the chosen combination.

It can be observed that many combinations are already studied. Complex Computational Fluid Dynamics (CFD) models are made in combination with FEM and 3DOF dynamic systems. These models require long computational time, are complex to construct and understand and costly. Morison's equation is used for all

Table 3.1: Overview of research with corresponding properties

Forcing model

Dynamic system	CFD RANS		Morison's equation		Potential theory		Physical model	
Continues beam model /MDOF		✚✚ ⊖ ●	✓	∿ ✚ ⊖		✚✚ ✓	✓	●●
FEM model	✓	✚✚ ⊖	*(not applicable)*					
3DOF model	✓	✚	✓	∿	✓ (No tethers)	✚✚	✓	●
1DOF model			∿			✚	✓	●

Legend: ✓ Investigated by other researchers — ⊖ Computational time — ✚ Complex — ● Costly — ∿ No short waves

types of dynamic systems except for 1DOF dynamic systems. The potential theory is not used allot in the research field of the SFT. Complex mathematics is needed. Physical models are used for each dynamic system. It can be seen that there is lots of potential for 1DOF models. These models are relative easy to construct, low in costs, fast computational time and give great insight in fundamental behaviour. Morison's equation, and potential theory can be applied as forcing type to the 1DOF system. CFD forcing requires special computer software and is not desirable because it does not give good understanding of the fluid structure interaction on theoretical level. Combining a single degree of freedom (SDOF) system with a Morison or potential forcing model is a highly attractive combination that has still not been implemented in any dynamic analysis of the SFT. In table 3.1, this combination is indicated with a red marker. Morison's equation forcing method is not suitable for short waves and potential theory is based on complex mathematics. Combining both forcing methods with a SDOF system would result in a computational fast, not costly and new approach which is able to describe the dynamic response of a SFT for a broad range of wave lengths without using complex mathematics.

3.3. Dynamic model choice

To study the dynamic response of the SFT tunnel in a wave-current environment, a SDOF dynamic system is used. A global model schematization can be found in figure 3.1, outlined with a green framework.
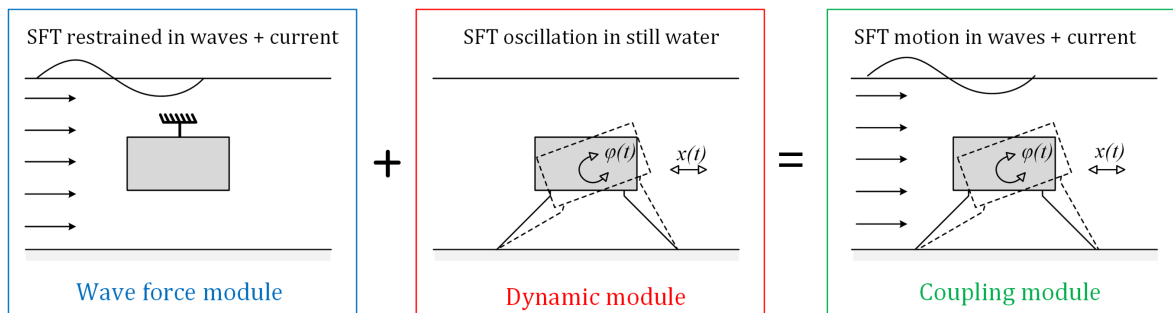
Figure 3.1: Superposition of hydrodynamics and wave-current loads on SFT

The dynamic system that is used has one degree of freedom which describes the coupled roll $\phi(t)$ and sway $x(t)$ of the tunnel in the x, z plane. The forcing on this dynamic system is described by a combination of Morison's equation and the potential theory. Both theories make use of the linear wave theory. Morison's equation is modified which makes it applicable for short waves and able to describe rotational moments.

Both applications are not possible with the classical Morison equation. Because the SFT motion is assumed to be linear, the motion of the SFT in a wave-current environment can be decoupled in two parts. The first describes the SFT restrained in a wave-current environment. The second part describes the SFT oscillation in still water. The schematization of the two decoupled parts can be found in figure 3.1.

The dynamic model details and its advantages and disadvantages of this choice are summed up:

Model details	**Advantages**	**Disadvantages**
• Forcing model: modified Morison equation in combination with potential theory.	• Applicable for short waves.	• No longitudinal effects.
• Dynamic system: 1DOF dynamic system describing coupled roll and sway.	• Possibility to describe rotational moment	• Heave motion cannot be studied.
• Superposition of hydrodynamics and wave-current loads.	• Fast computational time.	• Effect of the structure on the wave field cannot be studied.
• Waves are described by linear wave theory	• Simple dynamic model.	• Only linear waves can be studied.
	• Convenience of physical interpretation.	
	• Engineering tool.	

3.4. Model set-up

The dynamic model is set up to study the dynamic response of a rectangular tether anchored SFT in a wave-current environment. The dynamic SFT model consist of a wave force module and dynamic module. Both modules are coupled by a coupling module. The three modules correspond to the superposition of hydrodynamics and wave-current loads on the SFT which are presented in figure 3.1. Each module is elaborated with an extensive flow chart. Figure 3.2 shows the flow chart of the model set-up. In this figure, all modules are identified with the same colour as in figure 3.1. The flow chart is subdivided into three parts, input, dynamic SFT model and the output. In the flow chart, three different shapes are used, a rectangle (contains information), a circle (function) and a diamond (measurement data). The flow chart diagram is discussed briefly is separate paragraphs.
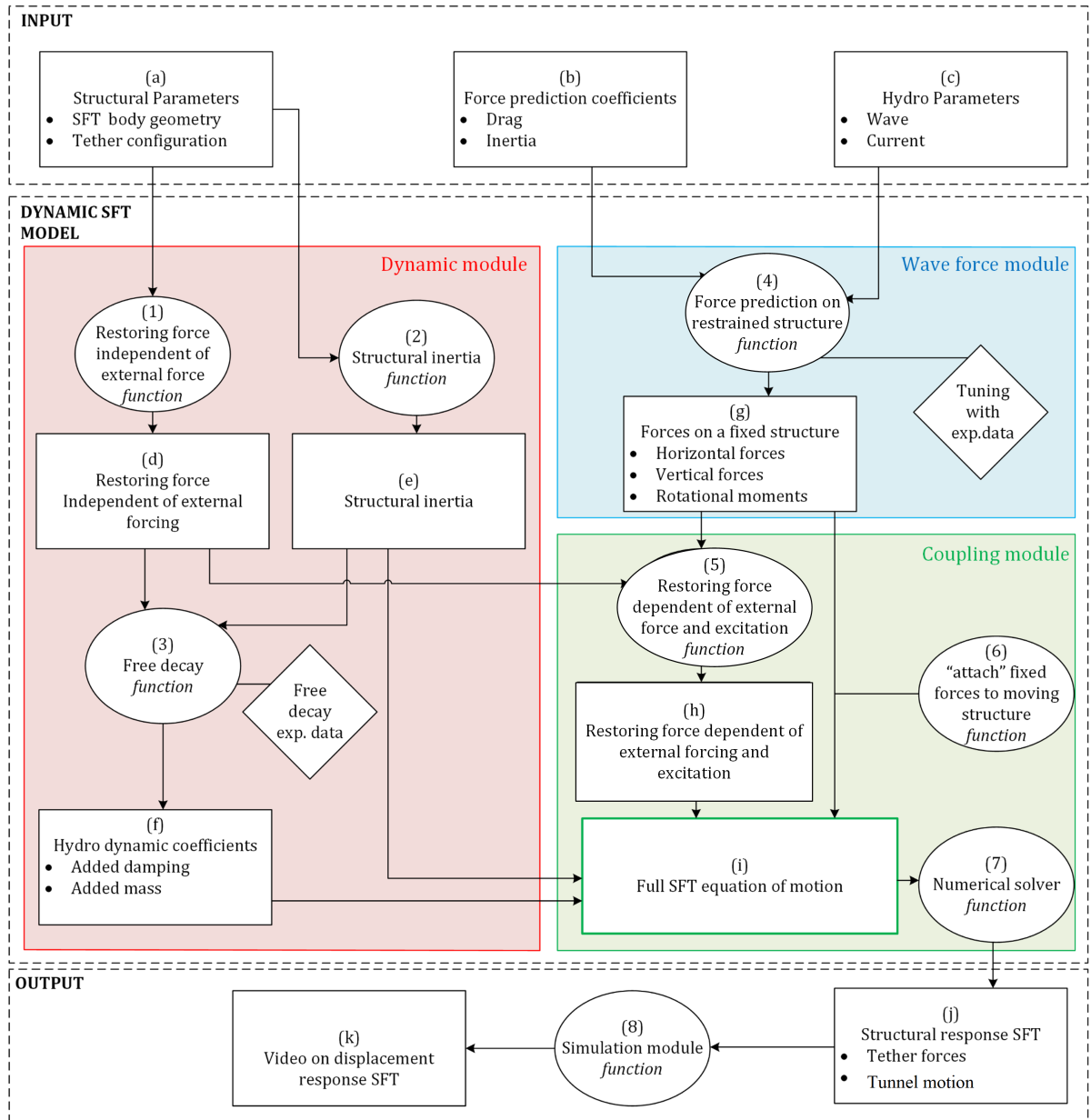
Figure 3.2: Flow chart of model set-up

3.4.1. Input

The input of the model can be categorized in structural parameters (*a*), force prediction coefficients (*b*) and hydro parameters (*c*). An overview of these parameters and some numerical values are given in table 3.2. A schematization of the SFT with parameter definitions is provided in figure 3.3. The hydro parameters are not numerical valued because these parameters will be varied during the parametric study. The structural parameters have the same dimensions as the physical small scale flume experiments (Drost, 2019). Some of the structural parameters are also varied during the parametric study, in this case the model dimensions from the scale experiments are presented. The force prediction coefficients that are used are gained from literature and tuned on the measured data from (Drost, 2019). The hydro dynamic coefficients, indicated in figure 3.2 with (*f*), are not categorised as input parameters. The value of these parameters is determined based on the physical model experiments and discussed in section 3.7.

Table 3.2: Input parameters dynamic SFT model

Parameter	Value	Unit
Structural parameters		
Height (b)	0.40	[m]
Width ($2a$)	0.16	[m]
Length (L_t)	0.792	[m]
Mass (m)	33.7	[kg]
Submerged depth (s_1)	0.175 - 0.35	[m]
BWR	1.51	[-]
Tether angle(α_T)	30-70	
Connection height (ϵ)	0.01	[m]
Connection width (γ)	0.06	[m]
Force prediction coefficients		
Vertical hydrodynamic mass (C_{mz})	1.45	[-]
Horizontal hydrodynamic mass (C_{mx})	1.35	[-]
Drag (C_d)	2.0	[-]
Current drag ($C_d c$)	2.1	[-]
Hydro Parameters		
Wave height (H)	-	[m]
Wave period (T)	-	[s]
Water depth (h_1)	0.7	[m]
Current velocity (u_c)	-	[m/s]
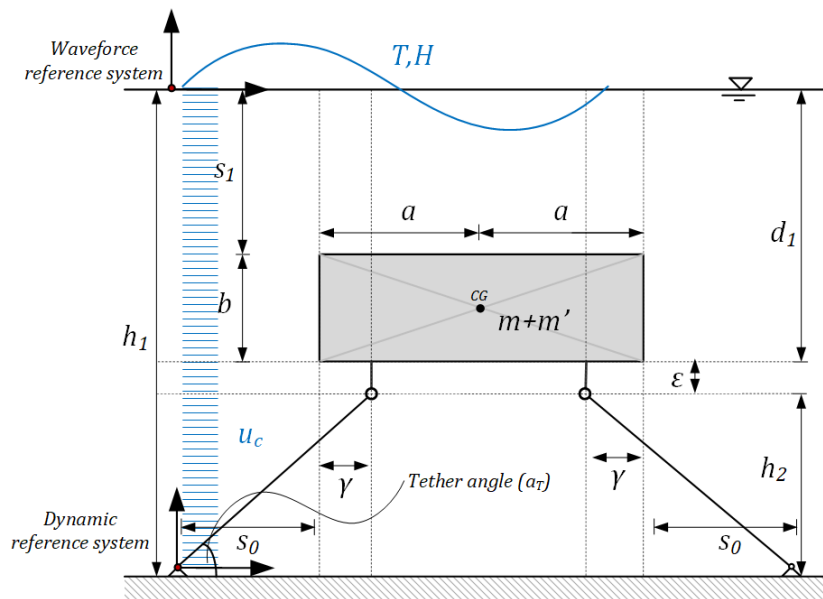
Figure 3.3: Schematization of SFT with parameter definitions.

3.4.2. Dynamic SFT model

In this section, the dynamic SFT model is elaborated. All different functions in the wave force module, dynamic module and coupling module are described separately.

(1) Restoring force independent of external force *function* **Dynamic module**
The restoring force, which is caused by the tether forces and the buoyancy force, is computed. The restoring force is present in case the structure is displaced out of its equilibrium position. However, no external forcing is taken into account. External forcing changes the tether forces and thus the restoring force. The restoring force independent of external forcing is stored in (d).

(2) Structural inertia *function* **Dynamic module**
The SFT has inertia while it moves. This is dependent on the geometry, mass and tether configuration. This function determines the inertia which includes translation and rotation. This information is stored in (e).

(3) Free decay *function* **Dynamic module**
The restoring force (d), independent of external forcing, and the structural inertia (e) are used to compute the hydro dynamic coefficients. Added damping and added mass are found by means of calibrating the model with free decay tests from (Drost, 2019). The restoring force does not need to be dependent on the external forcing because there is no external forcing present in a free decay test. The hydro dynamic coefficients are stored in (f).

(4) Force prediction on restrained structure *function* **Wave force module**
In this function, the forces on a restrained SFT are determined. The force determination is based on a combination of the potential flow theory and Morison's equation. Morison's equation is modified for short waves. The drag and inertia coefficients are calibrated with experimental data from (Drost, 2019). The forces on the restrained structure containing: horizontal forces, vertical forces and rotational moments, are stored in (g).

(5) Restoring force dependent of external force and excitation *function* **Coupling module**
The force independent restoring force is advanced by including the external forcing. Waves and current gives forces in the tethers which changes the restoring force. This information is stored in (h).

(6) "Attach" fixed forces to moving structure *function* **Coupling module**
The forces on the SFT are determined for a restrained submerged structure. These forces are attached to the dynamic model. If the model moves to the right, the forces move with the structure.

(i) Full SFT equation of motion **Coupling module**
The information containing, structural inertia (e), hydro dynamic coefficients (f), forces on fixed structure (g) and restoring force (h) is combined to form one equation of motion, describing the coupled rotational and translation movement of the SFT body.

(7) Numerical solver *function* **Coupling module**
The full equation of motion is numerically solved with Runge–Kutta 4 method. The dynamic SFT model computes the tether force response and the displacement response. The solution is stored in (j).

3.4.3. Output

The output contains the tether force response and the tunnel motion response. The tunnel motion consist of roll motion and a sway motion. Each motion contains accelerations, velocities and displacements. The displacement response is simulated with a simulation function (8). A video is generated which shows the dynamic response in the time domain. This video is stored in (k).

3.5. Model assumptions

The model assumptions are treated separately per module. The coupling module is not discussed because it is based on the assumptions of the wave force module and the dynamic module.

Wave force module

- Wave-current exciting forces and moments are produced by linear waves and uniform currents coming in on the restrained body.

- Velocity potential is not influenced by the presence of the structure.

- In-line friction contribution is neglected.

- Vortex shedding due to separation of flow is neglected.

- Flow along the tethers does not contribute to the wave-current forcing.

- The wave and current direction is always perpendicular to the tunnel structure.

- Current has no influence on the velocity potential

Dynamic module

- Hydro dynamic damping and hydro dynamic added mass, which causes extra inertia, are induced by the harmonic oscillations of the rigid body, moving in the undisturbed surface of the fluid.

- SFT oscillations do not influence the undisturbed velocity potential. (No radiated potential)

- The tunnel cross section is a ridged body with an equally distributed mass at each location of the cross section.

- The tunnel is pinned down by two inclined tethers which have an infinite axial stiffness, which implies no extension of tethers. The tethers are therefore rigid constrains.

- The self weight of the tethers is neglected.

- Small rotations, $\theta < 0.1$ [rad].

- Structural damping is neglected.

- Longitudinal effects are neglected.

- No snapping lines.

- Hydrodynamic damping is assumed to be constant.

- Hydrodynamic added mass is assumed to be constant

3.6. Wave force module

In the wave force module, the forces due to waves and current on the restrained SFT are determined. The SFT is forced by linear waves and uniform current. Both types of forcing are separated and treated in different sections.

3.6.1. Wave forcing

The tunnel body is attacked by a normal incident linear wave train of amplitude ζ and frequency ω. The wave loading creates a horizontal force $F_{w,x}$, vertical force $F_{w,z}$ and moment $M_{w,y}$ with respect to the metric centre of the SFT. The wave forces and their components are presented in eq 3.1. The three equations also show which theory is used to determine each force component.

$$
\begin{aligned}
F_{w,x} &= \boxed{F_{Krylov,x}} & \boxed{+ F_{drag,x} + F_{hydrod,x}} \\
F_{w,z} &= \boxed{F_{Krylov,z}} & \boxed{+ F_{drag,z} + F_{hydrod,z}} \\
M_{w,y} &= \boxed{M_{Krylov,y}} & \boxed{+ M_{drag,y} + M_{hydrod,y}}
\end{aligned}
$$

<div align="center">
Velocity potential   Modified Morison
</div>

$$(3.1)$$

A graphical visualization of eq 3.1 is given in figure 3.4. In here, the undisturbed pressure, acceleration of water and velocity of water are presented.
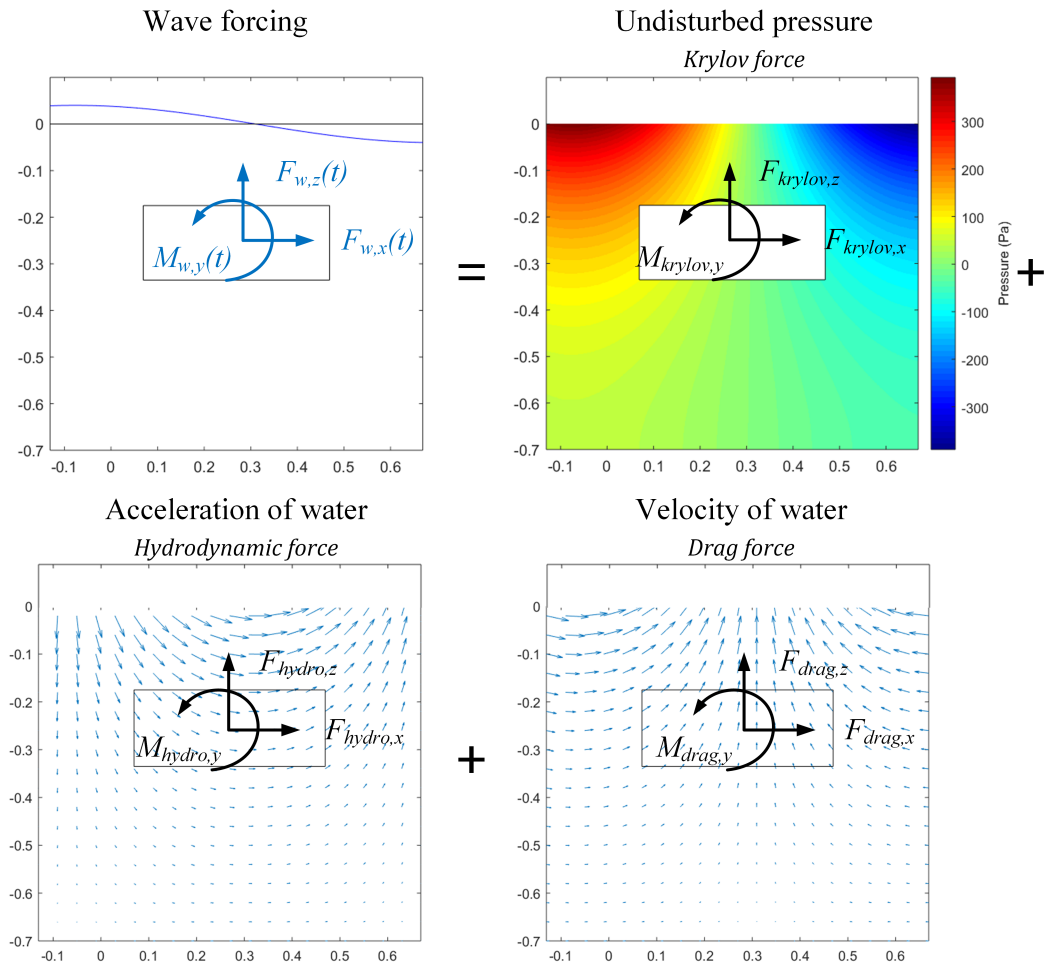
Figure 3.4: Wave force components. (Top left) Total wave force with visualized wave. (Top right) Krylov force, (Bottom left) Hydrodynamic force, (Bottom right) Drag force. Simulation performed with; $s_1 = 0.175m$, $H = 0.08m$, $T = 1.0s$

As can be seen in eq 3.1, each wave force is described by three force components. These three force components are similar to the force components that are known from the classical Morison's equation; Krylov

force, drag force and hydrodynamic force. However it can be observed that an extra force equation has been added, namely the wave moment. Besides the extra force equation, each force component is modified. The method, addressed as modified Morison, has two large advantages compared to the classical Morison equation.

- Modified Morison is able to compute the rotational moments for each force component. The classical Morison equation is not able to compute rotational moments. Rotational moments (in case of short waves) are very important to simulate the dynamic behaviour of the SFT. Especially the roll motion is triggered by rotational wave forces. Neglecting these wave forces would result in large errors for roll motion predictions.

- The applicability for the classical Morison equation is for a wave length structure length ratio of around $L/D > 5$. For shorter waves, diffraction effects should be taken into account. With modified Morison, pressures, velocities and accelerations are averaged over the structure dimensions which results in a reduction of the the wave forces, in case of short waves, compared to the classical Morison theory which uses the velocity and acceleration at the centre of the structure. It should be noted that 'real' diffraction effects are **not** taken into account. The wave field is assumed to be unaffected by the presence of the structure.

A short description of the modification of each wave force components is given in separate paragraphs. An extensive overview of each force component and its mathematical expressions is elaborated in separate sections in appendix A.

Krylov force

In theory, the Krylov force is a force introduced by the unsteady pressure field generated by undisturbed waves. In the classical Morison equation, this force is described by the undisturbed acceleration at the centre of the submerged object. This causes that wave krylov moment can not be computed. In the wave force module, the undisturbed dynamic pressure is computed with the velocity potential theory. The undisturbed dynamic pressures are integrated over the wet surfaces of the tunnel which gives the Krylov forces on each face of the tunnel. By integrating the pressures over the wet surfaces, a resulting pressure moment, with respect to the centre of gravity of the tunnel, can be determined. The undisturbed pressure field can be seen in top right of figure 3.4. The Krylov force components are elaborated in appendix A.2.

Hydrodynamic force

The hydrodynamic force is dependent on the acceleration of water around the restrained SFT. The undisturbed water acceleration can be observed in the bottom left of figure 3.4. For short waves, the tunnel structure cannot be seen as a point object. The water acceleration is not determined at the centre of the structure but averaged over the structure dimensions. To compute the horizontal hydrodynamic force, a structure-height average water acceleration is computed. The averaged horizontal water acceleration is inserted in eq 3.2 to obtain the horizontal hydrodynamic force.

$$F_{hydrod,x} = \rho A_x C_{mx} \overline{\frac{\partial u_x}{\partial t}} \tag{3.2}$$

To compute the vertical hydrodynamic force, a structure-width average water acceleration is computed. The averaged vertical water acceleration is inserted in eq 3.3 to obtain the vertical hydrodynamic force.

$$F_{hydrod,z} = \rho A_z C_{mz} \overline{\frac{\partial u_z}{\partial t}} \tag{3.3}$$

The line of action of the horizontal hydrodynamic wave force and the line of action of the vertical hydrodynamic wave force have a moment arm with respect to the centre of gravity of the restrained SFT. The moment arm of the horizontal hydrodynamic force is indicated with $\overrightarrow{r_{hx}}$ and the moment arm of the vertical hydrodynamic force is indicated with $\overrightarrow{r_{hz}}$. The hydrodynamic wave moment can be computed with eq 3.4.

$$M_{hydrod,y} = F_{hydrod,x} \times \overrightarrow{r_{hx}} + F_{hydrod,z} \times \overrightarrow{r_{hz}} \tag{3.4}$$

For the horizontal hydrodynamic Morison coefficient a value of $C_{mx} = 1.35$ is used. For the vertical hydrodynamic Morison coefficient a value of $C_{mz} = 1.45$ is used. The calibration of the hydrodynamic Morison coefficients C_{mx} and C_{mz} can be found in appendix A.5. A detailed elaboration of the hydrodynamic force components can be found in appendix A.3.

Drag force

The drag force is dependent on the squared velocity of water around the restrained SFT. The undisturbed water velocity can be observed in the bottom right of figure 3.4. For short waves, the tunnel structure cannot be seen as a point object. The water velocity is not determined at the centre of the structure but squared averaged over the structure dimensions. To compute the horizontal drag force, a structure-height squared average water velocity is computed. The squared averaged horizontal water velocity is inserted in eq 3.5 to obtain the horizontal drag force.

$$F_{drag,x} = \frac{1}{2}\rho b C_d \overline{u_x}|\overline{u_x}| \tag{3.5}$$

To compute the vertical drag force, a structure-width squared average water velocity is computed. The squared averaged vertical water velocity is inserted in eq 3.6 to obtain the vertical drag force.

$$F_{drag,z} = \frac{1}{2}\rho 2a C_d \overline{u_z}|\overline{u_z}| \tag{3.6}$$

The line of action of the horizontal drag wave force and the line of action of the vertical drag wave force have a moment arm with respect to the centre of gravity of the restrained SFT. The moment arm of the horizontal drag force is indicated with $\overrightarrow{r_{dx}}$ and the moment arm of the vertical drag force is indicated with $\overrightarrow{r_{dz}}$. The drag wave moment can be computed with eq 3.7.

$$M_{drag,y} = F_{drag,x} \times \overrightarrow{r_{dx}} + F_{drag,z} \times \overrightarrow{r_{dz}} \tag{3.7}$$

A drag force coefficient of $C_d = 2.0$ is used. A detailed elaboration of the drag force components can be found in appendix A.3.

3.6.2. Current forcing

The current forcing on the SFT creates an extra drag force in the same direction as the current. The inline drag force due to a uniform current is determined with Morison's equation and described by $F_{cur,x}$. A drag coefficient of $C_{dc} = 2.1$ is used. The current influences the wave velocity potential. This effect is taken into account by changing the force prediction inertia coefficients C_{mz} and C_{mx} which are used to determine the wave forces. KC dependent functions are used to estimate the value of the inertia coefficients. The current forcing is elaborated in appendix A.6.

3.7. Dynamic module

A free floating tunnel has three degrees of freedom which are, roll, sway and heave. This dynamic system assumes the tunnel is connected with two in-extensible tethers. Adding two rigid constrains to the free floating tunnel reduces the SFT to a SDOF. This SDOF describes a coupled roll $\phi(t)$ and sway $x(t)$ motion. The heave motion is not present because the metric centre of the SFT is not changing in height due to the geometric layout, which assumes in-extensible tethers, of the chosen dynamic system. A schematization of the dynamic system is presented in figure 3.5a. The tunnel motion can be described by θ_1 and θ_2 indicated in red in the figure 3.5a. θ_1 is the angular rotation of the tether and θ_2 is the angular rotation of the tunnel body. Because the SFT body is connected with two rigid constrains, θ_1 can be written as function of θ_2. A non-linear scaling parameter λ is introduced which makes $\theta_1 = \theta_2 \lambda$. The SFT motion can be written as function of one rotational motion θ_2 around a instantaneous rotation point in space. This rotation point is present at the intersection of the two tether axis and because the structure is moving, the location of this fictive rotation point changes in time which can be observed in figure 3.5b.

Because of the assumption of small vibrations, the instantaneous rotational point is fixed at the intersection of the tether axis at the moment when the dynamic system is at rest. The fixed rotation point is indicated with $R(t_0)$ in figure 3.5b. Because of the assumption of small vibrations, the non-linear scaling parameter λ becomes linear.

(a) Schematic of the dynamic system. The dashed red line is the path that the rotation point follows in time.

(b) Evaluation of the rotation point in time.
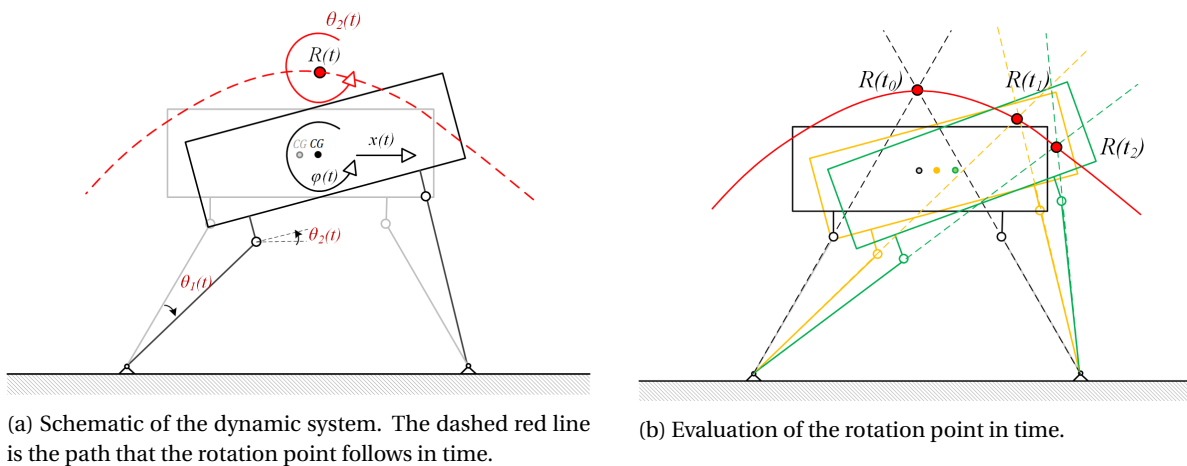
Figure 3.5: Schematization of Dynamic module.

Because the structure is submerged in still water, oscillations are damped. The total damping is composed of rotational damping and horizontal damping. In this manner, all combinations of combined roll and sway damping can be constructed. In case of a large tether angle, the sway motion is dominating. The rotational damping becomes negligible and horizontal damping remains. The other way around, in case of a small tether angle, the roll motion is dominating. The sway damping becomes negligible and rotational damping remains. In the situation that sway and roll are both present, a combined damping can be constructed. A visualization of decoupling of the total damping into a rotational damping and horizontal damping is presented in figure 3.6.
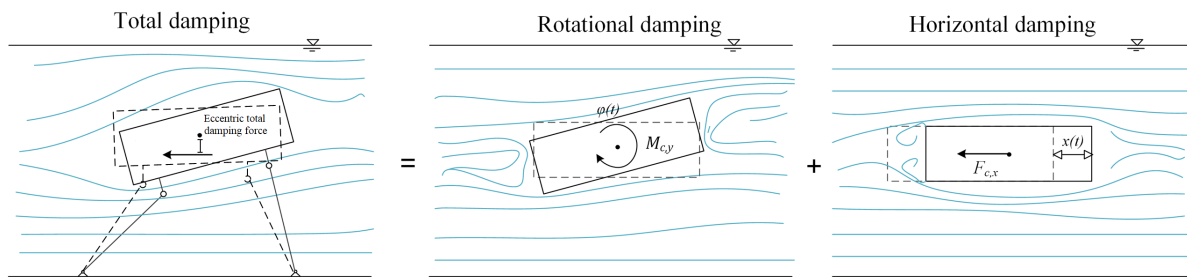
Figure 3.6: Decoupling of combined sway-roll damping into rotational damping and horizontal damping. Combined sway-roll damping is indicated with an eccentric damping force.

The rotational damping and horizontal damping are drag dependent and expressed as a rotational damping moment $M_{c,y}$ and a horizontal damping force $F_{c,x}$. The rotational damping moment is proportional to the roll of the tunnel body ($M_{c,y} \sim C_s \dot{\phi}(t)|\dot{\phi}(t)|$), the horizontal damping force is proportional to the sway of the tunnel body ($F_{c,x} \sim C_r \dot{x}(t)|\dot{x}(t)|$). The magnitude of the sway damping coefficient C_s and rotational damping coefficient C_r are calibrated with free decay tests from (Drost, 2019). The calibration method can be found in appendix B.4. In addition to these damping forces, there is also a buoyancy force F_b due to the displaced water. Due to this buoyancy force, tether forces are present. The tether located at the incident wave site is named the inner tether. The tether furthest from the wave source is named the outer tether. The inner tether force is indicated with T_{inner} and the outer tether force is indicated with T_{outer}. Both tether forces are dependent on the rotation θ_2 of the object. All forces are presented in figure 3.7a.

(a) Forces on SFT during oscillations in still water.

(b) Replacement of all forces by a damping moment and a stabilizing moment.
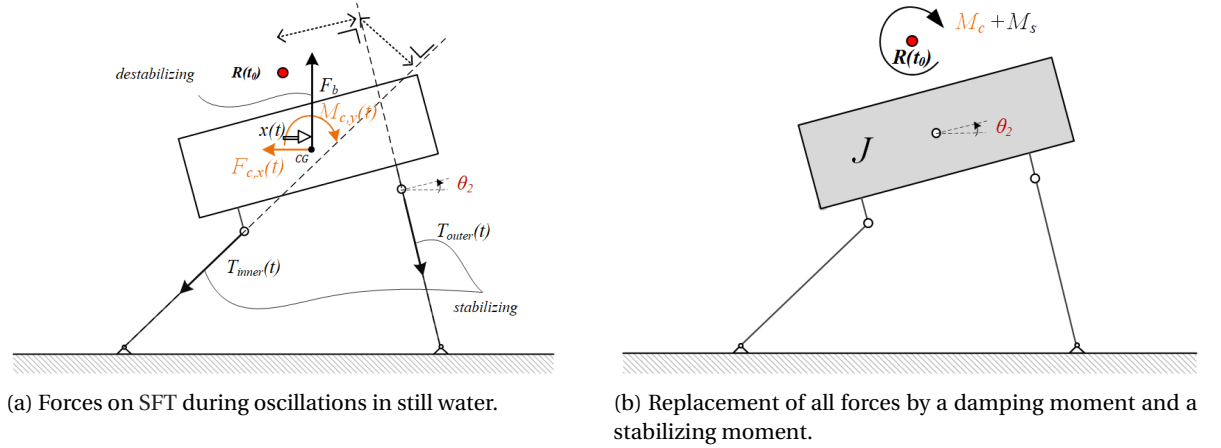
Figure 3.7: Schematic visualization of dynamic module. (De)stabilizing forces are indicated in black and damping forces are indicated in orange.

The forces that are presented in figure 3.7a can be replaced by one damping moment M_c and a stabilizing moment M_s at the location of the rotation point. The forces in the tethers cause a stabilizing moment with respect to the fixed rotation centre while the buoyancy force F_b causes a destabilizing moment with respect to the fixed rotation centre. The stabilizing moment due to the tether forces is more dominant than the destabilizing buoyancy moment. The resultant moment of the tether forces and the buoyancy force can thus be seen as a net stabilizing moment. The location of the rotation point is assumed fixed, chosen at the intersection of the tethers when the structure is at rest, taking advantage of the assumption of small vibrations. The damping moment and stabilizing moment around the fixed rotation point are visualized in figure 3.7b. The stabilizing moment is due to the presence of the tether forces and the buoyancy force. If the system is excited from its equilibrium, the stabilizing moment pushes the structure back to its equilibrium position. The motion is damped by the damping moment.

Besides the damping and stabilizing moment, the SFT motion has a moment of inertia J with respect to the fixed rotation point. The moment of inertia is obtained by applying the Lagrangian formalism in which the total potential and kinetic energy is expressed as function of the rotational motion θ_2. Mathematical derivation for the moment of inertia can be found in appendix B.2. The moment of inertia is dependent on the mass of the SFT. Because the water around the SFT body is accelerating with the body itself, an added mass term m' is introduced. This added mass term is added to the original mass of the SFT which increases the inertia of the structure. The moment of inertia J is presented in eq 3.8. The magnitude of this added mass term is tuned on the free decay tests from (Drost, 2019). The determination of m' can be found in appendix B.4.

$$J = \left(m + m'\right) \times \left(\frac{4a^2 + b^2}{3} - 2s_0 \lambda a - h_2 \lambda b + s_0^2 \lambda^2 + h_2^2 \lambda^2 + 2\gamma \lambda\, s_0 - \gamma^2 - 2a\gamma - 2\epsilon h_2 \lambda + b\epsilon + \epsilon^2 \right) \qquad (3.8)$$

The compact form of the equation of motion which describes the rotation of the SFT around the fixed rotation point, without the presence of external forcing, is presented in eq 3.9. Please note that the forcing term is taken equal to 0 because no external forcing is present during free decay.

$$\frac{d^2\theta_2}{dt^2}J + M_c + M_s = 0 \tag{3.9}$$

in which

J	=	Moment of inertia
M_c	=	Damping moment
M_s	=	Stabilizing moment independent of external forcing

The determination of the damping moment M_c can be found in appendix B.4 eq B.27 and expressions for the stabilizing moment independent of external forcing M_s can be found in appendix B.3 eq B.23.

3.8. Coupling module

In the coupling module, the wave force module and the dynamic module are coupled which is visualized in figure 3.1. The horizontal wave force $F_{w,x}$ horizontal current force $F_{cur,x}$, vertical wave force $F_{w,z}$ and rotation wave moment $M_{w,y}$, obtained from the wave force module, are attached to the gravitational centre of the SFT. This can be observed in figure 3.8a, in which the wave forces are indicated in blue. The tether forces are now not only dependent on the buoyancy force, but also on attached wave forces. Therefore, the inner and outer tether force vectors are partially black, partially blue. In orange, the damping forces can be observed. As said before, all forces from the wave force module and the dynamic module are attached to the metric centre of the tunnel structure. Attached implies that in case the structure moves, the forces move with the structure.

(a) Forces on moving SFT in waves + current

(b) Replacement of all forces by a wave force moment, damping moment and a stabilizing moment.
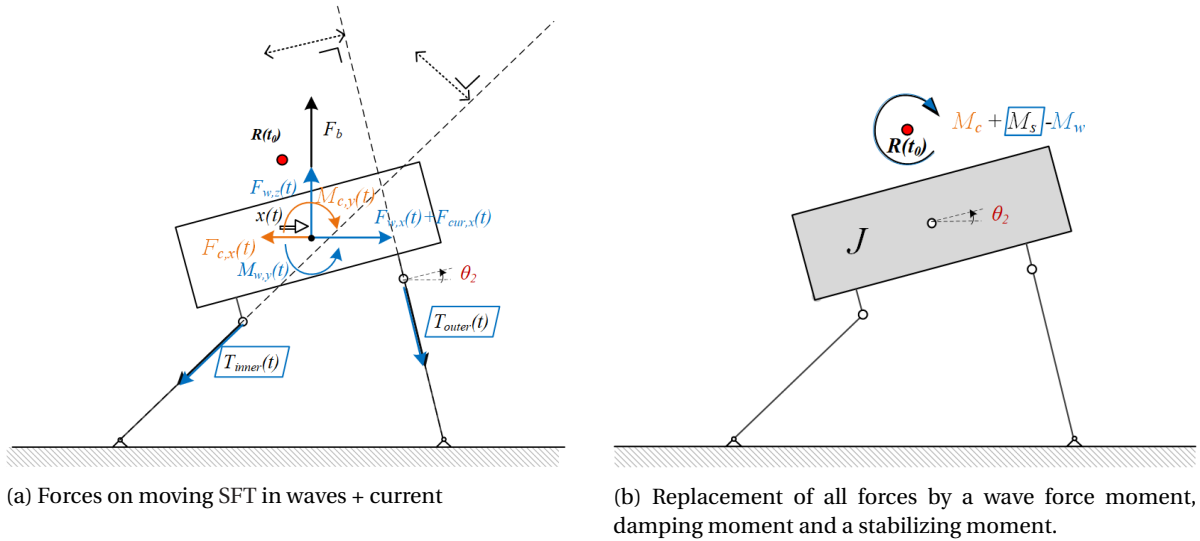
Figure 3.8: Schematic visualization of coupling module. Forces from the wave force module are indicated in blue. Forces form the dynamic module are indicated in black. In case a force is dependent on the wave force module and the dynamic module, both black and blue are used. Damping forces are indicated in orange.

All forces from figure 3.8b can be replaced by one rotational moment around the rotation point. The location of this rotation point is fixed, chosen at the intersection of the tethers when the structure is at rest taking advantage of the assumption of small vibrations. This rotational moment consists of a wave moment M_w, damping moment M_c and stabilizing moment M_s. M_w is written in blue because it depends on the wave force module only. M_c is written in orange. M_s is written in black and outlined with blue because this moment is due to the tether forces which are dependent on both modules.

The compact form of the full equation of motion which describes the rotation of the SFT around the fixed rotation point, forced by waves and current, is presented in eq 3.10.

$$\frac{d^2\theta_2}{dt^2}J + M_c + M_s = M_w \tag{3.10}$$

in which

J	=	Structural inertia
M_c	=	Damping moment
M_s	=	Stabilizing moment dependent of external forcing
M_w	=	Wave moment

The determination of the damping moment M_c can be found in appendix B.4 eq B.27. The expressions for the stabilizing moment independent of external forcing M_s can be found in appendix B.3 eq C.5. The determination of the wave force moment M_s can be found in appendix C.2 eq C.7.

From the full equation of motion presented in eq 3.10, the roll and sway of the tunnel can be determined, presented in eq 3.11 and 3.12. A full elaboration of the coupling module is provided in appendix C.

$$\phi(t) = \theta_2(t) \tag{3.11}$$

$$x(t) = h_2\lambda\theta_2(t) - \left(\frac{1}{2}b + \epsilon\right)\theta_2(t) \tag{3.12}$$

3.8.1. Simulation module MATLAB

The dynamic SFT model is modeled with MATLAB. In this way, many SFT configurations with different wave conditions can be simulated. To give an impression of the simulation module in MATLAB, snapshots of two SFT simulations are presented in figure 3.9.
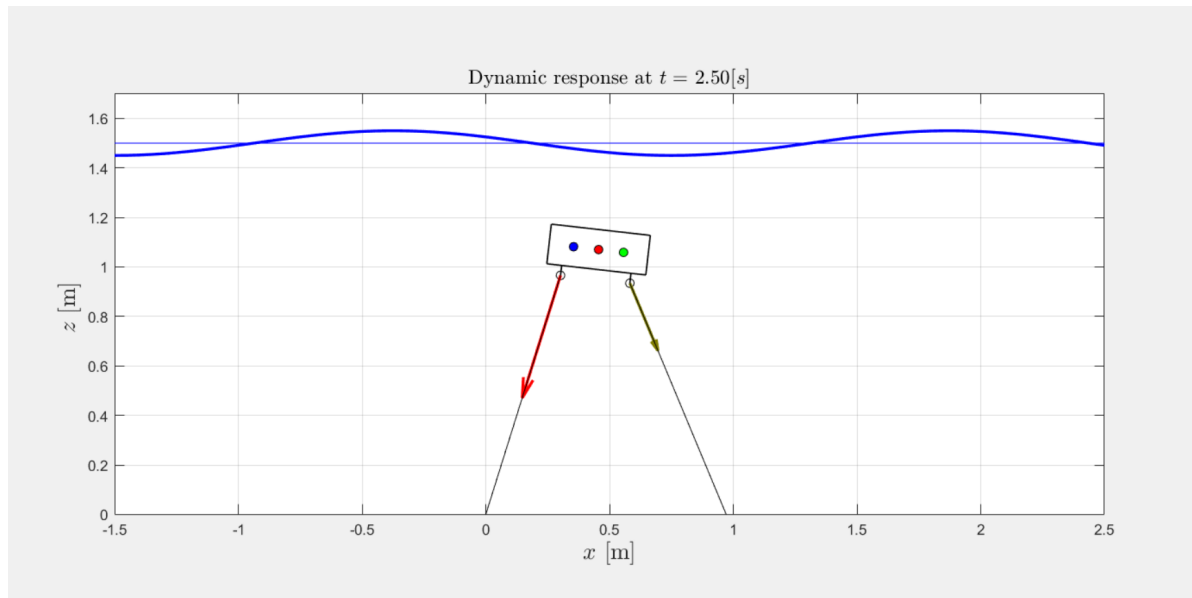
(a) Dynamic response simulation for a relative steep tether angle (70°) attacked by short waves. The tethers are connected inward of the tunnel body.
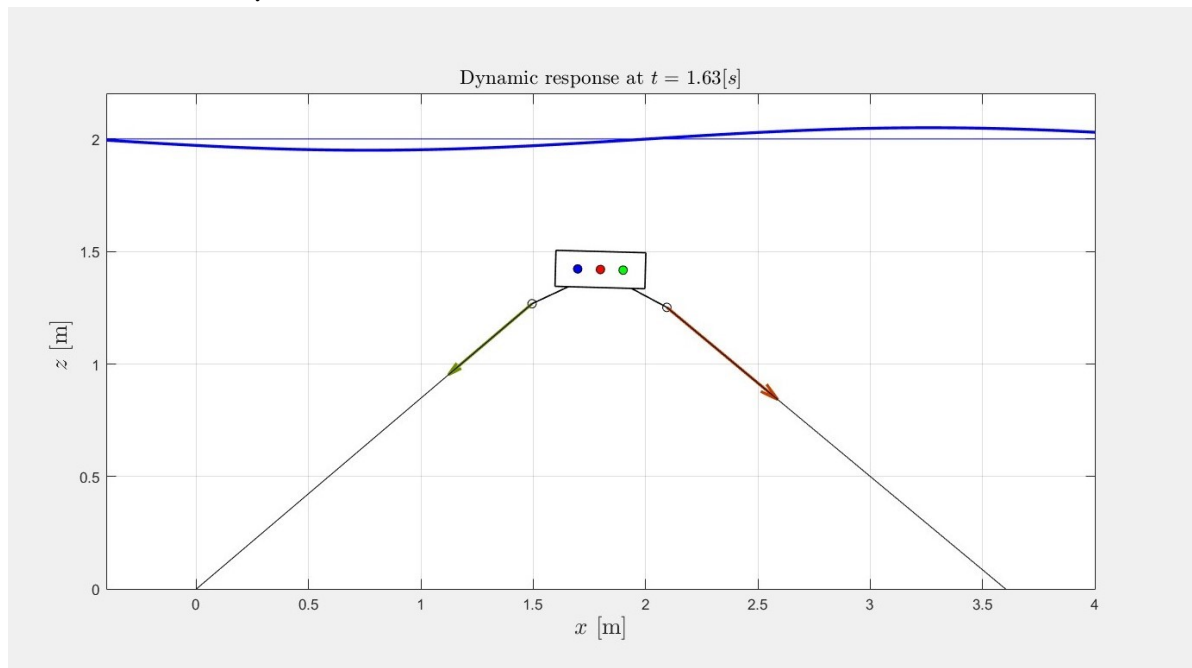
(b) Dynamic response simulation for a relative large tether angle (40°) attacked by long waves. The tethers are connected outward of the tunnel body.

Figure 3.9: Snap shots for two different SFT simulations. The simulations are performed with a MATLAB module. Vectors in the tethers show the magnitude of the tether force. Apart from the length of the vectors, the color is also indicating the magnitude of the tether force. The more red a tether vector is, the larger the force. The more green a tether vector is, the smaller the force. Please note, both configurations have a different water depth, tether connection, tether angle and submergence depth. Also the wave conditions are different for both simulations.

4

Validation

In this chapter, the dynamic submerged floating tunnel (SFT) model is validated. The validation is performed for each module separately. In other words, the wave force module, dynamic module and coupling module are validated in separate sections. The validation is performed with measured data from physical model experiments performed by (Drost, 2019). The physical model experiments are described in appendix D.

4.1. Wave Force module

The first module to be validated is the wave force module. First the wave force module is analysed and validated in time. The second part contains an analyses and validation of the maximal wave force in the wave number domain.

4.1.1. Analysis of wave forces in time

An analysis of the wave forces in time is done to check if the outcomes of the module is logical and expected. The SFT tunnel is attacked by a harmonic wave train with the following properties: $T = 1.0s, H = 0.16m$. The horizontal, vertical and rotational wave forces are plotted in time in figure 4.1. To analyse the force signal, two characteristic moments in time are analyzed. The first moment in time is at $t = 1.13s$ when the total horizontal and rotational moment are maximal and the vertical force is zero. The second moment is at $t = 0.88s$ when the total horizontal force and rotational moment are zero and the vertical force is maximal. Both moments in time are elaborated in separate sections.

t = 1.13s

In figure 4.1 it can be seen that the total horizontal force and rotational moment are maximal and that the vertical wave force is zero. At this moment of time, the dynamic pressures, water accelerations and water velocities are plotted and can be found in figure 4.2. The pressure at section I is larger than the pressure at section II. Because the node of the wave is located in the middle of the submerged body, this pressure difference is maximal. This implies that also the accelerations is maximal and directed in the same direction as the pressure resultant. The resultant vertical pressure force is zero and thus the averaged acceleration is also zero. The average velocity of water particles is directed in the upward direction and creates a vertical drag force. Because the drag force is small with respect to the Krylov force and hydrodynamic force, the horizontal force will be maximal and the vertical force tends to approximate zero. The rotational moment due to the Krylov force and the hydrodynamic force is maximal because the wave is located asymmetric on top of the submerged body. The rotational moment due to drag is zero at this moment of time, which gives a maximal total rotational moment.

t = 0.88s

In figure 4.1 it can be seen that the total horizontal force and rotational moment are zero and that the vertical wave force is maximum. At this moment of time, the dynamic pressures, water accelerations and water velocities are plotted and can be found in figure 4.3. The pressure at section I is the same as the pressure at section II because the trough of the wave is located in the middle of the submerged body, this pressure difference is

zero. This implies that also the horizontal accelerations is zero. The resultant vertical pressure force is maximal and thus the Krylov force and hydrodynamic force are maximal. The average velocity of water particles is directed in the horizontal direction and creates a horizontal drag force. Because the horizontal drag force is small, the total horizontal force approximates zero. The rotational moment due to the Krylov force and the hydrodynamic force is zero because the wave is located symmetric on top of the submerged body. The rotational moment due to drag is maximal because the flow around the submerged body is asymmetric. Because the drag is small, the total rotational moment is approximately zero.
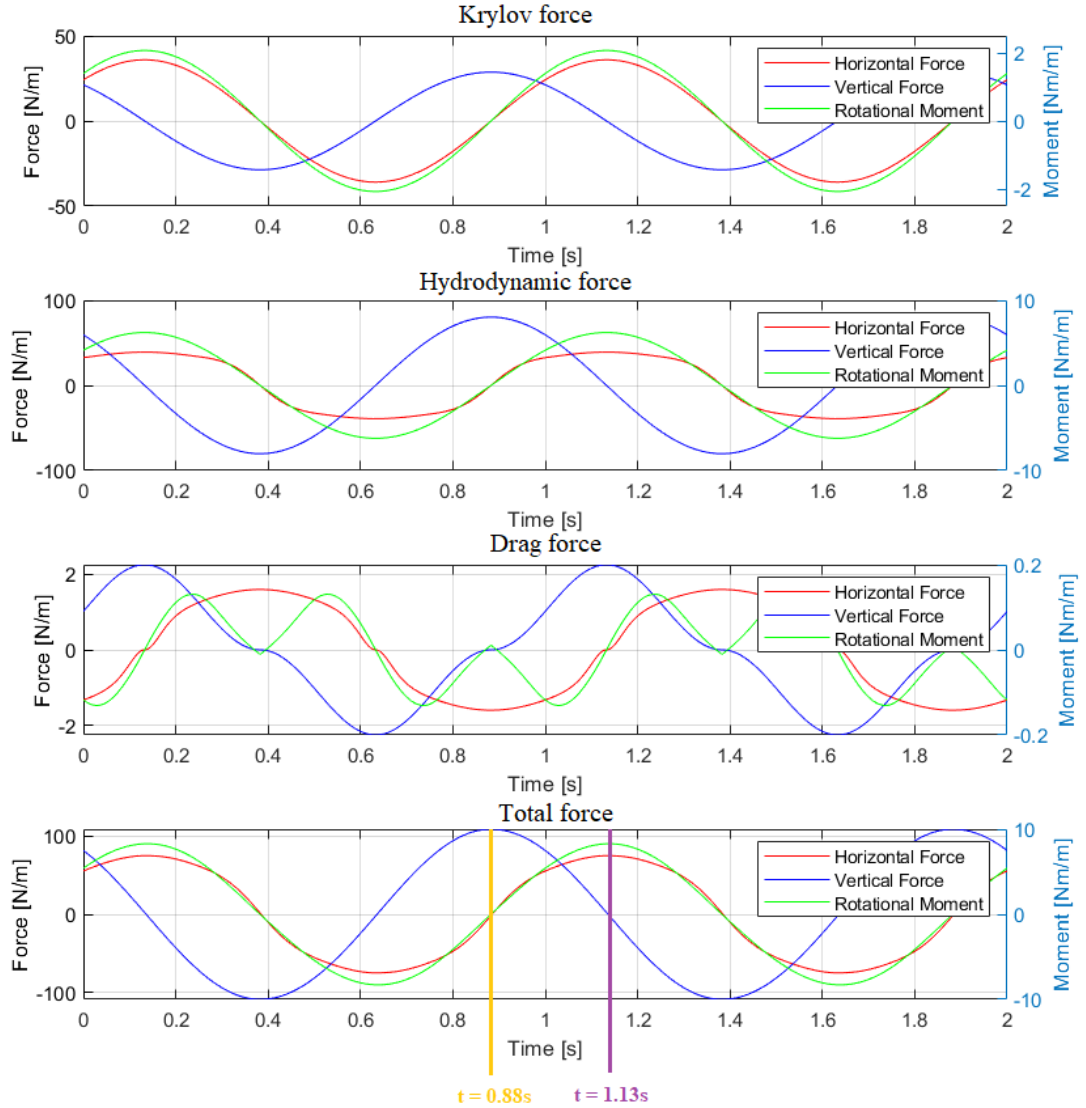
Figure 4.1: Total wave force on fixed SFT, composed out of Krylov force, hydrodynamic and drag force. Simulation time $t = 2T$, $s_1 = 0.35m$
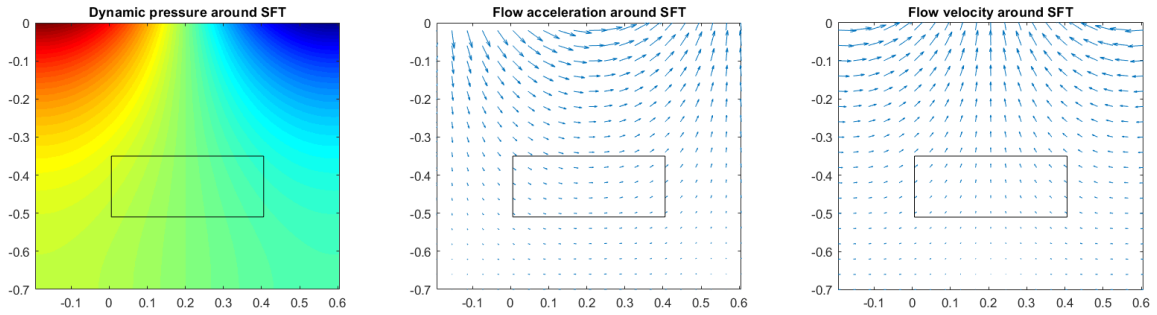
Figure 4.2: Undisturbed dynamic pressure, red largest absolute pressure, blue smallest absolute pressure. $T = 1.0s, H = 0.16m, s_1 = 0.35m$. Snapshot at $t = 1, 13s$.
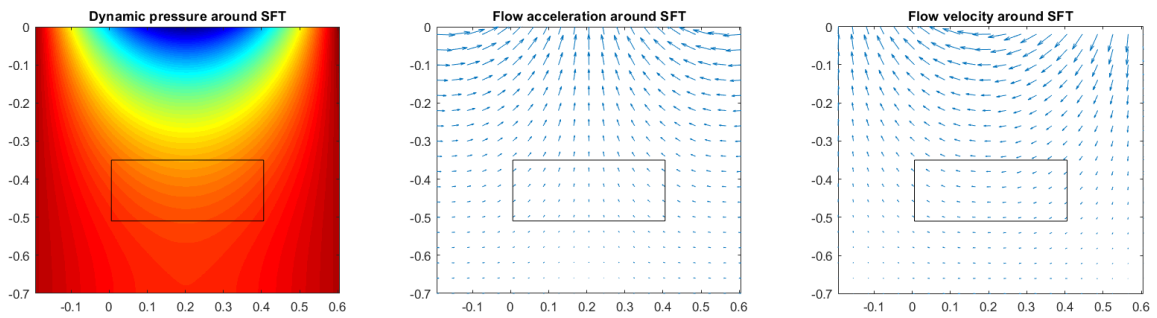
Figure 4.3: Undisturbed dynamic pressure, red largest absolute pressure, blue smallest absolute pressure. $T = 1.0s, H = 0.16m, s_1 = 0.35m$. Snapshot at $t = 0.88s$.

4.1.2. Validation of wave forces in time

Two different cases are validated, a long wave ($T = 1.41s$) on a relative deep submerged depth ($s_1 = 0.35m$) and a short wave ($T = 0.92s$) on a relative shallow submerged depth ($s_1 = 0.175m$). Figure 4.4 shows the forces on a deep submerged restrained submerged SFT in time due to a long wave. It can be observed that the model predicts the wave force almost perfect. The vertical wave force is over predicted a bit. The horizontal wave force and vertical wave force are 90 degrees out of phase which is due to the orbital motion described by the linear wave theory. The contribution of the vertical wave force to the rotational moment is small and therefore the rotational moment is in phase with the horizontal wave force.
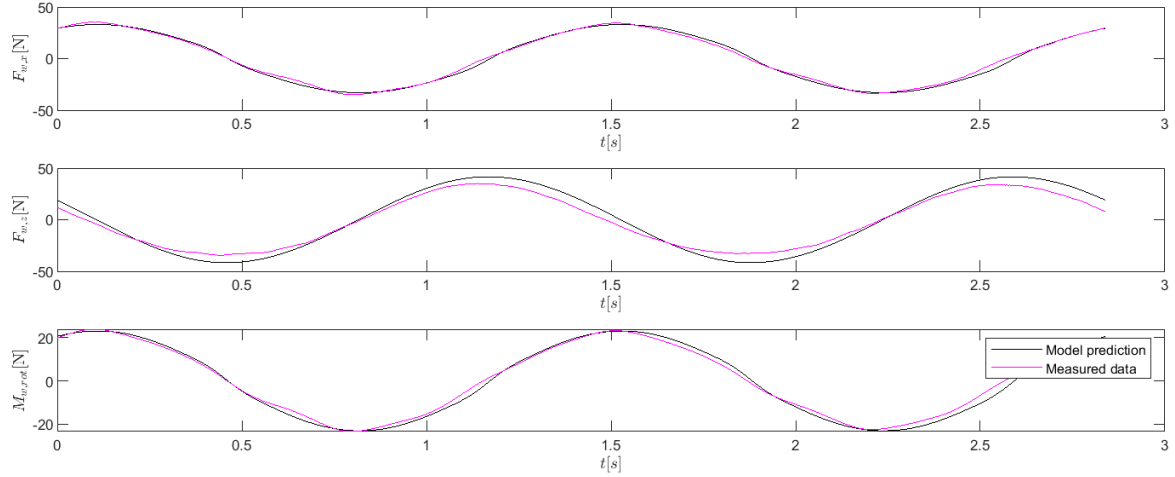
Figure 4.4: Wave forces on restrained SFT at submergence depth $s_1 = 0.35m$. $H = 0.08m, T = 1.41s$. Validation data from (Drost, 2019).

Figure 4.5 shows the wave force due to a short wave, attacking a shallow submerged restrained SFT. It can be observed that the force response becomes less sinusoidal. The crest and trough of the wave force response become longer. The model predicts this shape well, however the accuracy of the amplitude decreases. Decreasing the wave length and submergence depth results in more wave deformation which results in energy dissipation (breaking waves) and non linear fluid structure interaction. Because the wave field is not affected by the presence of the tunnel structure, the model can not take into account wave deformation and energy dissipation, which results in an over predicting the wave forces.
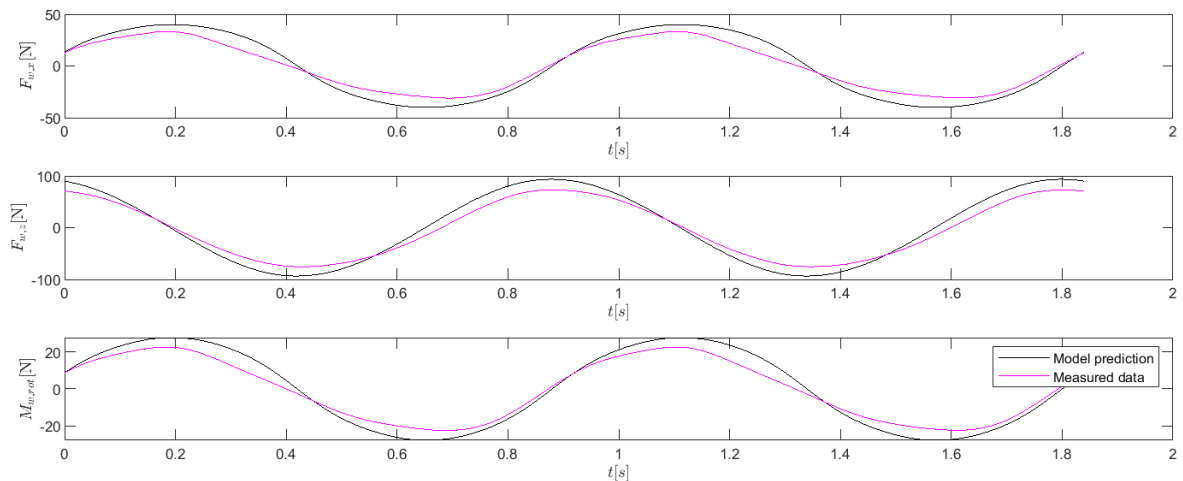
Figure 4.5: Wave forces on restrained SFT at submergence depth $s_1 = 0.175m$. $H = 0.08m, T = 0.92s$. Validation data from (Drost, 2019).

4.1.3. Analysis on wave force composition for various wave lengths

In this subsection, an analysis is performed on the different wave force components. These amplitude of these components, the Krylov force, hydrodynamic force and drag forces, are plotted as function of the non dimensional wave number kh_1 and presented in figure 4.6.
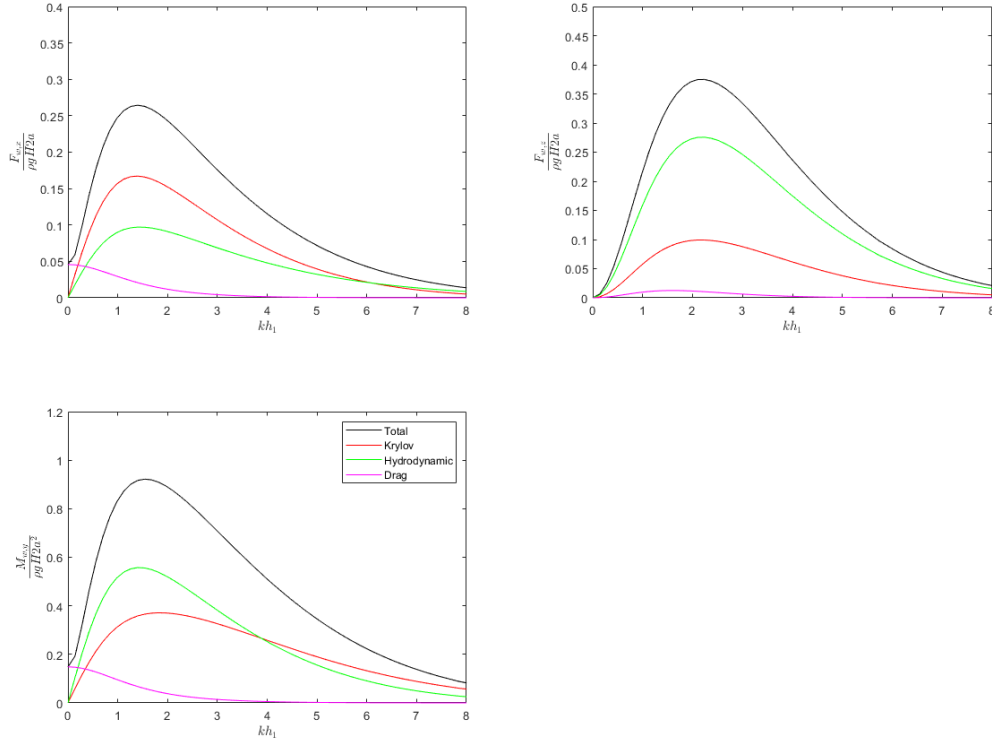
Figure 4.6: Composition of horizontal wave force, vertical wave force and rotational wave force. $s_1 = 0.35m$.

To study the ratio between these components, the Keulegan-Carpenter number is used. The KC number is defined in eq 4.1. In here u_m is the maximum flow velocity and T the period of the oscillatory flow.

$$KC = \frac{u_m T}{D} \tag{4.1}$$

The numerator of eq 4.1 shows the length scale of the orbital motion and the denominator the width D of the submerged object. For small KC numbers it can be said that the orbital motion of the water particles around the submerged object is small with respect to the dimension of the object itself. This means that for small KC numbers no separation of flow behind the object will occur. In this case the drag will become negligible and inertia dominates the system. In figure 4.6 this can be observed, the inertia is dominating for $kh_1 > 0.5$.

However when the orbital motion of water particles becomes large with respect to the object dimensions, drag becomes important. Flow separation and probably vortex shedding will be present. For large KC numbers, the flow becomes a steady current for each half period of the orbital motion. For long waves in shallow water, the orbital motion has no vertical component which means no vertical drag force. The drag dominance can be seen in figure 4.6 for $kh_1 \approx 0$.

4.1.4. Validation of wave force amplitude for various wave lengths

In this section, the amplitude of the horizontal, vertical and rotational wave force is analysed in the wave number domain. The non dimensional wave forces are plotted as function of the dimensionless wave number $k^* h_1$ on two different submergence depths. The wave number is indicated with $k*$ because the wave number is not measured but computed from the measured wave period. This can be observed in figure 4.7.
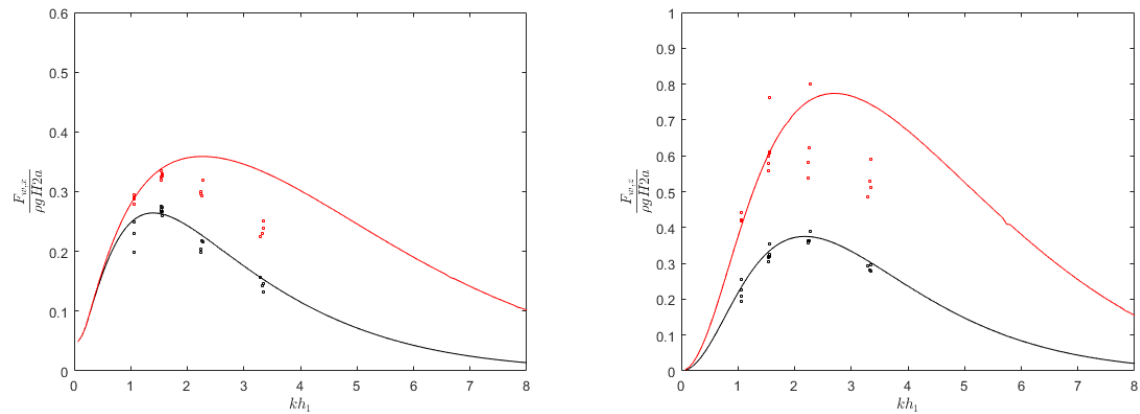
(a) Dimensionless horizontal wave force.

(b) Dimensionless vertical wave force.
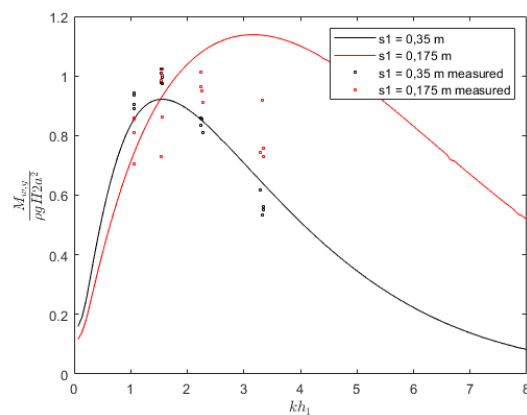
(c) Dimensionless rotational wave force.

Figure 4.7: Dimensionless wave forces on restrained SFT body as function of the dimensionless wave number on different submergence depths. Validation data from (Drost, 2019).

The model prediction for a submergence depth of $s_1 = 0.35m$ is almost perfect. On all wave length the prediction is good. For high wave numbers, the prediction becomes a bit weaker. The model prediction for a submergence depth of $s_1 = 0.175m$ is poor for the large wave numbers. For the longer waves the prediction is good. This can be declared based on the same argument as in the previous section. Short waves start to deform and even break on the shallow submerged structure. This deformation leads to a energy dissipation and other non-linear fluid structure phenomena that are not incorporated in the model. The waves are made non-dimensional by dividing, among other things, by the wave height. For the submergence depth of $s_1 = 0.35m$, it can be seen that the relation between wave height and wave force is linear. All measurements are on the same spot. For the small submerged depth, $s_1 = 0.175m$, the data is not on the same spot. The relation between the wave height and force response can not be described by a linear dependency.

4.1.5. Validation of horizontal wave force due to wave-current

In this section, the horizontal wave force is validated for a combined wave-current environment. The vertical wave force and rotational wave force are not validated because the current is a horizontal forcing. The horizontal wave force is also the largest contributor to the sway motion of the tunnel. Please note that the current has influence on the vertical forcing which is also included in the model. The validation is performed for one wave condition, with wave period $T = 1.82s$ and wave height $H = 0.08m$, on two submerged depths $s_1 = 0.35m$ and $s_1 = 0.35m$. The validations also includes a reference case in which the tunnel is loaded by current only. From figure 4.8, it can be concluded that for currents velocities up to $U_c = 0.4m/s$ the maximal deviation is below 20%. For $U_c = 0.4m/s$ at a submergence depth of $s_1 = 0.175m$ the deviation with the measured horizontal wave force is around 30%.
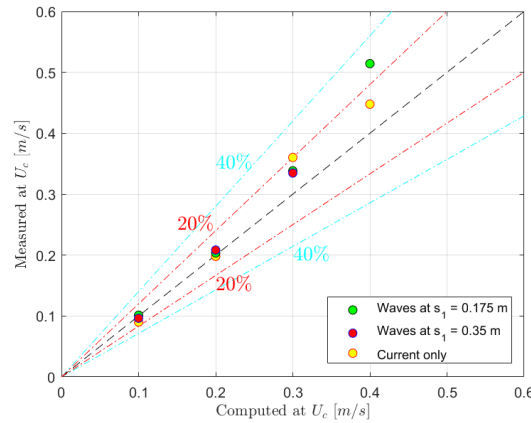
Figure 4.8: Horizontal wave force validation for a wave-current environment. For each current velocity, the wave force is computed with the model and the deviation with the measured wave force is computed.

4.2. Dynamic module

The dynamic module consist of a free oscillating SFT in still water, also called free decay. The free decay of two configurations is validated and verified. In figure 4.9a, the free decay of a SFT with a tether angle of $70°$ and submerged depth $s_1 = 0.35m$ is presented. The figure describes the rotation θ_2 around the rotation point $R(t)$. It can be seen that the natural period of the model and the measured data is the same until the amplitude of θ_2 becomes less than approximate $0.01[rad]$. This amplitude is reached after $4.5s$. After this time, the period of the measured data starts to decrease while the model period remains constant. This is due to the frequency independent added mass. For small amplitudes, the natural period is overestimated. The decay of the amplitude over time is estimated well until $4.5s$. After this time, the measured data decreases faster in time than the model predicted amplitude. The added damping is frequency dependent but in the model assumed to be constant. With small amplitudes, the model under predicts the damping.
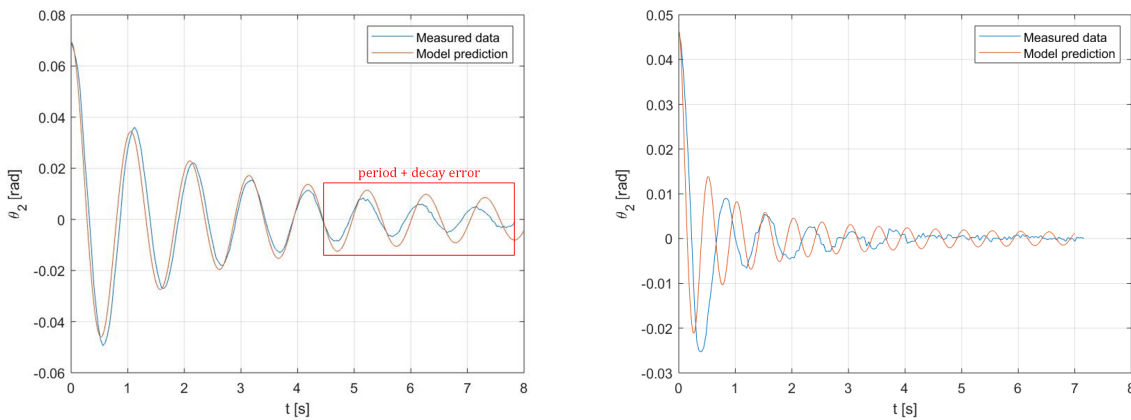
(a) Free decay test. Tether angle $= 70°$, $s_1 = 0.35m$.

(b) Free decay test. Tether angle $= 30°$, $s_1 = 0.175m$.

Figure 4.9: Free decay of model.

In figure 4.9b, the free decay of a SFT with a tether angle of $30°$ and submerged depth $s_1 = 0.175m$ is presented. It can be observed that the decay of the measured data and the model prediction are similar in magnitude. However the natural period of the measured data and the model are different which is due to the added mass. The added mass is tuned on a tether angle of $70°$ which allows combined sway and roll motion. The configuration with a tether angle of $30°$ has a pure roll motion which does not match with combined sway-roll added mass. This causes that the natural frequency of the $30°$ tether angle configuration is under predicted by the model.

4.3. Coupling module

In this section, the coupling module is validated and verified. The only tether angle that is considered is 70°. This angle gives large displacements while a tether angle of 30° is relative stable and gives very small displacements. For these small displacements the accuracy of the video analysis, which gives the deformation data, is not high enough for validation. First three different wave loading cases are analysed in time followed by an analysis of the displacements in the wave number domain.

4.3.1. Validation of displacement in time

The first case has a submerged depth $s_1 = 0.35m$ and is loaded by a linear wave train with $H = 0.08m$ and wave period of $T = 1.41s$. The sway displacement of the model and the measured data is presented in figure 4.10a. The model prediction fits the measured data well. The sway motion has the same form as the wave forcing and the positive sway displacement has the same magnitude as the negative sway displacement.

Decreasing the submergence depth changes the shape of the sway displacement response. This can be observed in 4.10b. The first thing that changes is the amplitude of the sway displacement, the positive sway is larger than the negative sway. This is predicted by the model. Also the time interval that the structure moves from negative sway to positive sway takes longer than the time interval that the structure moves from positive sway to negative sway. This phenomena is also captured by the model. However, there are some inequalities between the prediction and the measured data. The model does not take into account the deformation of the waves due to the presence of the structure. Diffraction and refraction effects can not be described by the model. Nevertheless, the prediction is fine.

In the last case, the wave period is decreased to $T = 0.92s$. The frequency of periodic forcing becomes so large that the structure in not capable to follow the wave motion. When the structure moves against the wave direction, the waves pass by so fast that the structure skips one wave. The structure has too much inertia to oscillate with same frequency as the waves. This can be seen in figure 4.10c. This phenomena is not captured by the model. The simplest explanation for that is the feedback effect of the structure on the wave field. If the object moves in the waves, it affects the wave field. With very large and fast motions, the wave field gets deformed allot. The dynamic SFT model does not take into account feedback effects. The wave field is not effected by the presents of the structure which makes it impossible to simulate similar effects. The amplitude of the oscillations is predicted with an error of approximate 30%. An possible explanation of the underestimation of the amplitude is given: because the structure is already positioned at the negative sway direction before the wave comes, the structure does not have to be 'stopped' by the coming wave. The object is moved from a stand still position instead of a negative approach speed. All energy that the wave gives to the SFT is used to accelerate the structure which results in larger displacements.
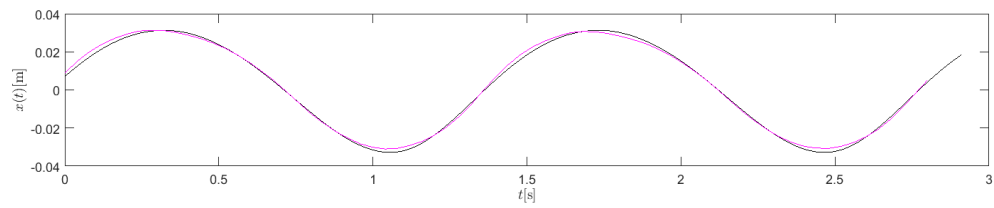
(a) Sway motion of SFT with submergence depth $s_1 = 0.35m$. $H = 0.08m$, $T = 1.41s$.
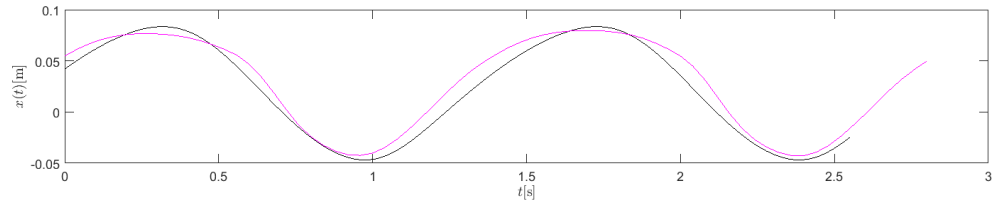
(b) Sway motion of SFT with submergence depth $s_1 = 0.175m$. $H = 0.12m$, $T = 1.41s$.
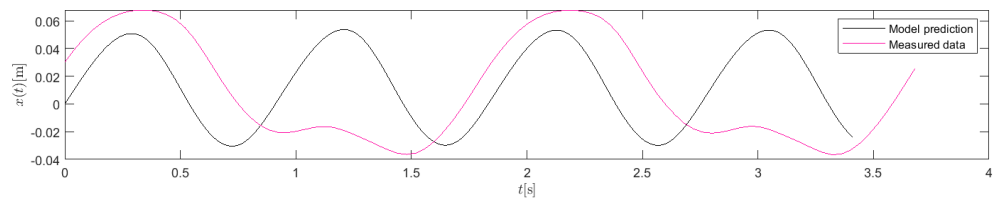
(c) Sway motion of SFT with submergence depth $s_1 = 0.175m$. $H = 0.12m$, $T = 0.92s$.

Figure 4.10: Wave forces on restrained SFT body on different submergence depths and wave periods.

4.3.2. Validation of displacements for various wave lengths

Now the displacements are validated and verified in time, all combinations of wave height and submergence depth can be plotted in the wave number domain to analyse the maximum positive and negative sway motion. The wave number is indicated with $k*$ because the wave number is not measured but computed from the measured wave period. It can be observed that the model predicts the measured data very well for the small waves ($H = 0.02m$ and $H = 0.08m$). Except for the large waves ($H = 0.12m$ and $H = 0.16m$), there is some scatter. With these large waves, in some cases, the SFT has snapping lines which influences the motion of the tunnel. The tunnel starts to bounce while oscillating. Because the model is not taking this bouncing effect into account, the prediction for the larger waves is sometimes poor. The dynamic model does also not take into account wave deformation and dissipation of energy due to the presence of the structure. This also results in a prediction error. The largest errors are found for the negative sway motion when the SFT is subjected to short waves.
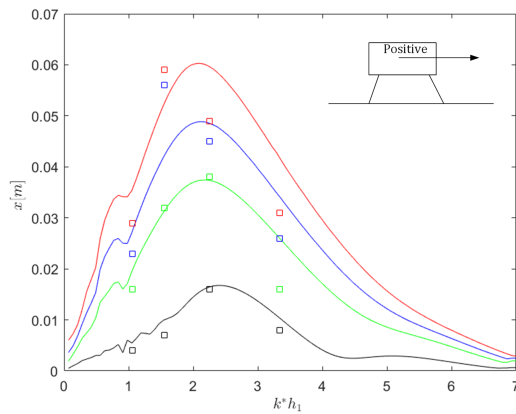
(a) Submergence depth $s_1 = 0.35m$.
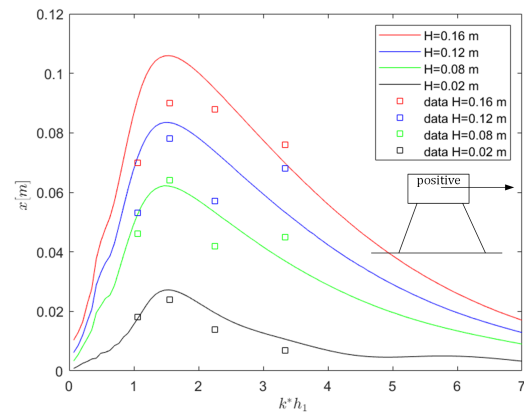
(b) Submergence depth $s_1 = 0.175m$.

Figure 4.11: Positive sway for tether angle 70°.
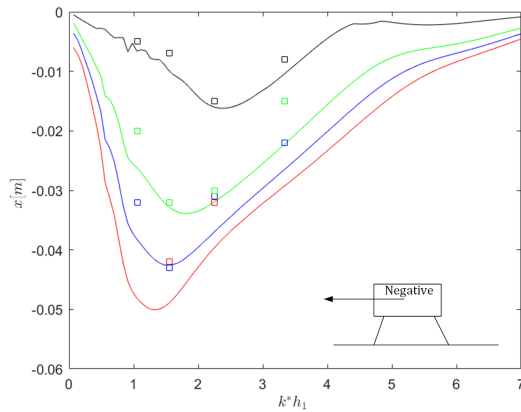
(a) Submergence depth $s_1 = 0.35m$.
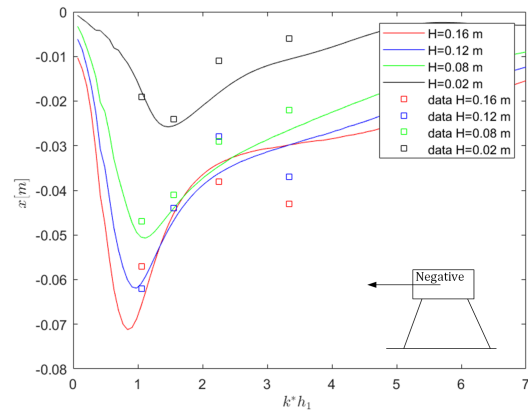
(b) Submergence depth $s_1 = 0.175m$.

Figure 4.12: Negative sway for tether angle 70°.

The wave length for which the structure has the largest positive sway displacement is almost independent of the wave height. In figure 4.11a and 4.11b this can be observed. The peaks for each wave height are located around the same wave number. However, the wave length for which the structure has the largest negative sway displacement does depend on the wave height. When the wave height increases, the negative sway motion is more sensitive to longer waves. This effect is due to the motion of the structure perpendicular to the wave motion. Observed from the structure, the waves length is shorter in than observed from a fixed location. If the negative velocity of the tunnel starts to increase, which happens for larger waves, the observed

wave length becomes shorter. The largest sway displacements are obtained at a constant wave length / wave structure ratio which is independent of the wave height. To obtain a constant wave length / wave structure ratio, the wave length needs to be increased to obtain a maximal displacement.

4.3.3. Validation of displacements due to wave-current for various wave lengths

In this section, a validation on the sway displacement, caused by a wave-current environment, is performed. The validation is performed for a tunnel configuration with a submergence depth of $s_1 = 0.35m$ and a tether angle of 70° loaded by a current in combination with a constant wave height of $H = 0.08m$. The results can be found in figure 4.13. The shape of the prediction is computed well. An increase in current velocity results in smaller positive and negative sway displacements. The orbital motion and pressure field are affected in such a way that the Krylov force and hydrodynamic force become smaller. Still the displacement prediction is a bit off. It can be observed that the positive sway displacement prediction is weaker than the negative sway displacement. The wave current interaction is highly simplified in the wave force module. The wave current loading on the SFT is a large simplification and meant for a preliminary impression. Further research and also more sophisticated models should be used to model the effect of a wave-current environment on the dynamic behaviour of the SFT.
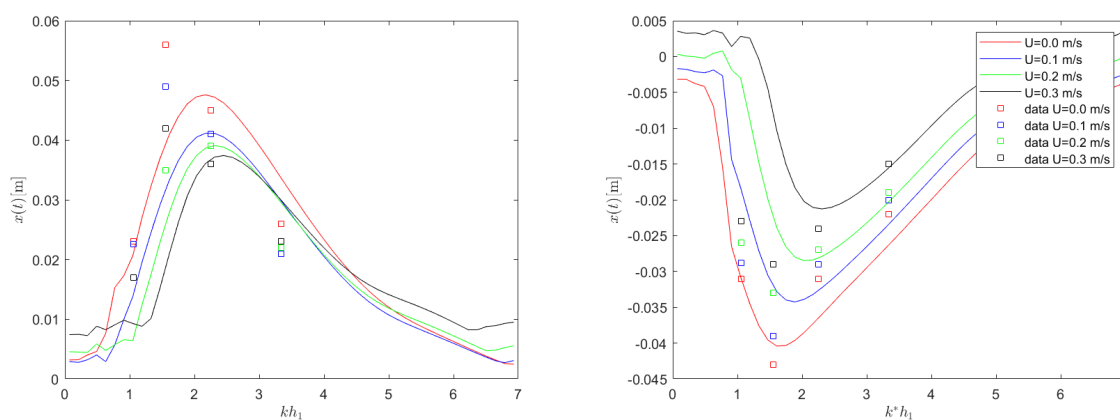
(a) Positive sway displacement.   (b) Negative sway displacement.

Figure 4.13: Negative sway for tether angle 70° and submergence depth $s_1 = 0.35m$. Forced by constant wave height $H = 0.08m$ in combination with current.

4.3.4. Validation of tether force in time

To validate the tether forces in time, four different configurations are analysed. These are presented in table 4.1. All cases are loaded by a linear wave train with $H = 0.08m$ and wave period of $T = 1.82s$.

Table 4.1: Validation configurations for tether forces.

Case	Submergence depth	Tether angle
1	$s_1 = 0.35m$	30°
2	$s_1 = 0.175m$	30°
3	$s_1 = 0.35m$	70°
4	$s_1 = 0.175m$	70°

The first case is presented in figure 4.14a. For a SFT with tether angle of 30° and submergence depth $s_1 = 0.35m$, forced by a long wave, the model prediction is good. The time shift between the inner and outer tether is correct. The second case is presented in figure 4.14b. The submerged depth is decreased which causes higher tether forces. The because the structure is more exposed to the waves, small second order effects in the force response can be observed. Because the dynamic model does not take into account refraction and diffraction effects, these second order effects can not be predicted by the model. The prediction if fine.

Now the tether angle is changed to 70° with a submergence depth $s_1 = 0.35m$, the results are presented in figure 4.14c. It can be observed that the model predicts the time shift between the inner and outer tether

correct. However the shape of the response that is measured and predicted are slightly different. The measured data shows larger second order effects while the model predicts only very small second order effect. The amplitude of the force prediction is good, however the exact shape of the tether force response is a bit off. In the fourth case, the submerged depth is decreased which causes more wave structure interaction. The second order effects are comparable with case 3. Again the model is not capable of predicting these second order effects. However the maximal tether force is predicted correct.
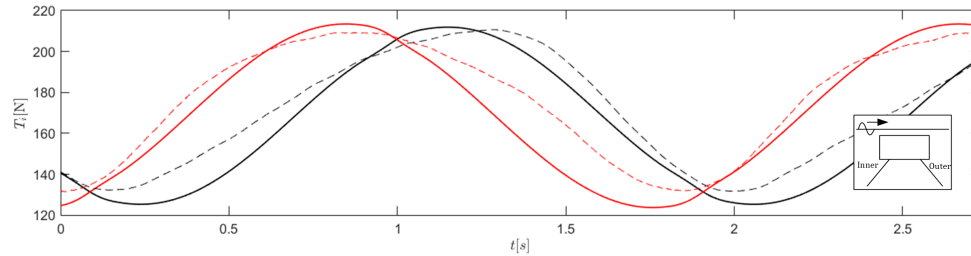
(a) Case 1: Tether forces of SFT, $s_1 = 0.35m$, tether angle = $30°$. $H = 0.08m$, $T = 1.82s$.
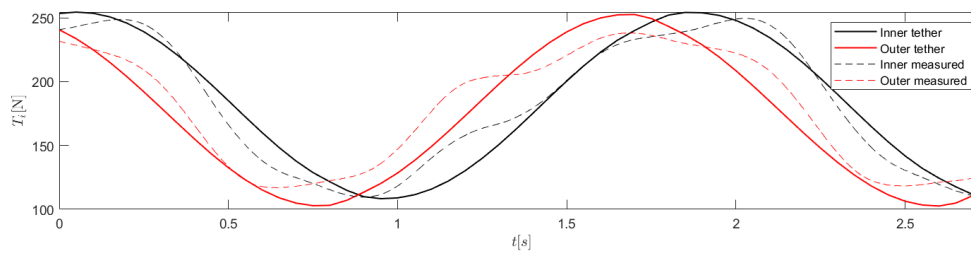
(b) Case 2: Tether forces of SFT, $s_1 = 0.175m$, tether angle = $30°$. $H = 0.08m$, $T = 1.82s$.
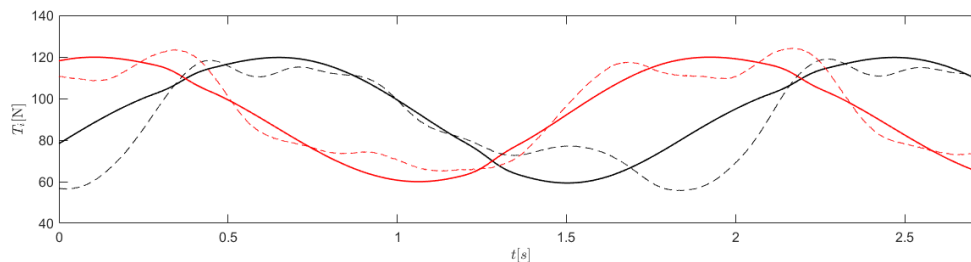
(c) Case 3: Tether forces of SFT, $s_1 = 0.35m$, tether angle = $70°$. $H = 0.08m$, $T = 1.82s$.
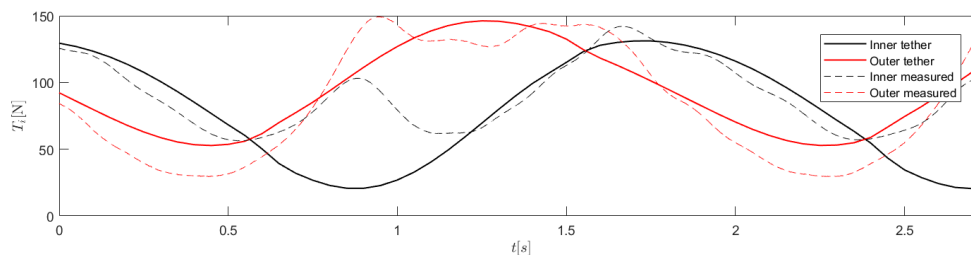
(d) Case 4: Tether forces of SFT, $s_1 = 0.175m$, tether angle = $70°$. $H = 0.08m$, $T = 1.82s$.

Figure 4.14: Tether forces on SFT for cases 1-4.

The second order effects of case three are further analysed by decreasing the wave period and increasing the wave height. In figure 4.15, two different load cases are analysed. The first one can be found in figure 4.15a in which the wave period is decreased to $T = 1.12s$. The wave height is kept the same ($H = 0.08m$). A decrease in wave period creates very large second order effects. The maximal tether force is increased by 200%. The model is completely wrong in its prediction. The behaviour looks similar to snap forces due to relaxation in the tethers, something that the model does not predict. However no snapping lines are present. The tether forces are always larger than zero. An explanation for this second order phenomena is given in section 4.3.5.

The second case considers the same configuration as the previous one, except now the wave height is

increased. The force response is presented in figure 4.15b. It can be observed that high peaks in the measured force response appear which the model does not predict. These high peaks are due to the snapping lines. No tension is present in the lines followed by a enormous snapping force. The model prediction is complete wrong. The error in the force prediction is due to the model assumptions. In the dynamic module, the tethers are assumed to be rigid bars which can take tension but also compression. Therefore no snapping lines be modelled which results in no extreme peak forces. It can be observed that the model is capable of predicting the snapping forces. The tether forces are at some point below zero which means compression in the tethers. In this way it is possible to predict if snapping lines will occur but it is not possible for the model to predict the forces in the tethers due to this snapping line event.
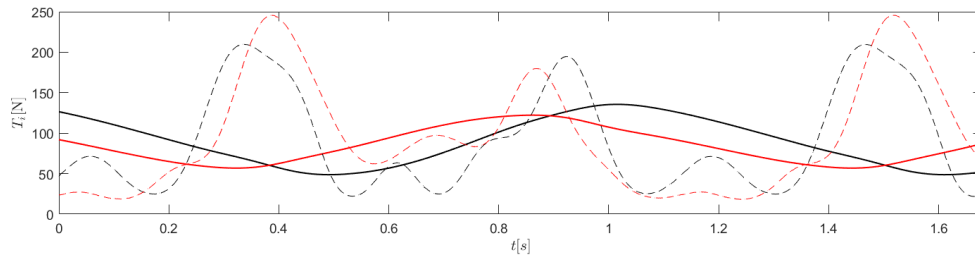
(a) Tether forces of SFT, $s_1 = 0.35m$, tether angle $= 70°$. $H = 0.08m$, $T = 1.12s$.
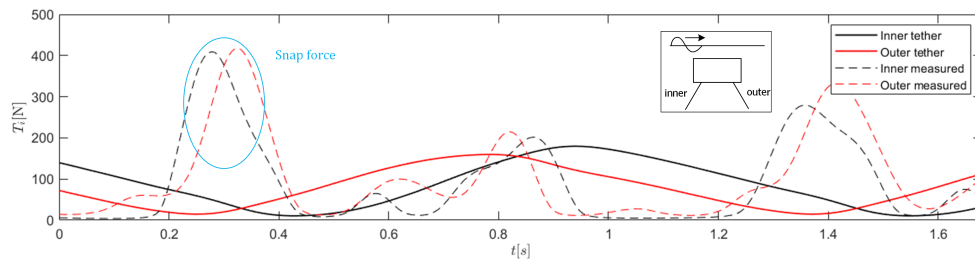
(b) Tether forces of SFT, $s_1 = 0.35m$, tether angle $= 70°$. $H = 0.16m$, $T = 1.12s$.

Figure 4.15: Tether forces on SFT for case 3. Change in wave height and wave period.

4.3.5. Validation of tether forces for various wave lengths

The last validation of the coupling module is performed on the tether forces in the wave number domain. The validation of the tether forces takes into account two different tether angles, a tether angle of 30° and a tether angle of 70°. The configurations with a tether angle of 30° can be found in figure 4.17 and the configuration with a tether angle of 70° can be found in figure 4.18. The wave number is indicated with $k*$ because the wave number is not measured but computed from the measured wave period.

First the 30° configuration is validated. The left column of figure 4.17 (figures a,c,e) show the tether forces and measured data with a submergence depth of $s_1 = 0.35m$. It can be observed that the model fits the measured data almost perfect. An decrease in submergence depth to $s_1 = 0.175m$ can be found in the right column of figure 4.17, (figures b,d,f). The amplitude of the tether forces is larger, the tunnel is located closer to the incident waves. In figure 4.17b, the tether force is over predicted for short waves. This is the result of the wave force module. In the wave force module, the incident wave does not takes into account wave deformation and dissipation of energy due to the presence of the SFT. The direct result of the over prediction of wave forces is an over prediction of tether forces. Nevertheless the prediction error is still acceptable. An increase in wave height results in higher tether forces which can be observed in figure 4.17d,f. The amplitude of the tether forces become so high that the minimum tether force becomes zero which results in a snapping line. Areas where snap is predicted are colored blue. In figure 4.17d, marked in green, the model over predicts the tether force. The model predicts a snapping line while in model tests, this is not the case. It can be seen that for all other measurements, the snap is predicted well.

The configurations with a tether angle of 70° is now validated and can be found in figure 4.18. Again the left column of the figure validates a submergence depth of $s_1 = 0.35m$ and the right column validates a submergence depth of $s_1 = 0.175m$. First a the submergence depth of $s_1 = 0.175m$ is discussed. It can be observed that the model predicts snapping lines for wave heights of $H = 0.12m$ and $H = 0.16m$. The area of this prediction is indicated with a blue box. It can be seen that the snap prediction is correct. Outside the blue box, the data fits the model well. Inside the box, large snapping forces are present. Because the model is not capable of computing the snapping forces, large prediction errors are made. However this is no problem because the model predicted that snap would occur.

For a submergence depth of $s_1 = 0.35m$, the force prediction is weaker. It can be observed in figure 4.18a,c,e that for a wave height of $H = 0.08m$, $H = 0.12m$ and $H = 0.16m$ the dynamic model has a large underproduction. This is also discussed in section 4.3.4. These plots are assigned with a red box. It can be seen that the minimal tether forces for a wave height of $H = 0.08m$ and $H = 0.12m$ is always above zero and so the reason for this under prediction is not a snapping line. The maximal error is almost 400 % which in unacceptable. The reason for this under prediction is due to the set-up of the physical model tests. In figure 4.16, the set-up for the physical model tests for a tether angle of 70° on a submergence depth of $s_1 = 0.35m$ and $s_1 = 0.175m$ is presented.
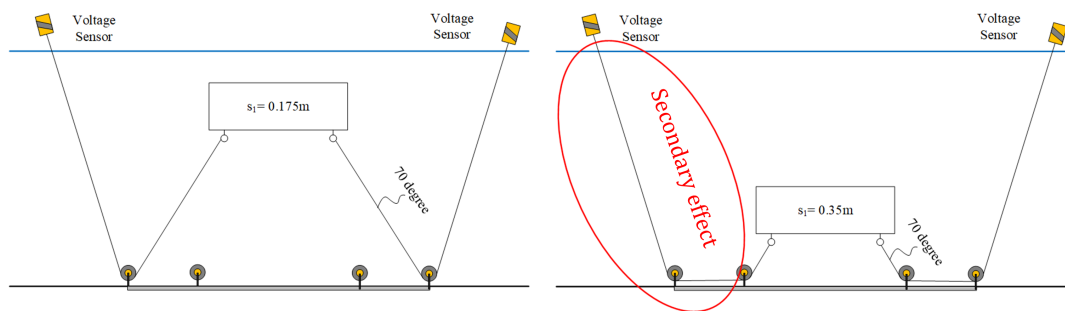
Figure 4.16: .

The tether forces are measured by force sensors above the still water surface. Via pulleys on the bottom, the tunnel tethers are redirected towards the force sensors. Two tethers can be identified at each side of the tunnel, from the force sensor towards the pulley and from the pulley towards the tunnel. If the ratio between these tethers becomes too large, secondary effects start to take place. The secondary effects in combination with stiff pulleys gives a different physical model than a tether connected to the bottom. If the submergence depth is shallow, no large secondary effects take place. In section 4.3.6, the validation for the submergence depth of $s_1 = 0.35m$ is performed again. The secondary effects are filtered from the time signal to obtain a corrected data set.
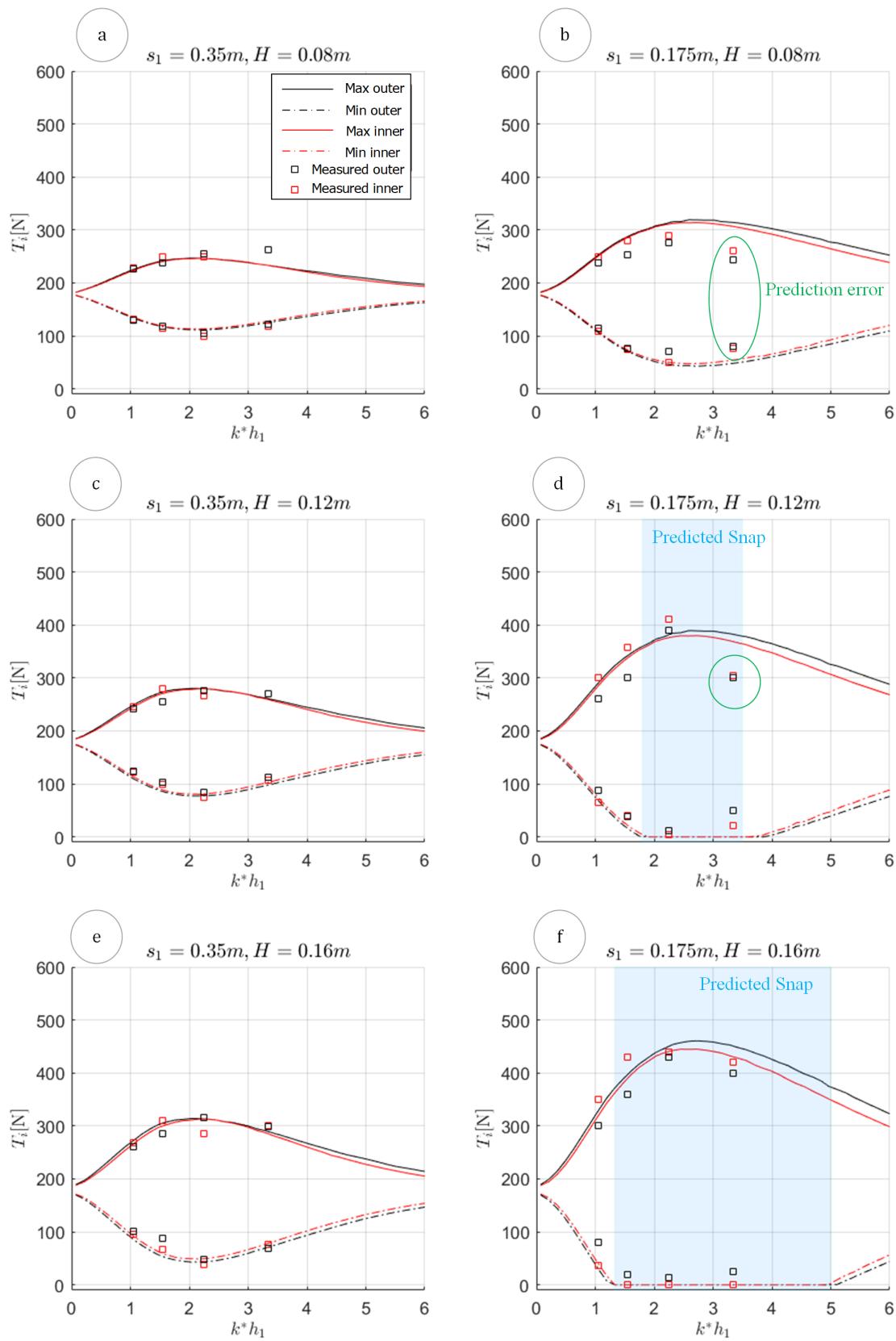
Figure 4.17: Tether force validation for configurations with tether angle $= 30°$. Left column shows a submergence depth $s_1 = 0.35m$. Right column shows a submergence depth $s_1 = 0.175m$.
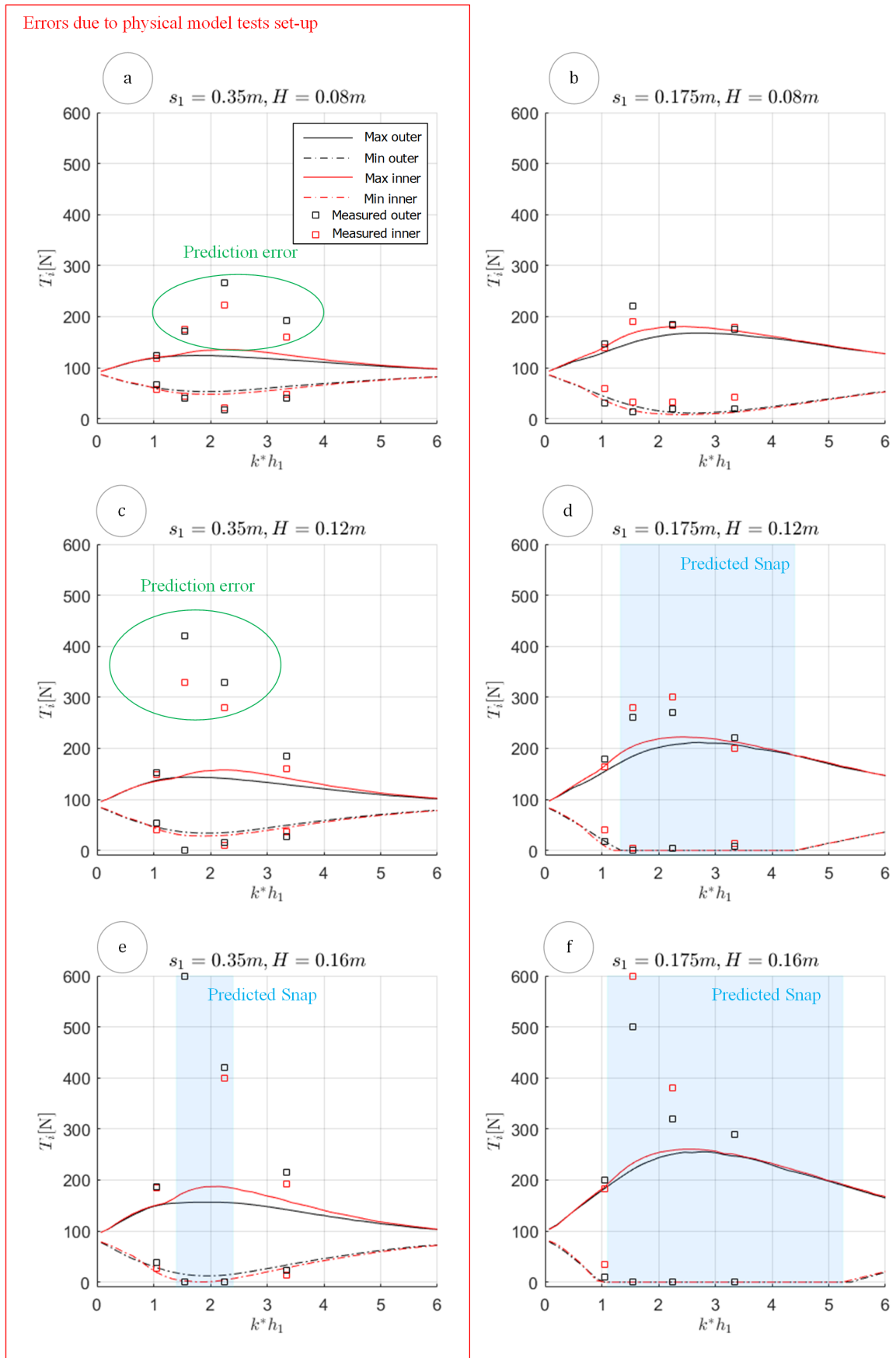
Figure 4.18: Tether force validation for configurations with tether angle = 70°. Left column shows a submergence depth $s_1 = 0.35m$. Right column shows a submergence depth $s_1 = 0.175m$.

4.3.6. Validation of tether forces (filtered data: $tether\,angle = 70°$, $s_1 = 0.35m$)

As discussed earlier in the previous section, the tether force data for a tether angle = 70° with a submergence depth of $s_1 = 0.35m$ contains large secondary effects. These are due to the chosen physical model set-up explained in figure 4.16. The data is filtered by extracting the wave frequency mode. This is illustrated in figure 4.19. The wave frequency mode is chosen because the motion of the tunnel is wave frequency dominant.
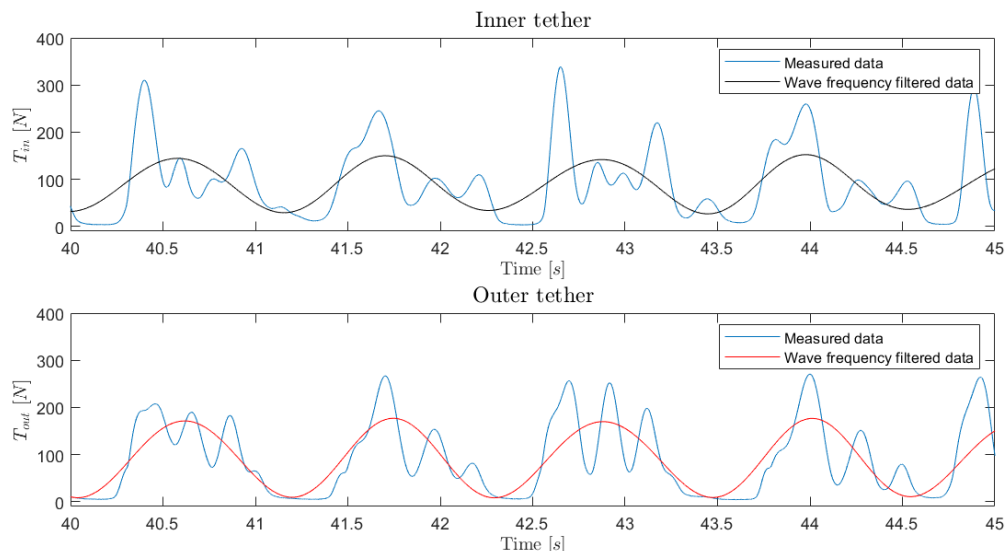
Figure 4.19: Filtered tether forces. Tether angle = 70°, $s_1 = 0.35m$, $H = 0.12m$, $T = 1.12s$.

It can be observed that the inner tether has higher order harmonics, due to the secondary effects, than the outer tether. The amplitude of the force signal is reduced for both tethers. The reduction is higher for the inner tether because of the higher second order harmonics. Likewise figure 4.18a,c,e, the minimal and maximal amplitude of the tether force are plotted in the wave number domain only now with the filtered data. For data which 'real' snapping forces are measured, no filtering is applied. For structures with snapping lines, almost no wave frequency mode is present in the force signal. Snap would be filtered away from the force signal which is not desirable. The filtering result is presented in figure 4.20. It can be observed that the data of the outer tether fits the model date well. The force prediction for the inner tether is weak. The measured tether force signal contains too much second order harmonics, due to secondary effects, to extract the wave frequency mode in a correct way. It seems that the model predicts the tether forces for this configuration well. Most likely, the error is due to a wrong physical model set-up and not due to the dynamic SFT model.
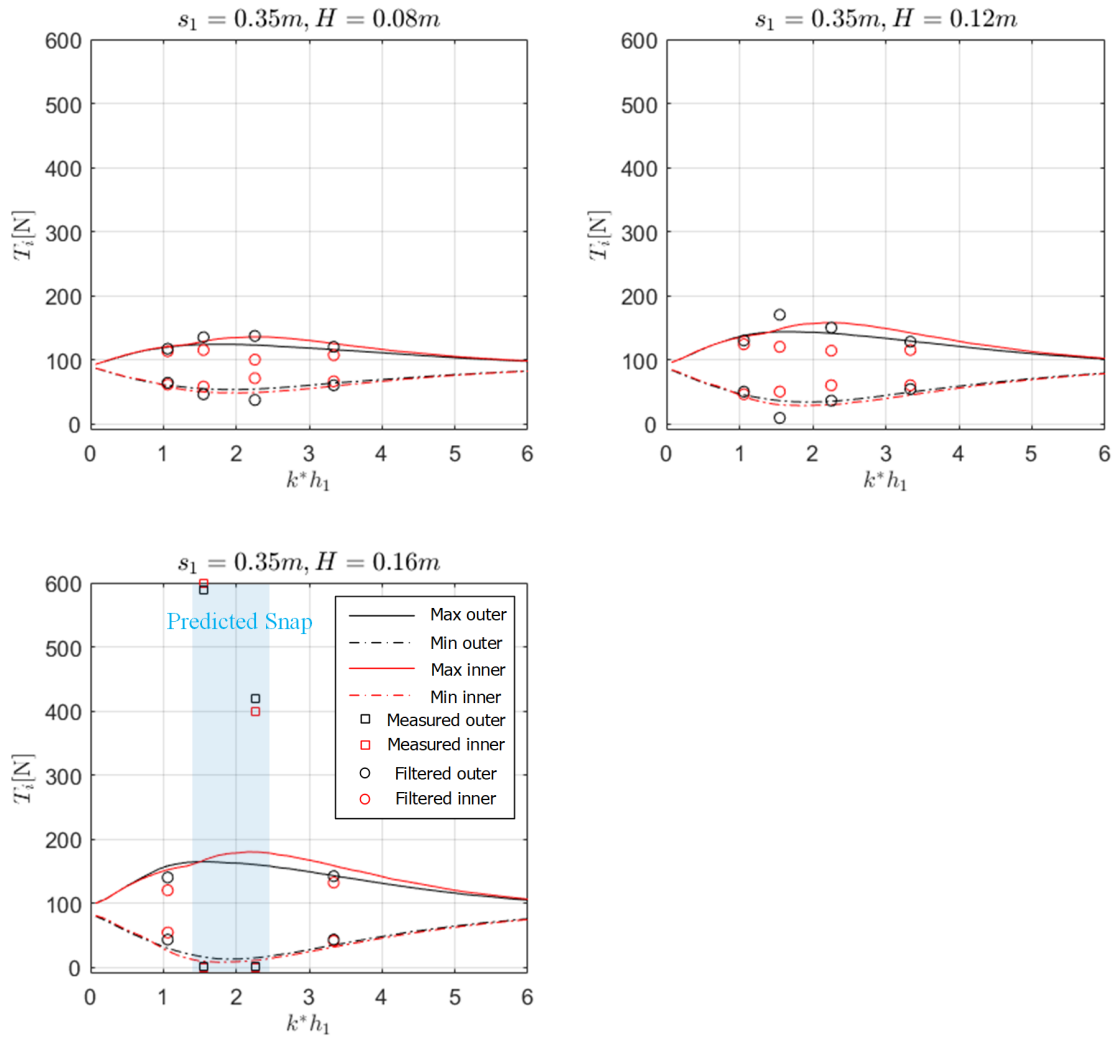
Figure 4.20: Tether force validation for configurations with tether angle = 70° and a submergence depth $s_1 = 0.35m$. Measured data is filtered by extracting the wave frequency mode.

4.4. Limitations of dynamic SFT model

After the validation of the dynamic SFT model is done, its limitations can be listed.

Submergence depth

In case the tunnel is located close to the water surface and subjected to short waves, wave forces are over predicted. This causes that tunnel displacements but also tether forces are over predicted. At a submergence depth $s_1 = 0.175m$, the model is limited to waves longer than approximately five times the tunnel structure width. In other words, at $s_1/b \approx 1$, $L/(2a) > 5$. Increasing the submergence depth improves the accuracy of the motion prediction and tether force prediction. At a submergence depth $s_1/b \approx 2$ the model is not limited by the length of waves.

Feedback effect

Feedback effects can not be modeled by the dynamic SFT model. The model is not able to determine the deformed wave field due to the motion of the tunnel structure. In case motions start to increase and the feedback effect grows, model predictions become weaker. Especially for the analysis of motions in time, which can become far different than sinusoidal. The feedback effect is the largest for high waves in combination with a shallow submergence depth. Waves start to break over the structure, causing wave slamming on top of the tunnel. Large motions stimulate the wave breaking even more, causing large second order effects. In the model, the wave forces are determined based on a fixed tunnel, not taking into account feedback effects or wave breaking.

Snapping lines

The snap prediction of the model works very well. For small tether angles e.g. 30, the snap force is almost the same as the tether force predicted by the model. Snap force prediction is possible for stable configurations. However it is not possible to determine the snap forces for unstable configurations. The displacements of the tunnel are not affected allot in case of snapping lines. Displacements are reduced but the model can still be used to estimate the amplitude of the displacements.

Anchorage depth

The model can not be used for predictions in which the anchorage depth is large compared to the SFT tunnel dimensions. For anchorage depths larger than approximately 10 times the structure width, the model assumption for rigid tethers is not realistic anymore. $h_1/(2a) < 10$. This limitation is a rough estimation. Verification at large depths is not performed because of the a lack of physical experimental data.

Tunnel cross section

The model is limited to an aspect ratio of 2.5 with a width of $2a = 0.4m$ and height $b = 0.16m$. This aspect ratio and the size of the tunnel cross section can not be changed for parametric studies. The force prediction coefficients C_{mz}, C_{mx}, C_d and C_{dc}) are dependent on the aspect ratio. The hydro dynamic coefficients C_r, C_s and M_a are dependent on the size of the tunnel cross section. In case it is preferred to change the aspect ratio or the tunnel size, the force prediction coefficients and hydro dynamic coefficients need adaptation, something which is not included in the dynamic SFT model.

Second order effects

The dynamic SFT model is not capable of capturing large second order effects which is due to the model set-up. No wave breaking or diffraction effects are taken into account which causes the wave force module to produces harmonic loads without higher harmonics. The dynamic module is a 1degrees of freedom (DOF) dynamic model calibrated in still water. The coupling module combines the wave force module and dynamic module and does not take into account feedback effects. The result is a more or less harmonic output of the dynamic SFT model.

Current

For the positive and negative sway motions, the model can be used as initial tool. The prediction trends are fine, however the model accuracy is limited. The wave forcing is highly simplified which can cause prediction errors of ±25% for positive displacements and ±60% for negative displacements. The implementation of current in the model should be seen as a trigger for other researchers. This relative simple dynamic model has many applicational options.

5

Parametric study

In this chapter, a parametric study is performed. This study investigates the motion of the submerged floating tunnel and the tether forces by varying parameters. The first part of the parametric study is about the tunnel motion. The second part of the parametric study analyses the tether forces. The third part investigates the slack - taut transition of the tunnel. In the fourth part, safety measures against tether fatigue are analysed. Finally, a sensitivity analysis is provided.

The parameter definitions are presented in figure 5.1. The submergence depth s_1 is the depth on which the top of the tunnel is located. The height and width of the tunnel are indicated with b and $2a$. The tunnel is anchored under a tether angle at a water depth h_1. The connection between the tethers and the tunnel body is indicated with ϵ and γ in which γ can be inward or outward directed. The tunnel is attacked by a linear wave train of wave length L and wave height H. The tether force of the inner tether is indicated with T_{inner}. The tether force of the outer tether is indicated with T_{outer}. A anti clockwise rotation of the tunnel is associated with positive roll and a horizontal motion to the right side is indicated with positive sway. Parameters are chosen within the applicable range of the dynamic SFT model. Deep water waves with a steepness larger than $H/L > 0.142$ tend to break and are out of the applicable range of the current study.
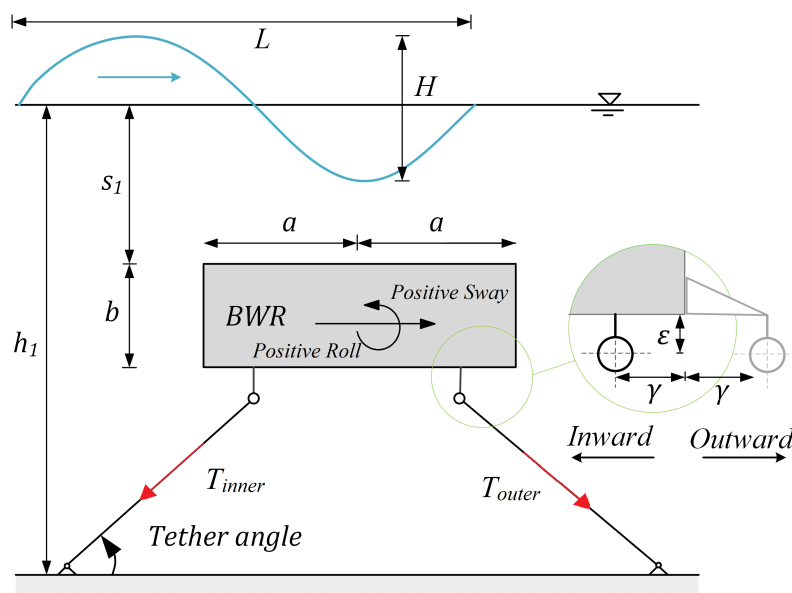
Figure 5.1: Parameter definitions used in parametric study.

5.1. Submerged floating tunnel motions

To study the SFT motion, a reference case is used for which its parametric values can be found in table 5.1.

Table 5.1: Reference case parameter values used in the parametric tunnel motion study.

Parameter	Value	Unit
h_1	1.0	m
$2a$	0.4	m
b	0.16	m
s_1	0.32	m
γ	0.06 (inward)	m
ϵ	0.02	m
BWR	1.5	-
H	0.1	m

The reference case is compared to other cases in which parameters from the reference case are varied. In this way, the effect of parameters on the tunnel motion can be investigated. The motion study is performed for the roll motion (including displacement $\phi(t)$, velocity $\omega(t)$ and acceleration $\alpha(t)$) and the sway motion (including displacement $x(t)$, velocity $v(t)$ and acceleration $a(t)$). The tunnel motion is studied in different circumstances by varying structural and forcing parameters. These parameters are: the buoyancy weight ratio BWR, tether angle, submergence depth s_1, horizontal connection γ and wave length L. The tunnel width $2a$, tunnel height b, connection height ϵ and water depth h_1 are **not** changed during the motion study. The force prediction coefficients and hydro dynamic coefficients are based on the shape of the tunnel. Changing the shape and size of the tunnel cross section would result in prediction errors. Another parameter that is not varied within the motion study is the wave height H. The explanation for this is visualized in figure 5.2. In this figure, the sway displacement is plotted as function of the dimensionless wave height H/b and dimensionless wave length $L/(2a)$. It can be observed that the wave length at which this maximum sway motion occurs is constant and located at $L/(2a) = 4$. Another thing to observe is the linear relation between the wave height and sway displacement. The spacing between the contour lines at $L/(2a) = 4$ is almost constant. The wave height H is therefore assumed to be a magnitude scalar of the response and therefore not of interest in this parametric study. A non dimensional wave height of $H/b = 0.625$ is used in the entire motion study. Please note that for other configurations, the maximum displacement is found for a different wave length.
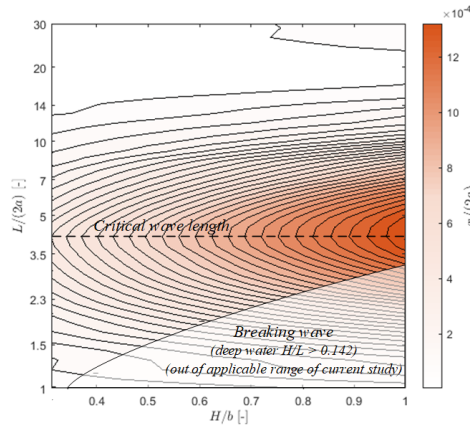
Figure 5.2: Relation between non dimensional wave length $L/(2a)$ and non dimensional wave height H/b and the sway motion $x/(2a)$. Tunnel width $2a$ and tunnel height b are constant while the wave length L and wave height H are variable. Simulation is performed with parameters from the reference case located in table 5.1. Tether angle = 50°.

An overview of the parametric study on the motion of the SFT is given in table 5.2. In total three different studies are performed. The first shows the effect of the submergence depth, the second the effect of the buoyance to weight ratio (BWR) and the last the effect of the tether connection. The cases from table 5.2 are compared with the reference case of which its parametric values can be found in table 5.1. Table 5.2 also shows in which paragraph the parametric study can be found.

Table 5.2: Submerged floating tunnel motion parametric study overview.

Study on roll and sway motion	Dimensionless parameter		Range
Effect of submergence depth.	$L/(2a)$	with $2a$ fixed	1-30
Paragraph 5.1.1	Tether angle		20-80
	s_1/b	with b fixed	1.0
Effect of BWR.	$L/(2a)$	with $2a$ fixed	1-30
Paragraph 5.1.2	Tether angle		20-80
	BWR		2.0
Effect of tether connection.	$L/(2a)$	with $2a$ fixed	1-30
Paragraph 5.1.3	Tether angle		20-80
	$\gamma/(2a)$	with $2a$ fixed	0.15 outward

In the parametric study, only the positive tunnel motions are analysed. Tunnel motions in the same direction as the wave propagation direction gives higher excitation's. The positive tunnel motions are therefore governing with respect to negative tunnel motions. This can be observed in chapter 4, figure 4.12.

5.1.1. Effect of submergence depth

Changing the submergence depth influences the motion of the SFT. This section illustrates the effect of a decrease in submergence depth from $s_1/b = 2.0$ to $s_1/b = 1.0$ while the water depth h_1 remains constant.

First the roll motion is discussed, presented in figure 5.4. In this figure, the first column of figures represents the reference case with a submergence depth of $s_1/b = 2.0$. The second column of figures is simulated with a decreased submergence depth of $s_1/b = 1.0$. From top to bottom the roll displacement, roll velocity and roll acceleration are plotted as function of the tether angle and the wave length / structure length ratio $L/(2a)$. Each roll motion is discussed separately. It can be observed that the roll motions become larger in magnitude when the submergence depth becomes smaller. The maximum roll displacements are found for $L/(2a) = 8$ with a tether angle of 65°. The tunnel roll displacement becomes more sensitive to shorter waves in combination with a smaller tether angle when decreasing the submergence depth. The same phenomena can be found for the roll velocity and the roll acceleration. Decreasing the submergence depth makes the 'sensitivity center' move to wards the shorter waves and smaller tether angles. However the roll acceleration is most sensitive to the shorter waves.

The sway motion is presented in figure 5.5. In this figure, the first column of figures represent the reference case with a submergence depth of $s_1/b = 2.0$. The second column of figures is simulated with a decreased submergence depth of $s_1/b = 1.0$. From top to bottom the sway displacement, sway velocity and sway acceleration are plotted as function of the tether angle and $L/(2a)$ ratio. Sway motions become larger in magnitude when the submergence depth becomes smaller. It can be observed that the sway motions are much more sensitive to the longer waves. The largest sway displacement occurs with $L/(2a) \approx 20$. The sway displacement motion is a long scale motion and is largest for a tether angle approaching 90°. The sway velocity and sway acceleration are more sensitive to shorter waves with $L/(2a) \approx 5$. A decrease of the submergence depth has the largest influence on the sway velocity and sway acceleration. The sensitivity centre moves down towards the shorter waves. However the most sensitive tether angle remains the same.

An explanation of the influence of the submergence depth on the tunnel motion in given in figure 5.3. Short waves are not able to reach the tunnel body when it is located at a large submergence depth. Longer waves are reaching deeper in the water column. When the tunnel body is located closer to the water surface, shorter waves start to have more impact on the structure. Because these waves are steeper, water accelerations and pressure differences are higher which causes larger displacements. Close to the water surface, the sensitivity centre of the roll acceleration approaches $L/(2a) = 2$ with a tether angle of around $30-40°$. This roll dominant system is presented in figure 5.3B. Longer waves in combination with a large tether angle creates a sway dominant system which can be seen in figure 5.3C. The pressure profile over the water depth becomes more or less linear and the forcing becomes purely horizontal which results in the largest sway motions. If the wave length becomes large, velocities and accelerations become smaller. Velocities and accelerations of the tunnel are always more sensitive to shorter waves than the displacements because the time scale of the wave oscillation is faster. A faster change in wave motions gives higher velocities and accelerations.
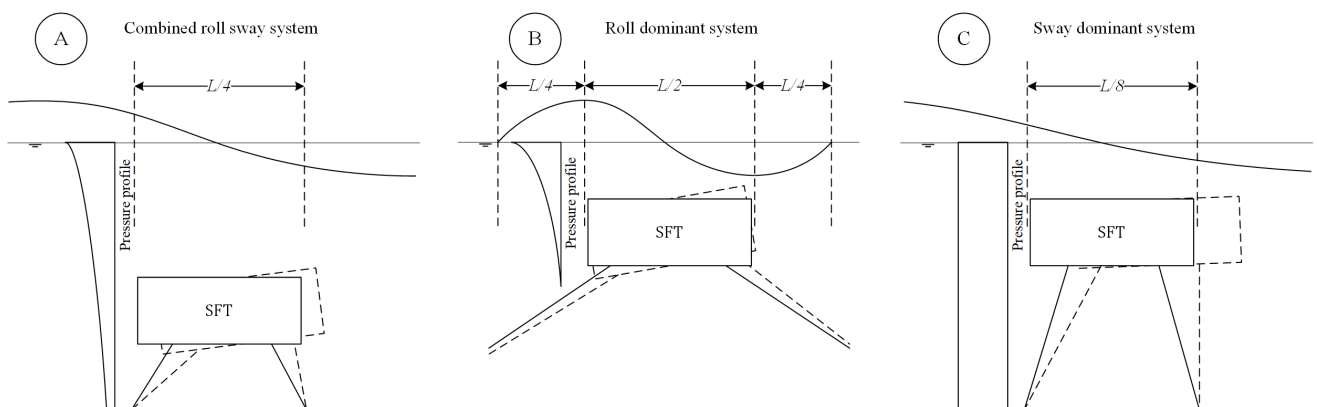
Figure 5.3: Schematization of a combined, roll dominant and sway dominant system.
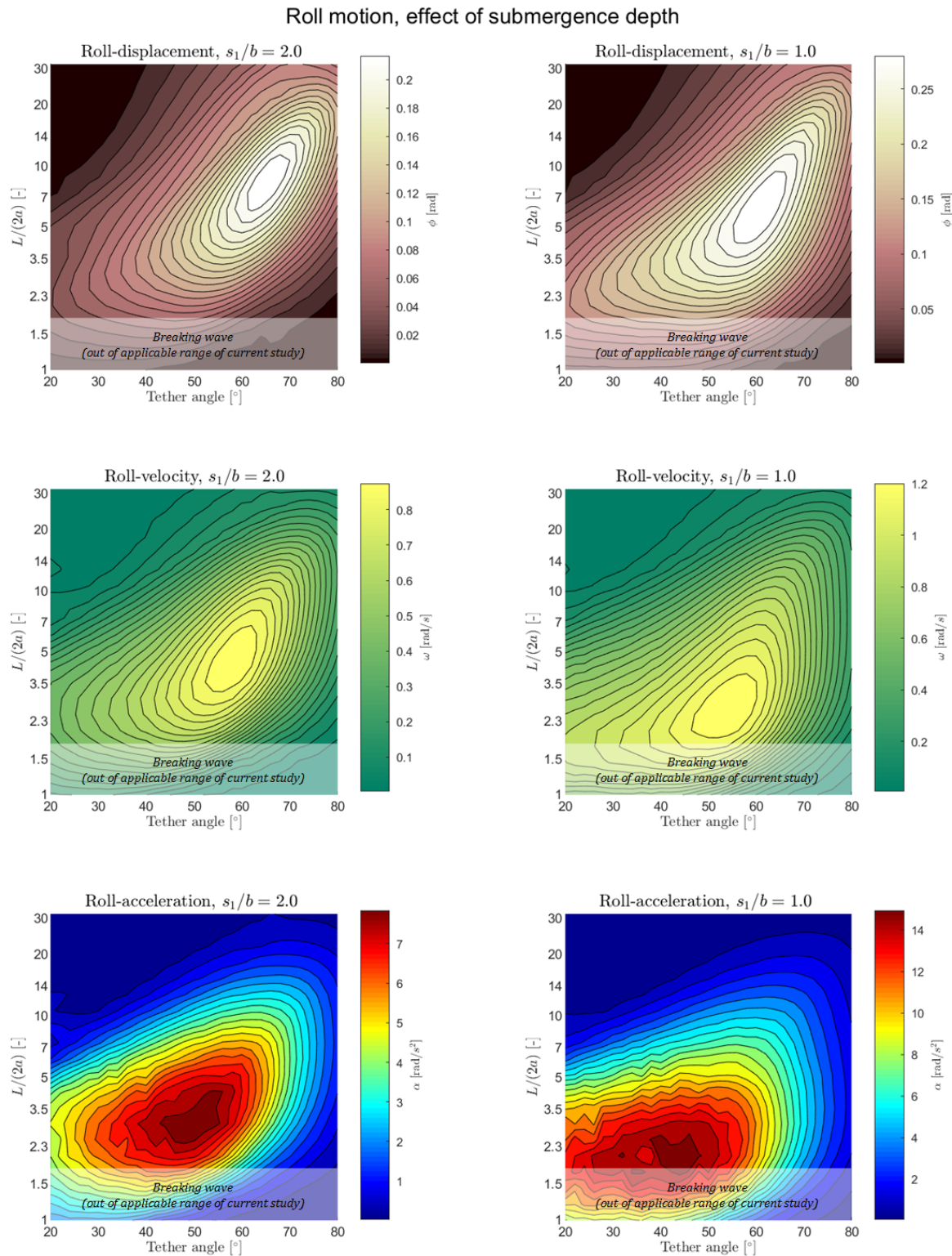
Figure 5.4: The effect of the submergence depth on the roll motion of the SFT. The left column of figures represents the reference case with parameters from table 5.1. The right column of figures show the effect of a decrease in submergence depth from $s_1/b = 2.0$ to $s_1/b = 1.0$.
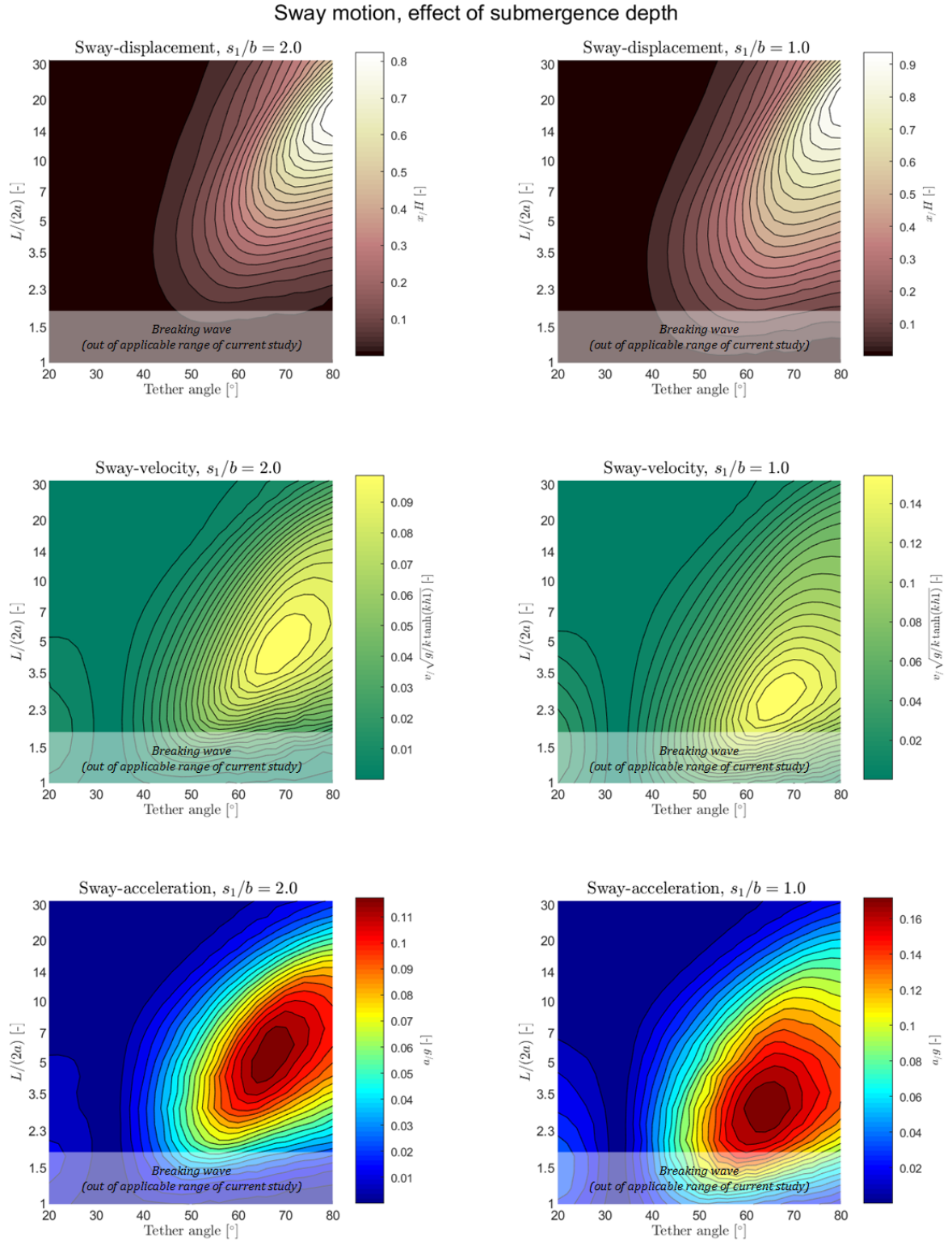
Figure 5.5: The effect of the submergence depth on the sway motion of the SFT. The left column of figures represents the reference case with parameters from table 5.1. The right column of figures show the effect of a decrease in submergence depth from $s_1/b = 2.0$ to $s_1/b = 1.0$.

5.1.2. Effect of BWR

Changing the BWR influences the motion of the SFT. This section illustrates the effect of an increase in BWR from $BWR = 1.5$ to $BWR = 2.0$.

First the effect of the BWR on the roll motion is discussed, presented in figure 5.6. In this figure, the first column of figures is simulated with the parameters from the reference case in which a BWR of $BWR = 1.5$ is used. The second column of figures is simulated with a BWR of $BWR = 2.0$. From top to bottom the roll displacement, roll velocity and roll acceleration are plotted as function of the tether angle and the wave length / structure length ratio $L/(2a)$. Each roll motion is discussed separately. It can be observed that an increase in BWR has a large influence on the wave length / structure length ratio. A tunnel with a larger BWR is more sensitive to smaller waves. This effect is the largest for the roll displacement and roll velocity. The roll acceleration remains sensitive to $L/(2a) \approx 3$. Increasing the BWR causes the sensitivity center to shift towards the larger tether angles. This effect is largest for the roll acceleration. Increasing the BWR causes roll displacements to be smaller in magnitude. For roll velocities and roll accelerations, the magnitudes are almost similar to the reference case with $BWR = 1.5$.

The sway motion is presented in figure 5.7. In this figure, the first column of figures is simulated with the parameters from the reference case in which a BWR of $BWR = 1.5$ is used. The second column of figures is simulated with a BWR of $BWR = 2.0$. From top to bottom the sway displacement, sway velocity and sway acceleration are plotted as function of the tether angle and $L/(2a)$. It can be observed that a larger BWR gives smaller sway displacements. The sway velocities and sway accelerations become larger when increasing the BWR. For all sway motions, the sensitivity centre shifts towards the shorter waves. Increasing the BWR does not have an effect on the location of the sway sensitivity center in terms of tether angles.

An explanation for the obtained results is given. An increase in BWR causes the mass to decrease which lowers the inertia of the entire dynamic system. The tether forces become larger which gives a higher stiffness of the dynamic system. These two effect causes that the natural frequency of the system becomes higher. This makes the structure more sensitive for shorter waves, making the sensitivity center of the roll motions and sway motions shift towards the smaller waves. A larger stiffness of the dynamic system results in smaller displacements for both the roll and sway.
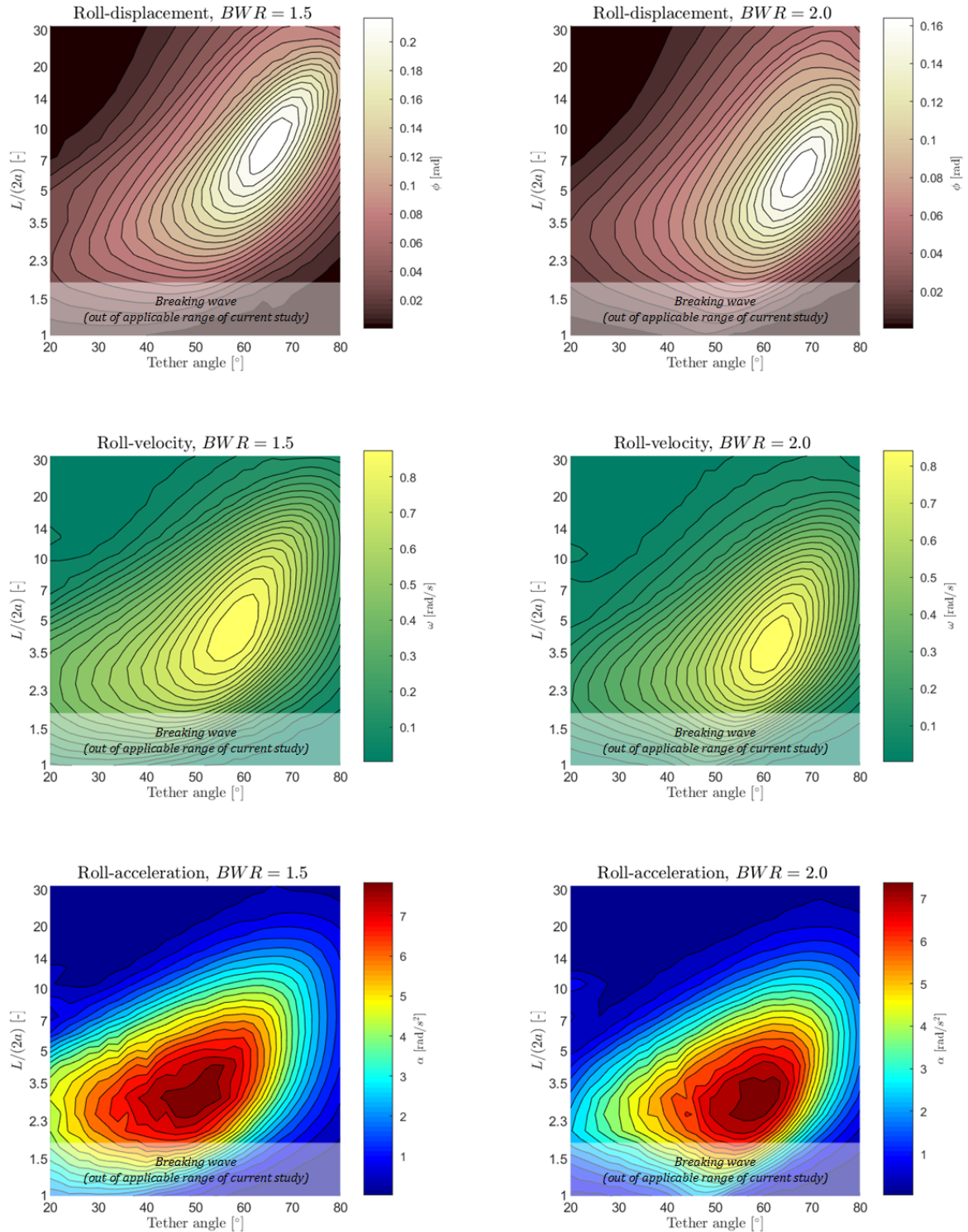
Figure 5.6: The effect of the BWR on the roll motion of the SFT. The left column of figures represents the reference case with parameters from table 5.1. The right column of figures show the effect of an increase in BWR from $BWR = 1.5$ to $BWR = 2.0$.
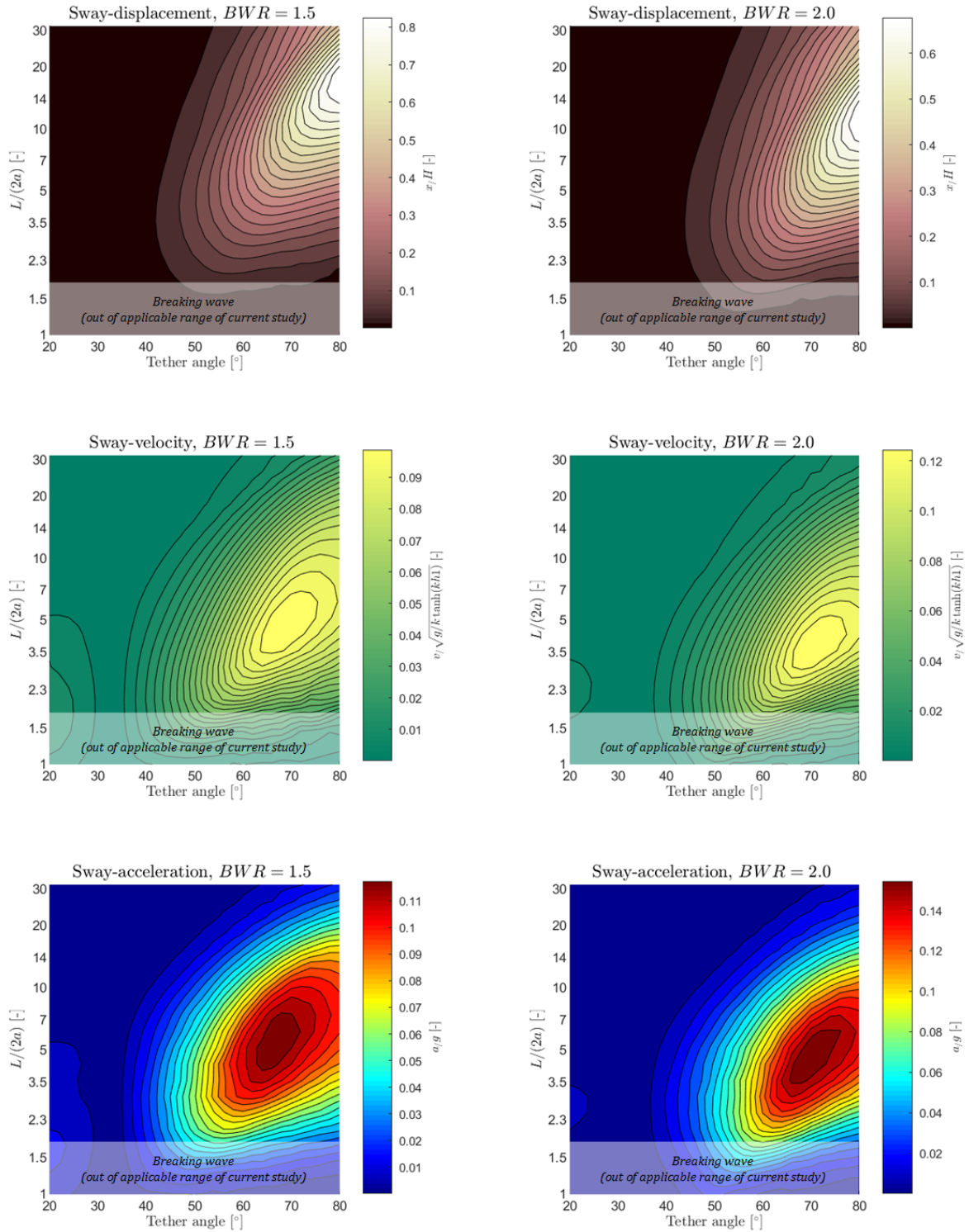
Figure 5.7: The effect of the BWR on the sway motion of the SFT. The left column of figures represents the reference case with parameters from table 5.1. The right column of figures show the effect of an increase in BWR from $BWR = 1.5$ to $BWR = 2.0$.

5.1.3. Effect of tether connection

The motion of the SFT can be influenced by adapting the tether connection support. In the previous cases, the tethers are connected inward of the sides of the tunnel body. In this section, the effect of an outward directed tether connection support is analysed. A schematization of this outward tether connection support is given in figure 5.8.
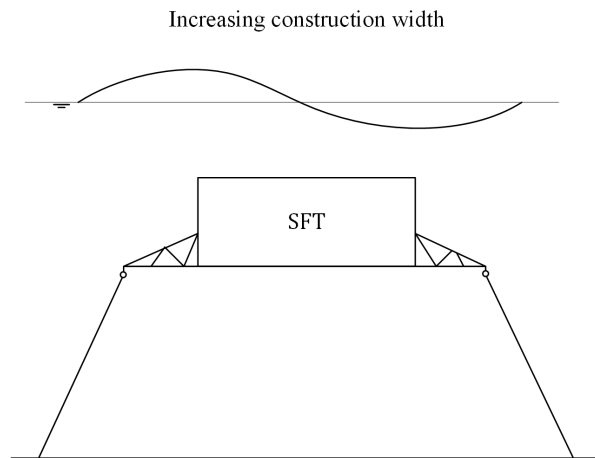
Figure 5.8: Schematization of SFT with tethers connection outward of the tunnel body.

First the effect of the tether connection support width on the roll motion is discussed, presented in figure 5.9. In this figure, the first column of figures is simulated with the parameters from the reference case in which a tether connection width of $\gamma/(2a) = 0.15$ (inward) is used. The second column of figures is simulated with a tether connection width of $\gamma/(2a) = 0.15$ (outward). From top to bottom the roll displacement, roll velocity and roll acceleration is plotted as function of the tether angle and the wave length / structure length ratio $L/(2a)$. Increasing the construction width by placing the tether connection outside the tunnel body reduces the magnitude of all roll motions. Also the location of the sensitivity center changes. The roll displacement becomes sensitive to shorter waves. This effect is also visible for the roll velocity and roll acceleration, however this effect is small. The sensitivity center shifts towards the smaller tether angles when the tether connection is placed outward of the tunnel body. The most remarkable effect is that the sensitivity plot becomes more concentrated around the sensitivity center.

The sway motion is presented in figure 5.10. In this figure, the first column of figures is simulated with the parameters from the reference case in which a tether connection width of $\gamma/(2a) = 0.15$ (inward) is used. The second column of figures is simulated with a tether connection width of $\gamma/(2a) = 0.15$ (outward). From top to bottom the sway displacement, sway velocity and sway acceleration are plotted as function of the tether angle and $L/(2a)$. Placing the connection sideways of the tunnel body causes smaller sway displacements. The sway velocities and sway accelerations become larger. All sway motions become more sensitive to the shorter waves. The sway velocity and sway acceleration becomes more sensitive to smaller tether angles. The largest sway displacements are still found for a tether angle of 90°.

An explanation for the obtained results is given. Increasing the construction width increases the rotational inertia of the structure. This causes an decrease in magnitude of all roll motions.
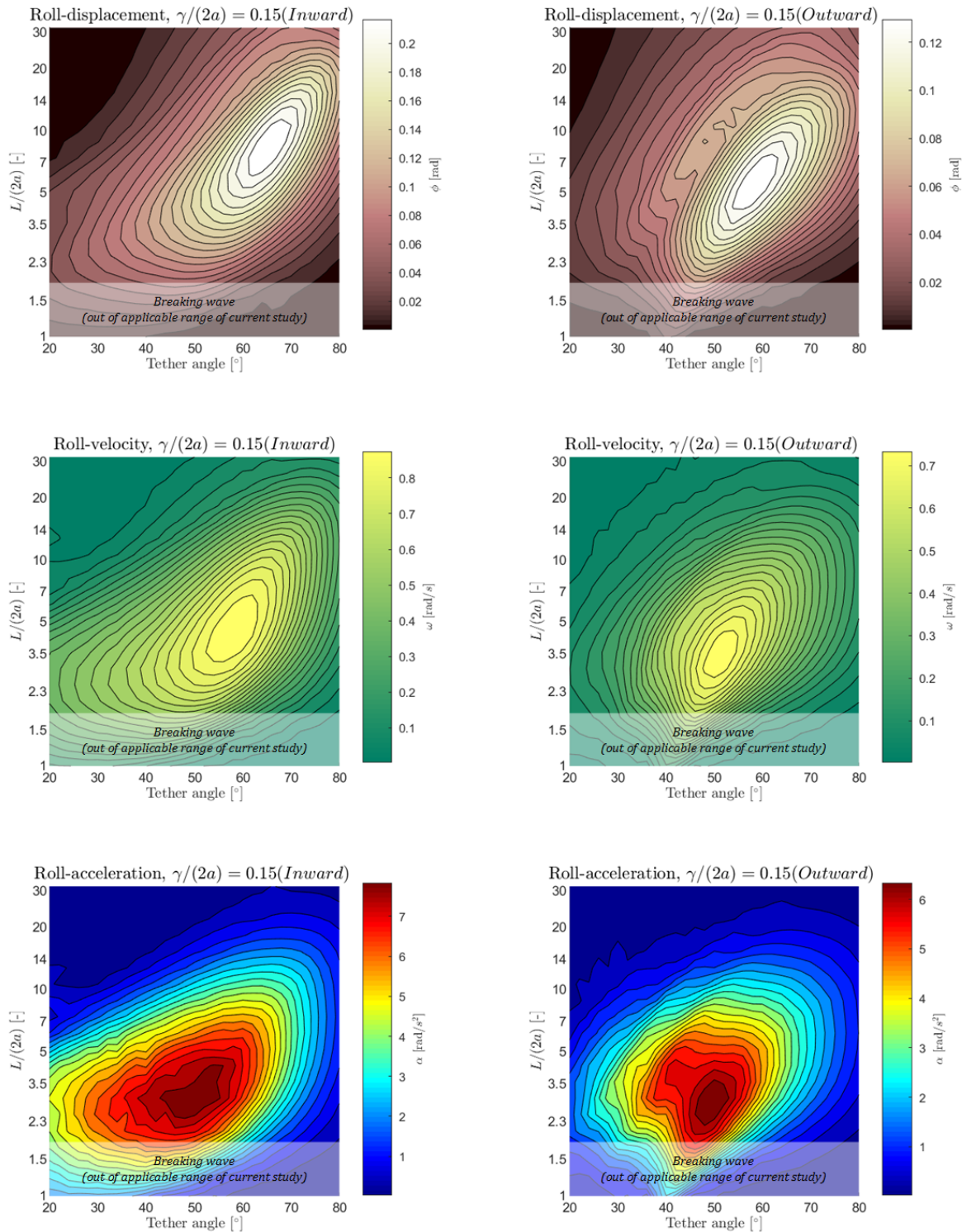
Figure 5.9: The effect of the tether connection on the roll motion of the SFT. The left column of figures represents the reference case with parameters from table 5.1. The right column of figures show the effect of a change in connection width from $\gamma/(2a) = 0.15$ (inward) to $\gamma/(2a) = 0.15$ (outward)
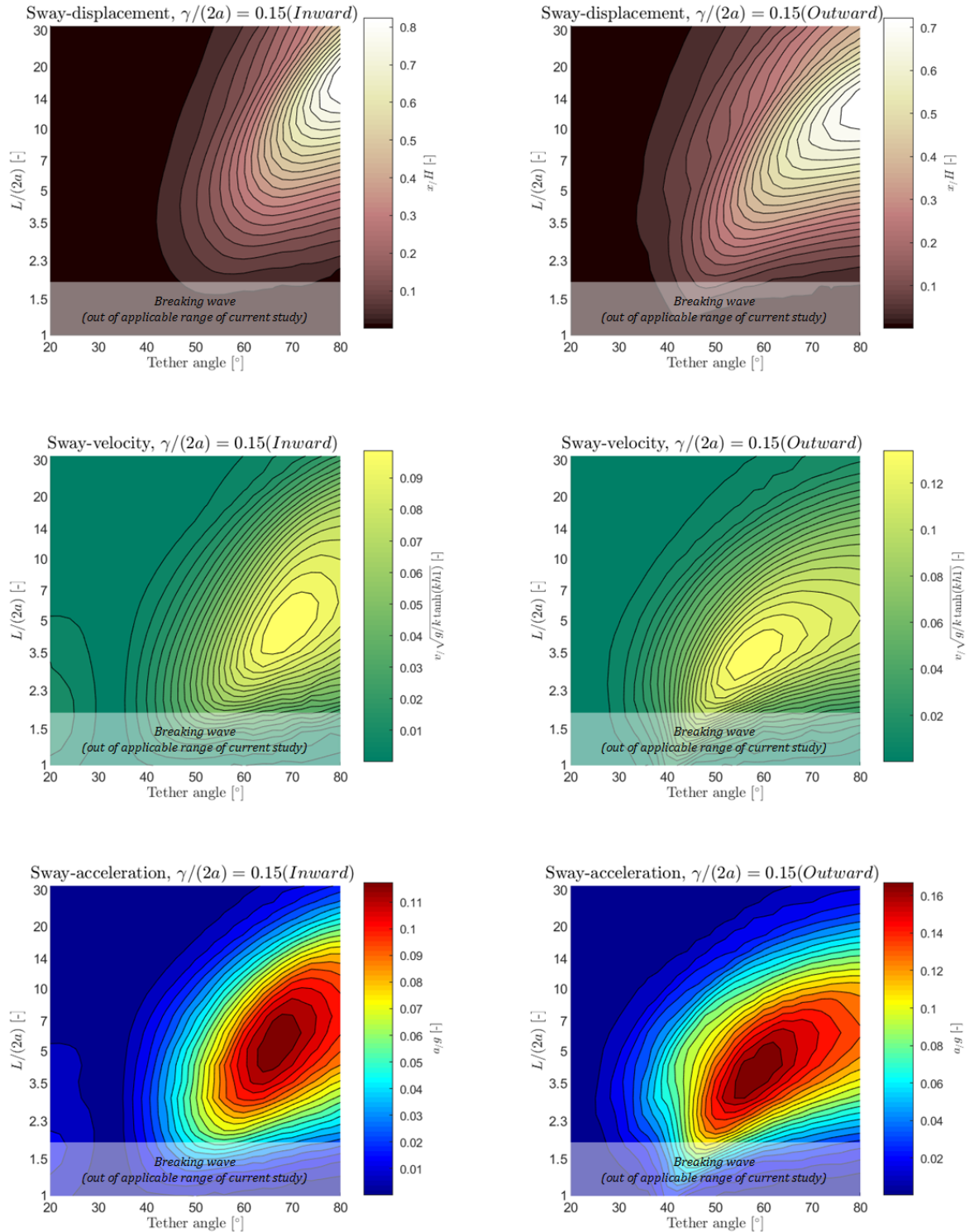
Figure 5.10: The effect of the tether connection on the sway motion of the SFT. The left column of figures represents the reference case with parameters from table 5.1. The right column of figures show the effect of a change in connection width from $\gamma/(2a) = 0.15$ (inward) to $\gamma/(2a) = 0.15$ (outward)

5.2. Tether forces

In this section, a parametric study is performed on the maximal tether force. In this study, only the tether located at the incident wave side (inner tether) is analysed because this is governing with respect to the outer tether. The influence of structural parameters, as function of the wave length, on the maximal inner tether force is investigated and can be found in paragraph 5.2.1. The influence of structural parameters, as function of the wave height, on the maximal inner tether force is investigated and can be found in paragraph 5.2.2. In both paragraphs, the maximal tether force has been made non dimensional by dividing the tether force by the buoyancy force. The buoyancy force is the resultant upward directed force of which its magnitude can be determined with eq 5.1 in which m is the mass of the SFT body.

$$F_b = (BWR - 1)mg \qquad (5.1)$$

The parameters that are used in this tether force study can be found in table 5.3.

Table 5.3: Reference case parameter values used in the parametric tether force study.

Parameter	Value	Unit
h_1	1.0	m
$2a$	0.4	m
b	0.16	m
s_1	0.32	m
γ	0.06 (inward)	m
ϵ	0.02	m
BWR	1.5	-
Tether angle	50	°

5.2.1. Maximal tether force as function of wave length

First the effect of the wave length on the tether force is investigated. In figure 5.11, the influence of structural parameters on the maximal tether force is presented. This study is performed for a range of wave lengths. The simulations are performed with parameters from table 5.3. In figure 5.11a, it can be seen that the largest tether forces are found for the smallest tether angles. This is logical because of the geometric relations. The vertical component of the tether force needs to make vertical equilibrium. When the tether makes a large angle with respect to the vertical, the tether force needs to be large to make equilibrium. In the same figure, the critical wave length as function of the tether angle is plotted. It can be seen that configurations with large tether angles are more sensitive to longer waves. In figure 5.11b, the influence of the submergence depth in combination with the wave length is plotted. A tunnel that is placed close to the still water level has larger tether forces than a tunnel with a larger submergence depth. A tunnel with a large submergence depth is more sensitive to longer waves. This is indicated with a critical wave length line. In figure 5.11c, the influence of the BWR in combination with the wave length is plotted. The largest tether forces are found for a large BWR. However, in this figure the tether force is divided by the buoyancy force. In this way, it can be seen that structures with a low BWR have a relative larger tether force than structures with a high BWR. Structures with a high BWR have less motion which results in lower tether forces. Increasing the BWR does not causes a change in wave length sensitivity which can be seen by the dashed critical wave length line. In figure 5.11d, the influence of the tether connection in combination with the wave length is plotted. It can be observed that increasing the width of the tether connection structure does not have any influence on the magnitude of the tether forces. The critical wave length is independent of the tether connection.
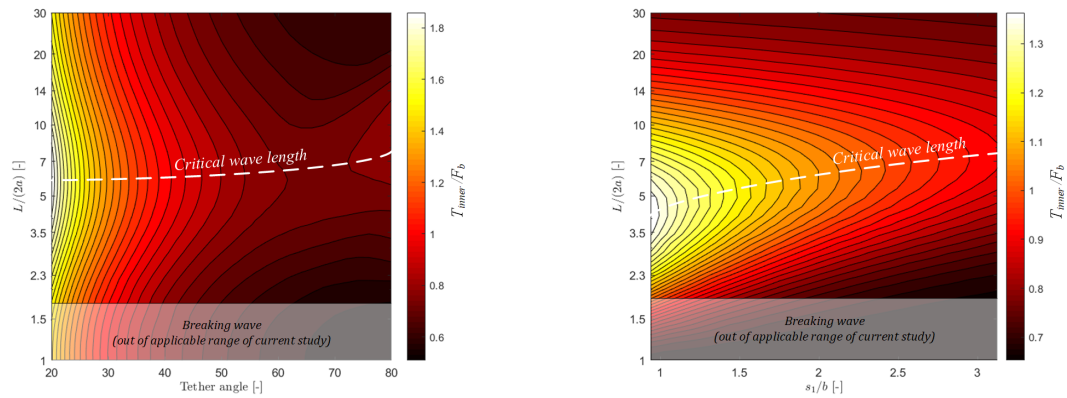
(a) Influence of the tether angle,
tether angle range $[20° - 80°]$.

(b) Influence of the submergence depth,
s_1 range $[0.15m - 0.50m]$.
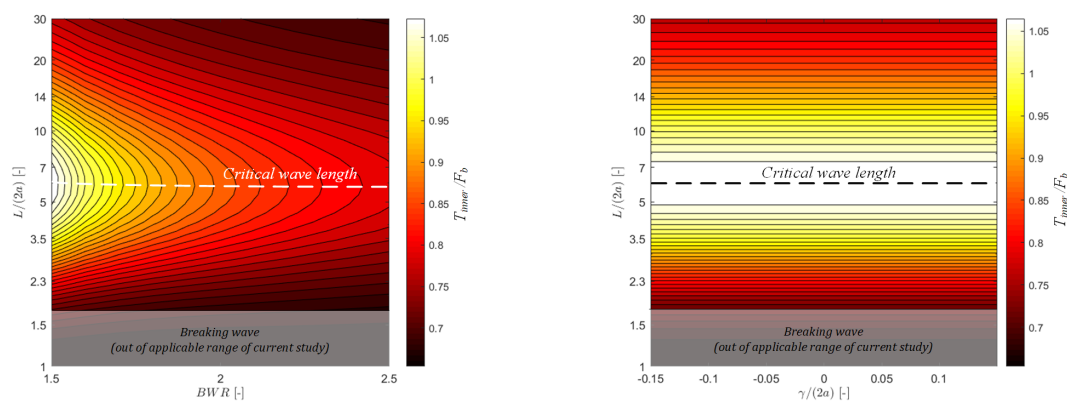
(c) Influence of the BWR,
BWR range $[1.5 - 2.5]$.

(d) Influence of the tether connection,
γ range $[0.06m$ outward$-0.06m$ inward$]$.

Figure 5.11: The influence of structural parameters, as function of the non dimensional wave length, on the maximal inner tether force. Tether force has been made non dimensional by dividing the tether force by the buoyancy force F_b. Simulation is performed with parameters from 5.3. $H/b = 0.625m$

5.2.2. Maximal tether force as function of wave height

In this paragraph, the effect of the wave height on the tether force is investigated. In figure 5.12, the influence of structural parameters on the maximal tether force is presented. This study is performed for a range of wave heights. The simulations are performed with parameters from table 5.3. First the effect of the tether angle is discussed, which can be found in figure 5.12a. The largest tether forces are again found for the smallest tether angles. An increase in wave height causes an increase in tether force. However it can be seen that the smallest tether forces are not found for the largest tether angles. The smallest tether forces are found at around 63°. For larger tether angles than 63°, the motion of the structure causes a larger increase in tether force than the decrease of the static tether force. In figure 5.11b, the influence of the submergence depth in combination with the wave height is plotted. A larger wave height gives larger tether forces. An increase in submergence depth causes a decrease in tether forces. In figure 5.12c, the effect of the BWR in combination with the wave height on the tether force is plotted. Large non dimensional tether forces are found for a small BWR. For a small BWR, motions become larger which causes an increase in tether forces. The effect of the tether connection on the tether forces can be found in figure 5.12d. It can be observed that increasing the width of the tether connection structure does not have any influence on the magnitude of the tether forces. Increasing the wave height always results in an increase in tether force. However the rate of increase is purely dependent on the configuration that is chosen. In figure 5.13, the wave height is plotted against the wave length. Increasing the wave height does not change the location of the most critical wave length indicated by the black dashed line. It can be concluded that the wave height is a magnitude scalar.
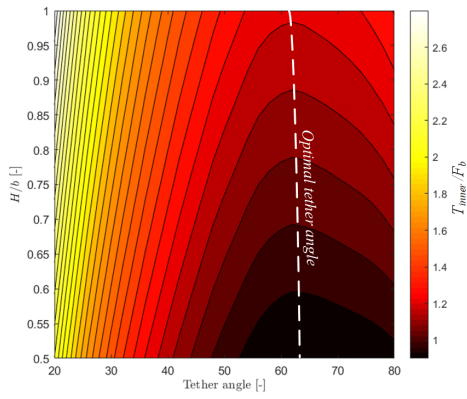
(a) Influence of the tether angle,
tether angle range $[20° - 80°]$.
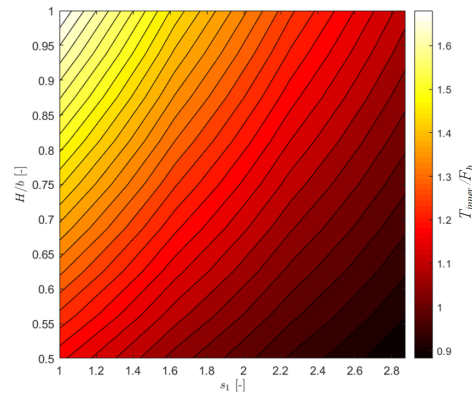
(b) Influence of the submergence depth,
s_1 range $[0.15m - 0.50m]$.
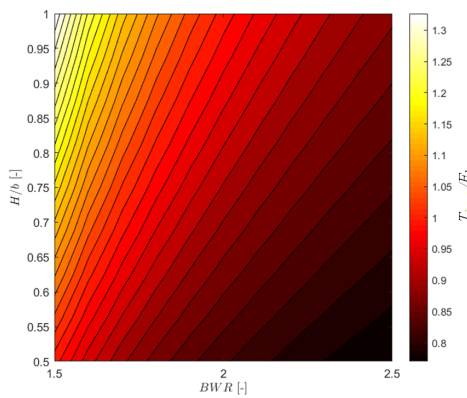
(c) Influence of the BWR,
BWR range $[1.5 - 2.5]$.
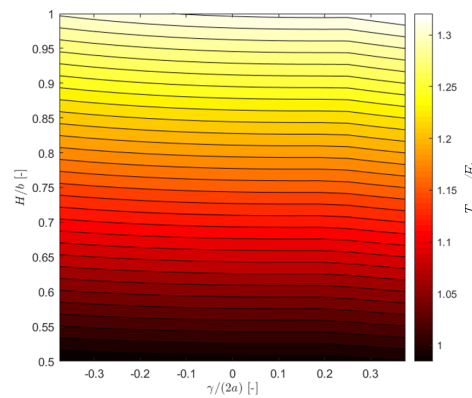
(d) Influence of the tether connection,
γ range $[0.06m\ outward - 0.06m\ inward]$.

Figure 5.12: The influence of structural parameters, as function of the non dimensional wave height, on the maximal inner tether force. Tether force has been made non dimensional by dividing the tether force by the buoyancy force F_b. Simulation is performed with parameters from 5.3. $L/(2a) = 6$
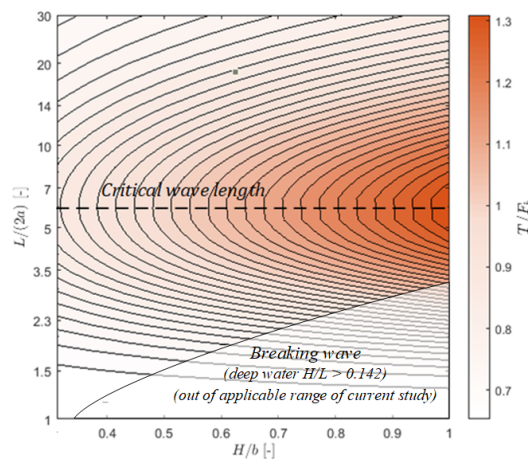
Figure 5.13: Relation between non dimensional wave length $L/(2a)$ and non dimensional wave height H/b and the maximum inner tether force T_{inner}/F_b. The construction width $2a$ and construction height b are fixed.

5.3. Slack-taut transition

In the previous section, the maximum tether force was analysed in detail. This maximum tether force is important for the design of the tether dimensions. However the minimum tether force needs to be analysed as well. In case the tether force becomes zero, no tension force is present anymore. Without taut in the tethers, relaxation takes place, followed by high snap forces. Tether slack must be avoided at all times! The transition between a tether under tension and a relaxation of this tether is indicated by a taut-slack transition. The most dominant structural parameters influencing this taut-slack transition are the BWR, tether angle and submergence depth. In this section, the slack taut transition is studied. The parameters that are used are presented in table 5.4.

Table 5.4: Reference case parameter values used in the parametric slack-taut transition study.

Parameter	Value	Unit
h_1	0.7	m
$2a$	0.4	m
b	0.16	m
ϵ	0.02	m
γ	0.06 (inward)	m

In figure 5.14, a slack-taut sensitivity map is presented. This map indicates for which combinations of the BWR and tether angle, slack or taut will occur. The slack area is indicated with red while the snap area is indicated with blue. The transition between the slack and taut is indicated with a black contour line displaying zero tension. Below this line the tunnel has snapping lines. In figure 5.14, the tether force below the transition line becomes negative. Because tethers can only take tension forces, the magnitude of this negative tension force is not representative. Negative tether forces are due to the model set up. In the model, the tethers are modelled as rigid bars which are able to take pressure forces. Therefore a snapping tether can be predicted but the magnitude of the snap force can not be determined. From figure 5.14 it can be observed that structures with a low BWR (for example 1.25) are likely to snap. Configurations with large tether angles have the tendency to snap earlier than configurations with a small tether angle. A structure with a tether angle of 80° will snap at a BWR of 1.35 while a structure with a tether angle of 40° will not snap with that same BWR. It should be noted that the position of the slack taut transition contour in figure 5.14 is strongly dependent on the chosen wave conditions and submergence depth.
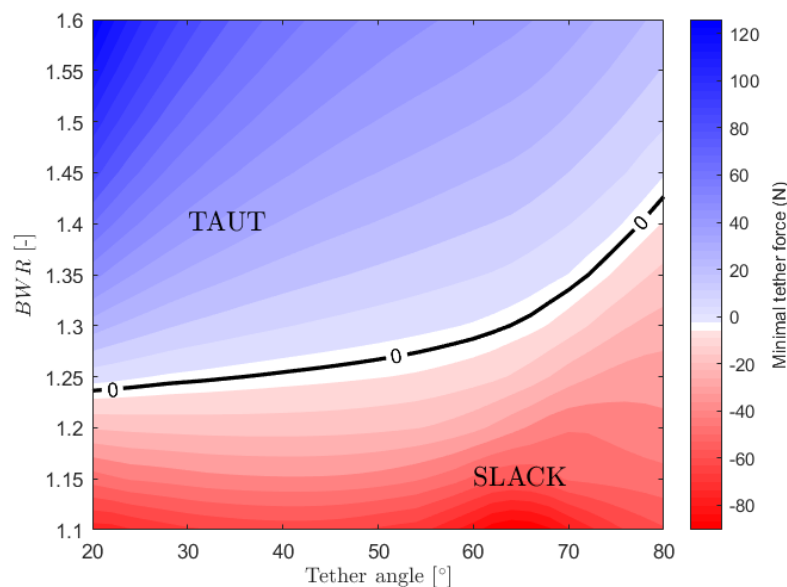
Figure 5.14: Slack-taut sensitivity map. Blue indicates taut in the tether (no snapping line). Red indicates slack in the tether (snapping line). Black line indicates the no tension contour. $s_1/b = 2.5$, $H/b = 1.0$, $L/(2a) = 6.0$. The construction width $2a$ and construction height b are fixed.

To determine whether structures are likely to have snapping lines, prediction graphs can be a very handy tool. The most important information for such a graph is the transition line between the slack taut regions. Below the transition line, a structure has snapping lines. Above the transition line, the tethers have taut. In figure 5.15, a slack-taut prediction graph is provided. This graph consists of 6 figures. Each row of figures shows a different submergence depth, top row $s_1/b = 2.5$, middle row $s_1/b = 2.0$ and bottom row $s_1/b = 1.5$. The left column of figures shows the transition line between the slack taut regions for different wave lengths. In red, the transition line for the most critical wave length is plotted. At this wave length / structure length ratio $L/(2a)$, snap happens with the highest BWR. It can be seen that the critical $L/(2a)$ ratio depends on the submergence depth, something that was already discussed in the previous section. Because the critical wave length is not dependent on the wave height, it is possible to plot the critical transition contour for different wave heights. This is done in the right column of figure 5.15. In case the designer knows the design wave height and the submergence depth, it is possible to determine the BWR for which the structure has no snapping lines.
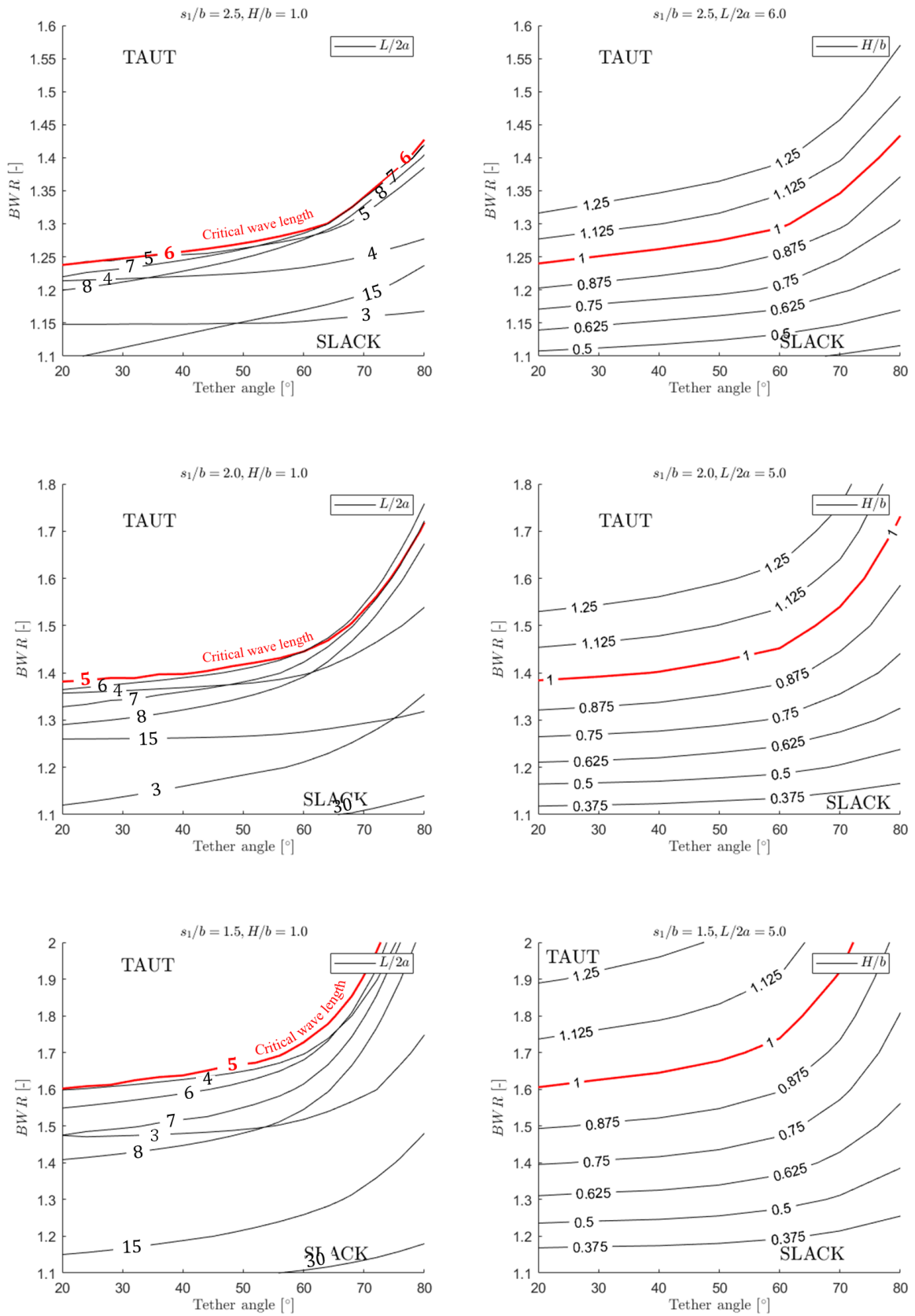
Figure 5.15: Slack-taut prediction graph indicating slack-taut transition lines for different wave heights in the left column. Top row $s_1/b = 2.5$, middle row $s_1/b = 2.0$ and bottom row $s_1/b = 1.5$. The construction width $2a$ and construction height b are fixed.

5.4. Safety against tether fatigue

The mooring tethers of a SFT are subjected to applied load fluctuations during their life time which creates the possibility of fatigue failure (K.H.Frank, 1991). The variation in tether stress needs to be controlled to guarantee safety. The design stress range for tethers is dependent on the number of load cycles. This can be observed in figure 5.16, in which for four types of wires, the stress range is visualized. The stress range is
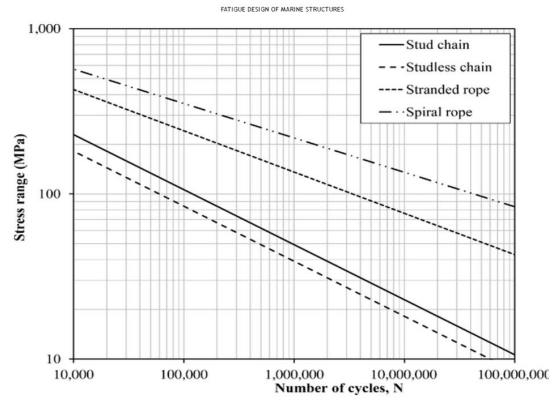
Figure 5.16: Fatigue design of marine structures (Lotsberg, 2016).

bounded by the maximal and minimal tether stress. Depending on the tether material and the number of loading cycles, a safety ratio between the maximal and minimal tether force can be determined. This ratio is denoted as R. In this parametric study, the maximum value of R is assumed to be 3. However this is a rough estimation because no guidelines for the SFT are made yet. If the ratio between the maximal and minimal tether force transcend a value of 3, safety is not guaranteed. In other words: $max(T)/min(T) = R < 3$.

In figure 5.17, the tether ratio R is plotted as function of the BWR and the tether angle. Three areas can be distinguished. These are: $R < 3$ (safe taut), $R > 3$ (unsafe taut) and slack. The transition contour between safe and unsafe taut is the most important information. Above this line, the tunnel configuration has a safe taut condition. The parameters that are used in this fatigue study are presented in table 5.4.
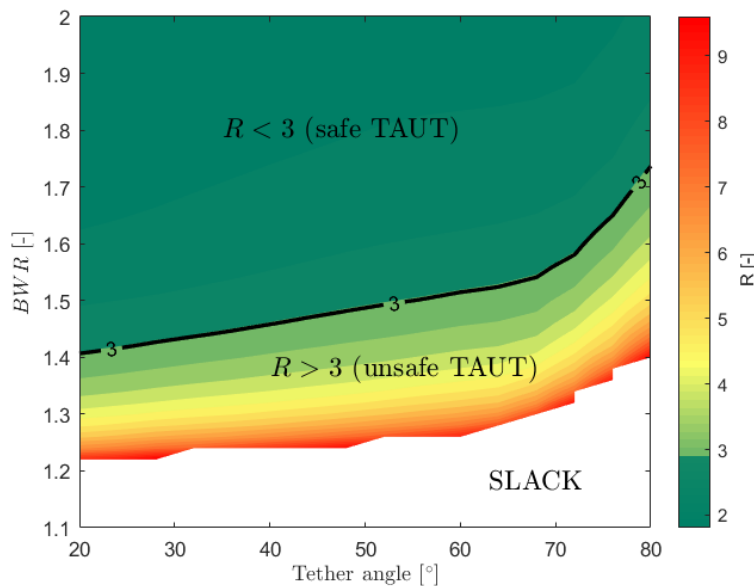
Figure 5.17: Tether force ratio map. Green indicates a safe tether force ratio under taut conditions. Yellow-red colors indicate an unsafe tether force ratio under taut conditions. In the white area, slack occurs. Black line indicates the transition line between safe and unsafe taut conditions. $s_1/b = 2.5$, $H/b = 1.0$, $L/(2a) = 6.0$. The construction width $2a$ and construction height b are fixed.

Likewise figure 5.15, a prediction graph can be constructed which shows the transition line between safe and unsafe taut conditions. This graph can be found in figure 5.18. Again the figure consists of 6 figures of which each row represents a submergence depth, top row $s_1/b = 2.5$, middle row $s_1/b = 2.0$ and bottom row $s_1/b = 1.5$. The left column of figures shows the transition line between the safe slack and unsafe slack conditions for different wave lengths. In red, the transition line for the most critical wave length is plotted. In the right column of figure 5.18, the transition line for the critical wave length is plotted for a range of wave lengths. In case the designer knows the design wave height and the submergence depth, it is possible to determine the BWR for which the structure has safe taut conditions.
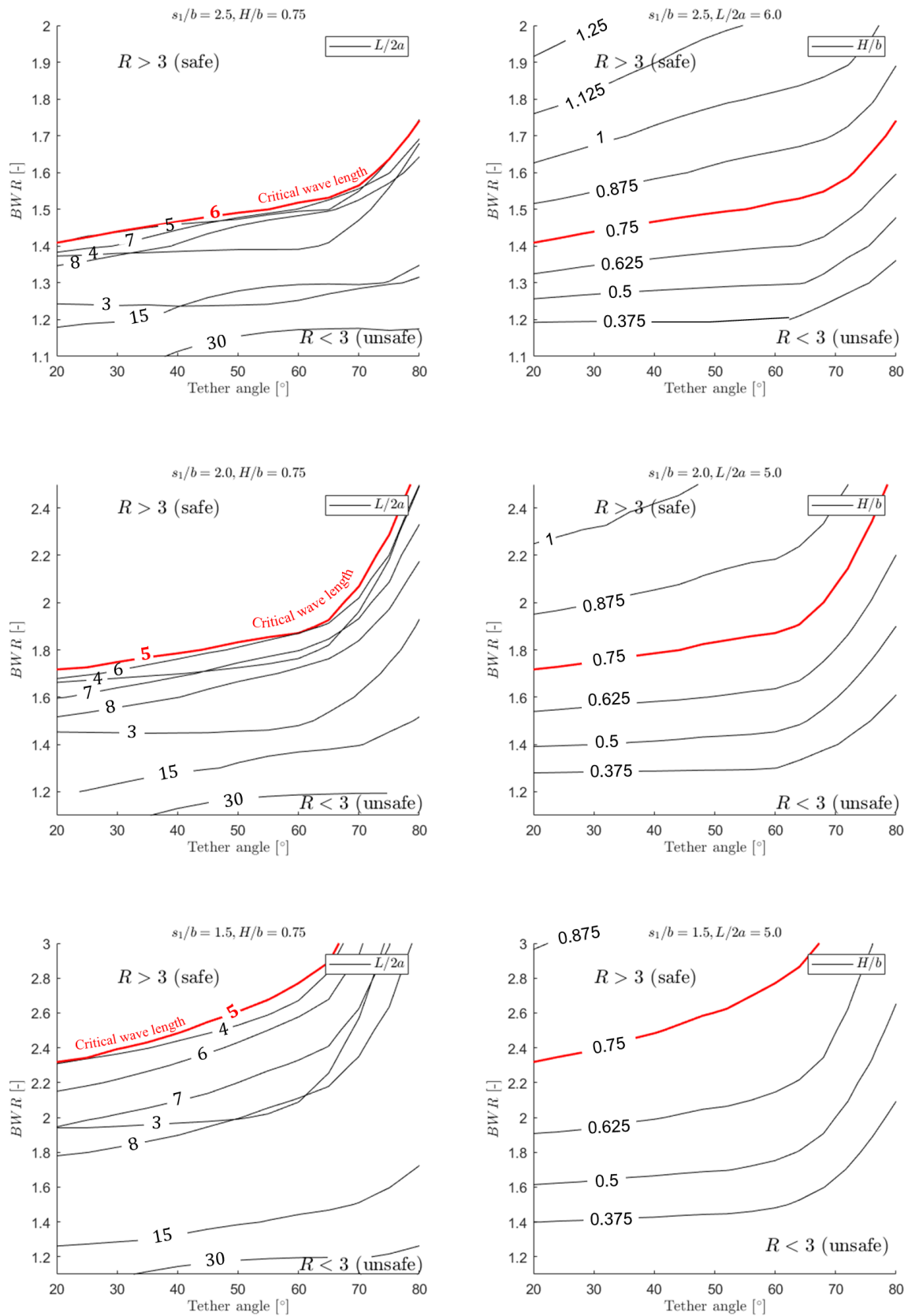
Figure 5.18: Design graph indicating safety tether ratio transition lines for different wave heights in the left column. Top row $s_1/b = 2.5$, middle row $s_1/b = 2.0$ and bottom row $s_1/b = 1.5$. The construction width $2a$ and construction height b are fixed.

5.5. Sensitivity study

A sensitivity study is performed to study the influence of independent input parameters on the output of the dynamic SFT model. The outcome of this sensitivity analysis is presented in figure 5.19.

	BWR	s_1	h_1	Tether angle	γ	ε	H	T
Value	1,5	0,35	0,7	50	-0,06	0,05	0,08	1,2
Increase with 50%	2,25	0,525	1,05	75	-0,09	0,075	0,12	1,8
Positive motions								
Roll displacement	-52,7	-57,9	54,9	-59,5	-5,7	-32,8	33,4	-42,2
Roll velocity	-54,5	-52,4	24,1	-71,1	-4,7	-13,7	36,1	-56,3
Roll acceleration	-38,1	-55,2	15,8	-77,7	-4,6	-6,6	56,3	-61,1
Sway displacement	-52,6	-57,9	54,9	89	12,9	-42,1	37,4	-42,2
Sway velocity	-54,5	-52,4	24,1	35,1	14,3	-25,7	36,1	-56,3
Sway acceleration	-38,1	-55,2	15,9	4,4	14,4	-19,6	56,3	-61,1
Negative motions								
Roll displacement	-48,6	-55,9	24,6	-70,1	-5,1	-19,2	31,5	-31,1
Roll velocity	-33,6	-60,8	46,7	-62,3	-3,7	-19,9	51,1	-38,8
Roll acceleration	-22,8	-37,4	51,3	-56,3	-4,9	4,6	27,4	-47,7
Sway displacement	-48,6	-55,9	24,6	39,6	13,8	-30,5	31,5	-31,1
Sway velocity	-33,6	-60,8	46,7	76,3	15,4	-31,1	51,1	-38,8
Sway acceleration	-22,8	-37,5	51,3	104,3	14	-9,9	27,4	-47,7
Tether forces								
Inner tether	41,2	-15,1	0,1	-19,6	-0,3	-0,7	17,5	-14,6
Outer tether	46,7	-12,6	1,2	-14,1	-0,1	1,1	15,9	-11,7

Increase with 100% | 100 | Decrease with 100% | -100

Figure 5.19: Sensitivity study on the output of the dynamic SFT model.

Globally three different outputs are generated by the model, the positive motions, negative motions and the tether forces. These outputs can be found in figure 5.19, in the first column. The top row shows the input parameters that is varied with during the sensitivity analysis. The value of the input parameters is increased with 50%. The increase or decrease of the output parameters is visualized by a color bar and a percentage. Red is an increase of the output, green is a decrease of the output.

<div style="text-align: right; font-size: 3em;">6</div>

Conclusion, discussion and recommendations

In this chapter the conclusion, discussion and recommendations of the research are presented. First the main research questions and their sub-questions are answered. Subsequently a discussion is provided in which the research assumptions and their consequences on the conclusion are given. After the discussion, recommendations are given.

6.1. Conclusions

The main research questions are composed of sub-questions. Before the main research questions can be answered, the sub-questions are discussed.

Sub questions

1 a) *What is an appropriate method to model the forces on a restrained submerged floating tunnel (SFT) in a wave-current environment?*

The forces on a restrained SFT due to waves are be modelled with a modified Morison formulation. In this formulation the classical Morison terms, Krylov force, hydrodynamic force and drag force, are modified. The Krylov force is computed with the undisturbed dynamic pressure field obtained from the undisturbed velocity potential function. Undisturbed dynamic pressures are integrated over the surface areas of the restrained SFT which makes it possible to compute not only the vertical and horizontal Krylov force, but also the Krylov moment. The hydrodynamic force and drag force are computed with a modified Morison equation in which the water velocity and water acceleration are averaged over the tunnel structure height and width by means of integration. The average water velocity and water acceleration is implemented in the classical Morison equation. Due to the integration of the water velocity and water acceleration, a line of action can be computed for both the vertical and horizontal hydrodynamic/drag force which makes it possible to obtain a rotational hydrodynamic/drag moment. This solution method has two large advantages compared to the classical Morison equation. The first advantage is the possibility to compute rotational moments, something which is not possible with the classical Morison equation. The second advantage is the applicability for short waves. For classical Morison, diffraction effects need to be taken into account for wave lengths shorter than five times the object dimension. The modified Morison formulation reduces the water velocity and water acceleration by averaging over the structure dimensions. In this way, a correction is made for the diffraction effects. It should be noted that the applicability for short waves is only valid in case of structures that are submerged at a depth of at least 1.5-2 times the structure height. The forces on a restrained SFT due to uniform current can be modelled with the drag force expression from the classical Morison equation. To correct for the wave current interaction, the hydrodynamic mass coefficients are adapted as function of the Keulegan-Carpenter number.

1 b) *What is the effect of surface wave pressures due to short waves?*
In case of short waves, the SFT structure is forced by an asymmetric load. This causes large wave moments on the tunnel body. Wave moments, in case of short waves, are very important to simulate the dynamic response of the SFT. Especially the roll motion is triggered by rotational wave forces. Neglecting the rotational wave forces would result in large errors for roll motion predictions.

1 c) *Is this method suitable for cases in which motion and position-change is relevant?*
The method to determine the forces on a restrained SFT, discussed in sub-question 1a, is suitable for cases in which motion and position-change is relevant. However there are some limitations. The motion of the tunnel body causes radiated waves which deform the incoming wave field. Because the forcing method on a restrained SFT does not include a radiated potential, wave field deformation due to motion can not be modelled. The wave field deformation is largest in case of large tunnel oscillations in a short period of time. These oscillations are caused by waves with a short wave length and a large wave height in combination with a dynamic SFT configuration that allows a lot of movement. In the latter case, the modified Morison formulation on a restrained SFT is not suitable to model the dynamic response of a SFT. In the event that at least one of the three factors (large wave height, short wave length or flexible structure) is not present, the modified Morison formulation on a restrained SFT is highly suitable for cases in which motion and position-change is relevant.

2 a) *How can fluid structure interaction between a wave-current environment and a moving SFT be modelled?*
To model the fluid structure interaction of a SFT in a wave-current environment, a dynamic SFT model is used which contains three modules that are briefly explained. The SFT motion in a wave-current environment is decoupled in two parts. The first describes the SFT restrained in a wave-current environment and is called the **wave force module**. The wave force module applies the modified Morison formulation explained in sub-question 1a. The second part describes the SFT oscillation in still water and is called the **dynamic module**. To model the oscillations in still water, a dynamic system is used. The dynamic system contains hydrodynamic damping and added mass terms to simulate the presence of the still water. The wave force module and the dynamic module are coupled by the **coupling module**. In the coupling module, the forces obtained from the wave force module are attached to the dynamic system in still water, described in the dynamic module. The full equation of motion (EOM) is solved numerically. With the dynamic SFT model, displacements, velocities, accelerations and tether forces can be predicted for a wide range of SFT tunnel configurations loaded by various wave-current conditions.

2 b) *What kind of dynamic system can be used to simulate the dynamic response of a SFT?*
The dynamic system that is used to simulate the dynamic response has one degree of freedom describing the coupled roll and sway of the tunnel in the cross sectional plane. The system can be simulated with a single degree of freedom (SDOF) system due to the assumption that the mooring tethers are rigid constrains. The degree of freedom is an rotation of the tunnel body around a fixed rotation point in space, located at the intersection of the two tether axes. The damping of the tunnel is composed of a rotational damping and translational damping. Because the water around the SFT body is accelerating with the body itself, an added mass term is used. The magnitude of the hydrodynamic coefficients is calibrated with free decay data from physical model experiments.

3 a) *Which structural parameters are dominating the dynamic response of the SFT structure?*
Of all structural model parameters, the buoyance to weight ratio (BWR), submergence depth, and tether angle have the largest impact on the dynamic response of the SFT structure. The anchorage depth has a moderate effect on the dynamic response of the SFT. The tether connection of the tunnel has less effect on the dynamic response compared to the already mentioned structural parameters.

3 b) *How do structural parameters influence the dynamic response of a SFT in terms of tunnel motions and tether forces.*
Before answering this sub-question, the definition of tunnel motions is defined. Tunnel motions take into account the roll displacement, roll velocity, roll acceleration, sway displacement, sway velocity and sway acceleration. A motion is called positive if the motion is in the same direction as the wave propagation. Negative motions are motions counter directed to the wave propagation.

The BWR increases the stiffness of the dynamic SFT system which causes a decrease in the roll motions and sway displacement. Due to the stiffness increase, sway accelerations and velocities become larger. The natural frequency of the SFT is increased by increasing the BWR, which makes it more sensitive to shorter waves. A logical result is the increase in tether forces. The increase in tether force is larger for the outer tether than for the inner tether. Increasing the BWR decreases the risk of snapping lines. Also the chance of tether fatigue is reduced by increasing the BWR.

A decrease in submergence depth increases all tunnel motions. The roll and sway tunnel motions become more sensitive to short waves. For the roll motion, the largest motions are expected for a very shallow submergence depth in combination with a wave length twice the width of the tunnel structure. A decrease in submergence depth also increases the tether forces. However this effect is relative small compared to the increase in tunnel motions. The decrease in submergence depth increases the risk of snapping lines. Also the chance of tether fatigue is increased by decreasing the submergence depth. The increase in motions and tether forces is a logical result because the tunnel is more affected by the waves at the water surface.

Configurations with large tether angles have the character to be very flexible and sway dominant while configurations with small tether angles are much more stiff and roll dominant. A moderate tether angle e.g. 50° has the tendency to be a combination of roll and sway. Tether forces for configurations with small tether angles are more sensitive to short wave lengths while tether forces for configurations with large tether angles are more sensitive to long waves. Configurations with small tether angles have a smaller risk for having snapping lines and tether fatigue compared to configurations with large tether angles.

Increasing the anchorage depth of the SFT increases all motions. The increase in tether force is almost negligible. For the positive motions, displacements have the largest increase in magnitude (approximately a factor 2 higher than the increase in velocities and accelerations). For the negative motions, the velocities and accelerations have the largest increase in magnitude (approximately a factor 2 higher than the increase in displacements). This is a remarkable effect.

Placing the tether connection sideways of the tunnel body causes smaller roll motions and larger sway motions. Lowering the tether connection with respect to the tunnel bottom is favorable for all tunnel motions. The manner of how the tether connection is orientated, with respect to the tunnel body, has small influence on the tether forces.

3 c) *How does this study contributes to the research field of SFT?*
This study gives a supplement to the classical Morison theory. Morison's theory is modified which makes it possible to compute rotational moments due to wave loading. Also the applicability to short waves is enlarged. A new dynamic schematization is developed which makes it possible to describe the dynamic response of a SFT as a SDOF system. The advantages of this dynamic schematization are the fast computational time and the convenience of physical interpretation. The results obtained from this research study can be used as a preliminary design tool. In an early design stage, motions and tether forces can be predicted. Also measures to reduce these motions and tether forces can be investigated using the dynamic SFT model. Design graphs to estimate the snap-taut transition and safety against tether fatigue are provided. It should be noted that this dynamic SFT model can not be used for detailed computations in later design stages.

Main research questions

1. **How can forces on a SFT in a wave-current environment be predicted?**
   The hydrodynamic force, due to waves and current, is computed for a restrained SFT based on a modified Morison formulation. Force determination on a restrained SFT gives the possibility to compute the hydrodynamic forces independent of the motion of a tunnel. This has high computational advantages and the complexity of the problem is reduced. The decoupling of the hydro dynamic forces and SFT tunnel motion is not valid in case of large tunnel oscillations in combination with high tunnel accelerations. In the latter case, wave field deformation due to the motion of the SFT is severe and radiated waves due to the motion of the structure can not be neglected. The wave-current forces on the restrained SFT are computed with a modified Morison formulation. This method is developed to compute rotational forces caused by short waves, something which is not possible with the classical Morison equation. Rotational moments are indispensable when it comes to modeling of roll motions. The modified Morison formulation does not take into account diffraction effects, the incoming wave field is thus not affected by the presence of the SFT structure.

2. **How can the dynamic response of a tethered supported SFT be modelled in a wave-current environment?**
   The dynamic response of a tethered supported SFT in a wave-current environment is modelled using a SDOF dynamic system. This SDOF dynamic system describes the SFT oscillation in still water. The hydrodynamic coefficients, added damping and added mass, are calibrated with free decay data obtained from physical model experiments. The advantages of this SDOF dynamic system are the fast computational time and the convenience of physical interpretation. The hydrodynamic forces, computed for a restrained SFT, are attached tot the SDOF dynamic system. The result is a dynamic SFT model which is able to describe the motions and tether forces of a tethered supported SFT loaded by waves and current.

3. **How can parameters be used to reduce the dynamic response of a tethered supported SFT in a wave-current environment?**
   The dynamic response contains two aspects which are the tether forces and tunnel motions. It is desirable to reduce the dynamic response in order to limit construction costs and improve drive safety. The BWR can be used to increase the stiffness of the SFT configuration which reduces the roll motions and sway displacement. Also the risk of line snapping is reduced. A negative additional aspect is the increase in tether forces and due to the stiffness increase, sway accelerations and velocities become larger. An increase in BWR could be a good solution in cases where the wave climate is dominated by long waves. Tether forces and tunnel motions can be reduced by increasing the submergence depth. Also the risk of snapping lines is reduced. Tunnel motions, especially the sway acceleration, becomes more sensitive to longer waves in case the submergence depth is increased. An increase in submergence depth increases the pressure on the tunnel body which causes higher construction costs. Apart from this, it is more difficult to achieve a high BWR because of the extra construction material that will be needed. A shallow anchorage depth is always more favorable than a large anchorage depth in terms of tunnel motions. The anchorage depth has almost no effect on the tether forces. Configurations with large tether angles tend to be sway dominant. These structures are sensitive to long waves. Configurations with small tether angles tend to be roll dominant. These structures are sensitive to short waves. The risk of snapping lines can be reduced by reducing the tether angle. It should be noted that decreasing the tether angle results in larger roll motions. Based on the wave climate in combination with the design criteria, a suitable tether angle can be found. The roll motion can be decreased by placing the tether connection sideways of the tunnel body. A sideways connection causes larger sway motions. The increase in sway motions is larger than the decrease in roll motions. All tunnel motions can be reduced by lowering the tether connection with respect to the bottom of the tunnel body. The lowering of the tether connection does not influence the tether forces.

6.2. Discussion

This section discusses the effect of the assumptions and simplifications that where made during this research thesis. This section also provides the influence of the assumptions and simplifications on the previously given conclusions. The points of discussion are ordered from most influential to almost negligible.

- No diffraction effects are taken into account. The wave field is not affected by the presence of the SFT body. In case of long waves, the diffraction effect can be neglected. However when waves become shorter with respect to the tunnel structure dimensions ($L/(2a) = 5$), diffraction need to be taken into account. It can clearly be observed in the validation that at a shallow submergence depth, wave force predictions are highly over predicted for short waves. The causes over predictions in tether forces and tunnel motions. Errors for submergence depths smaller than 1.5-2 times the tunnel height can be up to 30%. For a submergence depth of 1.5-2 times the tunnel height, the diffraction effect can be compensated by the modified Morison formulation. The wave structure interaction is small at larger submergence depths, reducing the diffraction effect. Closer to the still water surface, the wave structure interaction is large. Apart from diffraction effect, energy dissipation due to wave deformation and wave breaking is more severe close to the still water surface. These phenomena can not be modelled by the dynamic SFT model.

- The motion of the SFT in a wave-current environment is decoupled into a restrained SFT in a wave-current environment and a oscillating SFT in still water. Due to this assumption, it is not possible to include the effect of the tunnel motion on the wave field. Feedback effects can not be modeled and in case of large displacements in combination with high accelerations, prediction errors for the SFT motions and tether forces are made.

- Wave breaking due to a shallow anchored SFT is not taken into account. Breaking waves cause slamming forces on top of the tunnel structure. Slamming forces change the dynamic response of the SFT significantly. In the situation of large tunnel motions with high accelerations, wave breaking is enhanced, causing even larger prediction errors. For moderated tunnel motions, and submergence depths below 1.5-2 times the structure depth, this effect is not present. Even when the tunnel has a small submergence depth, model predictions are still acceptable.

- The dynamic SFT model is validated with data from physical model experiments. In these physical model experiments, some physical effects occurred which are not included in the dynamic SFT model. These effects could lead to differences between the validation data and the dynamic SFT model. A short summation is given.

  - In the physical model set-up, tethers are connected to pulleys and measuring equipment. Due to the pulleys and measuring equipment, secondary effects occur at large submergence depths. The physical model that has been created is fundamentally different than the model that is used in the dynamic SFT model. This results in large errors in the validation process. A solution for this problem is given in the recommendations,

  - Seen from the top, the wave is affected by the presence of the side walls of the flume. The wave crest is deformed into a Gaussian shape in case of short waves. In case of long waves, this effect is small. The dynamic SFT model computes wave forces for waves that are constant in profile over the tunnel length, not taking into account any wave deformation due to side walls. This could lead to errors in the validation process. It should be noted that this a property of the physical flume experiment which can not be changed.

  - In the dynamic SFT model, the tethers are simplified as rigid constrains. From video's of the physical model experiments, it can be observed that the tethers do allow some extra motion. Due to the measuring equipment, some extension of the tether is allowed. Due to this extension, small heave motions and second order vibrations are possible. Because of the rigid constrains in the dynamic SFT model, these effects can not be taken into account. This could contribute to validation errors, however the effect is very small and can be neglected.

  - During the physical model experiments, water can flow along the sides of the tunnel body. In reality and also in the dynamic SFT model, flow can not pass the sides of the SFT. Flow passing shall always be present in physical model experiments and can not be avoided. Besides that, the

effect is inevitable. The flow passing effect is small and because the flow passing effect is present for all physical model experiments, is can be neglected.

- Damping and added mass coefficients are assumed to be constant in time and frequency independent. However, the magnitude of the added damping and added mass coefficients does depend on the frequency (Vugts, 1971). The value of the damping and added mass coefficients is obtained from free decay calibrations. During free decay, the tunnel moves with the eigenfrequency. In case the structure has a motion with a frequency far away from the eigenfrequency of the system, the damping is overestimated. This leads to a under prediction of motions. To obtain a higher accuracy in the motion prediction, added damping and added mass coefficients should include frequency dependency.

- The effect of flow along the tethers is not included in the dynamic SFT model. In the validation data from the physical model experiments, second order effects can be seen. The effect of flow along the tethers could contribute to these second order effects. The effect of flow along the tethers is neglectable because of the small size of the tethers in the physical model experiments. The tethers are made from a very thin nylon rope which have a small surface area.

6.3. Recommendations

In this section, two types of recommendations are provided. The first considers recommendations to improve the dynamic SFT model which is used in this thesis to simulate the dynamic response of the SFT. Subsequently, recommendations for future research on the dynamics of the SFT are given. These recommendations that are given are in line with the research that has been done in this thesis.

6.3.1. Recommendations to improve the dynamic SFT model

- To include the diffraction effect in the dynamic SFT model, the wave force module should be improved. To improve the wave force prediction, a different forcing model should be used. A good alternative is to solve the potential field based on a incoming potential and diffracting potential. The solved potential can be inserted into the linearized Bernoulli equation from which the pressures, included diffraction effects, can be obtained. From the pressures, the wave forces can be computed. This would improve the wave force prediction for wave lengths smaller than five times the structure length.

- To include the feedback effects in the dynamic SFT model, the tunnel dynamic system and force determination should be combined into one system. In this way, feedback effects can be modeled and no added damping or added mass terms have to be used. Possible methods to solve the fluid-structure interaction are potential flow theory and Computational Fluid Dynamics (CFD) modeling. Solving the velocity potential which contains a incoming potential, diffracted potential and a radiated potential involves complicated mathematics. The shape and dynamic system need to be processed in the boundary conditions to solve the velocity potential. This makes that the potential flow method is limited to the simple shapes and simple dynamic models and thus not very suitable for the dynamic system that is used in this thesis. CFD modelling is a more suitable forcing method to combine with the dynamic system of this thesis. With CFD models, higher order stoke waves, wave deformation and breaking waves can be simulated.

- The physical model experiments on which the dynamic model is validated contains physical effects that are not included in the dynamic SFT model. A short summation to improve the validation data is given.

  – The wave deformation into a Gaussian shape, due to friction at the flume walls, can be avoided by widening the flume. A longer stiff tunnel segment loaded by long crested waves reduces the effect of wave deformation. The effect of wave deformation due to friction at the flume walls will still be present but the total contribution to errors will be reduced. The wave deformation can also be corrected with correction parameters which depend on the wave length. It should be noted that these correction parameters are flume dependent. A wider flume also reduces the effect of flow along the tunnel sides. Flow along the tunnel sides will still be presents but the total contribution to errors will be reduced. Both phenomena are visualized in figure 6.1a.

  – Secondary effects due to pulleys and measuring techniques can be reduced by placing measuring equipment inside the tunnel element. In this way, no measuring tethers and pulleys have to be

used. A possible model set-up is presented in figure 6.1b. The water can not flow into the SFT because the air inside is trapped.
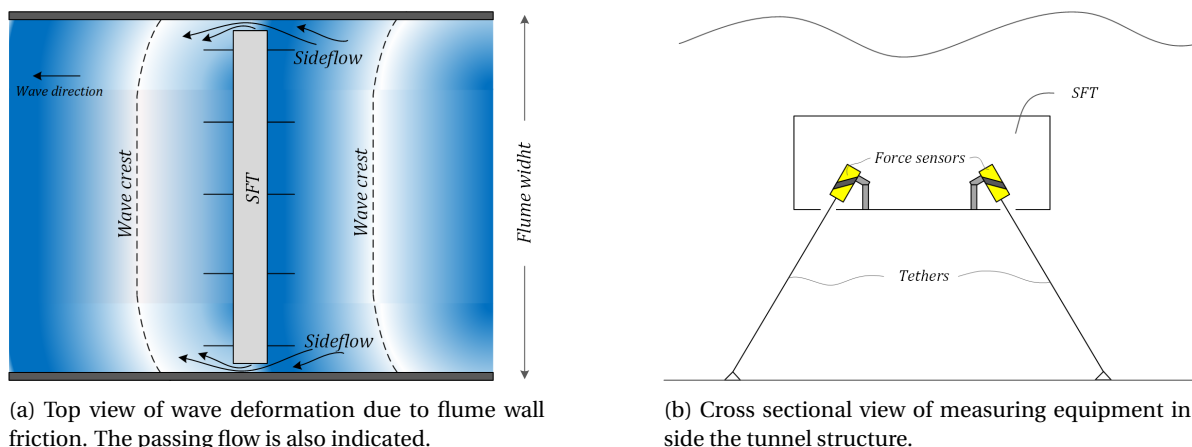
(a) Top view of wave deformation due to flume wall friction. The passing flow is also indicated.

(b) Cross sectional view of measuring equipment inside the tunnel structure.

Figure 6.1: Adaptations on physical model experiments to improve the validation of the dynamic SFT model.

6.3.2. Recommendations for future research on the dynamics of the SFT

- One of the first questions that arises is the applicability of this dynamic SFT model in case of large anchorage depths. The dynamic SFT model used in this thesis has simplified the tethers as rigid weightless constrains. When the length of tethers increases, the self weight and axial stiffness must be taken into account. The flexibility of the SFT will increase for large anchorage depths, something which is schematized in figure 6.2a. What is the limitation of this dynamic SFT model? A rough estimation of the maximal anchorage depth has been made in this thesis. For anchorage depths larger than 10 times the SFT width, the dynamic SFT model can not be used. This rough estimation is not validated! At the moment there is no validation data available a for deep anchored SFT.

- The tethered supported SFT is ideally suited for long-span deep water crossings. As mentioned in the previous bullet point, deep anchored tunnels have much more freedom than shallow anchored tunnels. Once the dynamic SFT model of this thesis is not valid because the anchorage depth is too large, a new dynamic model should be developed. This model needs to take into account the self weight and the axial stiffness of the tethers. Roll heave and sway can act independently of each other which requires a multi degrees of freedom (MDOF) dynamic system.

- From the parametric study in this thesis, it has been proven that increasing the anchorage depth increases all SFT motions. The extra flexibility due to long tethers gives an extra contribution to the increase in SFT motions. Measures to reduce the dynamic response need to be explored. One should think of vertical tethers to minimize the heave and roll motions, schematized in figure 6.2b. Other possibilities are hanging weights on the tethers or add damping systems.

- In this thesis, a simple wave current interaction model has been used. No parametric study has been executed of the influence of current on the dynamic response of the SFT. A more sophisticated wave current interaction model should be developed which can be used to simulate the dynamic response of a tethered supported SFT.

- The forcing on the SFT can be expanded. This research only takes into account permanent loads and wave-current loads. Service loads (rail/road traffic, loads during construction) and exceptional loads (earthquakes, fire, explosions, flood, collisions, encrustations due to underwater organisms) should also be investigated.

(a) Deep anchored SFT with two angular flexible tethers.

(b) Deep anchored SFT with two angular flexible tethers, corrected with two vertical tethers.
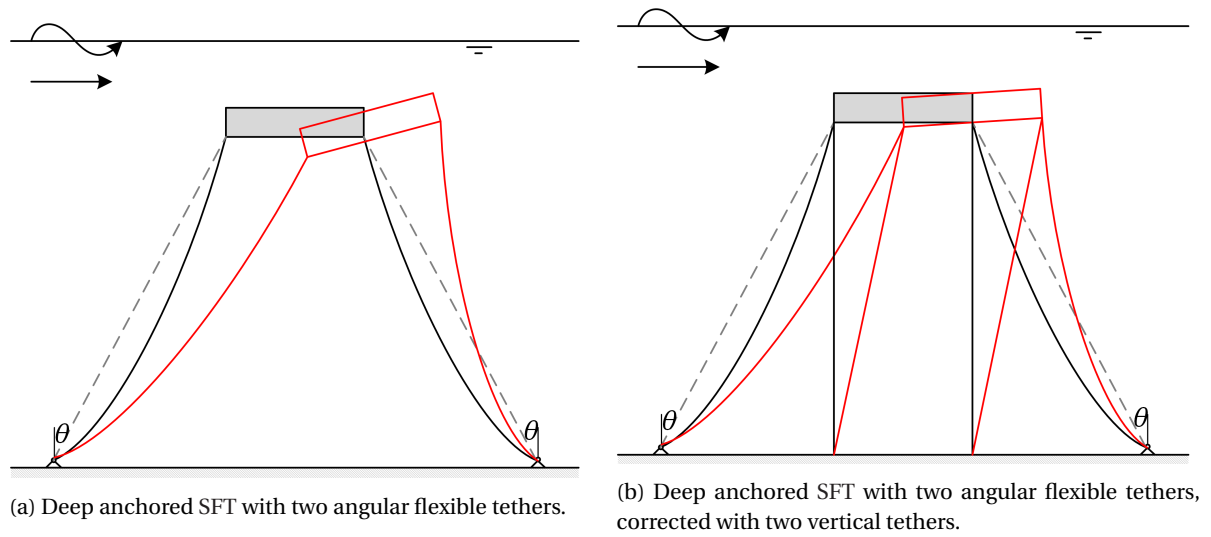
Figure 6.2: Deep anchored SFT tether configurations in which the flexibility of the tethers is taken into account.

References

Airy, G. (1841). Tides and waves. *Encyclopaedia Metropolitana.*

Bai, K. (1975). Diffraction of oblique waves by an infinite cylinder. *Journal of Fluid Mechanics 68, 513-535.*

Batchelor, G. (1973). *An introduction to fluid dynamics.* Cambridge University Press.

Boyce, W. E. & DiPrima, R. C. (2012). *Elementary differential equations and boundary value problems.* John Wiley & Sons; 10th International student edition.

Chen, H. & Yu, K. (2008). Cfd simulations of wave-current-body interactions including greenwater and wet deck slamming. *Computers and Fluids.*

Dong, R. (1978). *Effective mass and damping of submerged structures.* Lawrence Livermore Laboratory.

Drost, L. C. (2019). *The submerged floating tunnel, an experimental study on the hydrodynamic forces and kinematics of a submerged rectangular cylinder in a wave-current environment.* Delft University of Technology.

Faggiano, B., Landolfo, R. & Mazzolani, F. (2005). The sft: An innovative solution for waterway strait crossings. *IABSE symposium Lisbon.*

Faltinsen, O. M. (1990). *Sea loads on ships and offshore structures.* Cambridge university press.

Holthuijsen, L. H. (2007). *Waves in oceanic and coastal waters.* Cambridge University.

Journée, J. & Massie, W. (2001). *Offshore hydromechanics.* Delft University of Technology.

Journée, J. & Pinkster, J. (2002). *Introduction in ship hydromechanics* (draft ed.). Delft University of Technology. (Lecture MT519)

Kantardgi, I. (1995). Effect of depth current profile on wave parameters. *Coastal engineering.*

Kantardgi, I., Makarova, I. & Pelinovsky, E. (1989). Wave transformation by depth linear velocity shear current. *Oceanology XXIX.*

K.H.Frank, J. . (1991). Cyclic fatigue life of cables. *Engineering fracture mechanics.*

Korane, K. (2017). *Hydraulic wave-energy system operates underwater for over a year.* Retrieved from `https://www.fluidpowerworld.com/hydraulic-wave-energy-system-operates-underwater-year/`

Kunisu, H. (2010). Evaluation of wave force acting on submerged floating tuennels. *Procedia |Engineering.*

Lotsberg, I. (2016). *Fatigue design of marine structures.* Cambridge University Press.

Lu, W., Ge, F., Wang, L., Wu, X. & Hong, Y. (2011). On the slack phenomena and snap force in tethers of submerged floating tunnels under wave conditions. *Marine Structures.*

Mandara, A., Russo, E., Faggiano, B. & Mazzolani, F. (2016). Analysis of fluid -structure interaction for a submerged floating tunnel. *Procedia Engineering.*

Metrikine, A. (2006). *Dynamics, slender structures and an introduction to continuum mechanics.* Delft University of Technology.

Muhammad, N., Ullah, Z., Park, M. & Choi, D. (2017). The role of cable stiffness in the dynamic behaviours of submerged floating tunnel. *MATEC Web of Conferences.*

Méhauté, B. L. (1969). *An introduction to hydrodynamics and water waves.* Us Department of Commerce Washington DC.

OBrien, M., Johnson, J., Schaaf, S. & Morison, J. (1950). The force exerted by surface wave on piles. *Petol. Trans.*

Oikou, N. (2014). Vortex-induced vibration of a slender single-span cylinder. *Delft University of Technology, the Netherlands.*

Pan, Y., Zhang, H. & Zhou, Q. (2012). Numerical prediction of submarine hydrodynamic coefficients using cfd simulation. *Journal of Hydrodynamics.*

Patel, M. & Witz, J. (2013). Compliant offsshore structures. *Elsevier.*

Peng, W., Lee, K., Shin, S. & Mizutani, N. (2013). Numerical simulation of interactions between water waves and inclined-moored submerged floating breakwaters. *Coastal engineering.*

Peregrine, D. (1976). Interaction of water waves and current. *Adc. Appl. Math.*

Peters, D. (1993). Tuiconstructies, constructief gedrag en optimalisering. *TNO-Prins Maurits Laboratorium, Rijswijk.*

Remsheth, S., Leira, B., Ronnquist, A. & Udahl, G. (2005). Dynamic response and fluid structure interaction of submerged floating tunnels. *WIT Transactions on The Built Environment.*

Reniers, A. & Tissier, M. (2018). *Lecture notes ocean waves, linear wave theory.* Delft university of technology.

Rijnsdorp, D., Hansen, J. & Lowe, R. (2018). Simulating the wave-induced response of a submerged wave-energy converter using a non-hydrostatic wave-ow model. *Coastal Engineering.*

Savenije, L., Ashuri, T., van Bussel, G. & Staerdahl, J. (2010). Dynamic modeling of a spar-type floating offshore wind turbine. *EWEC 2010 Scientific Proceedings.*

Senan, N. A. F. (n.d.). *ode45.* University of California at Berkeley.

Sumer, B. M. & Fredsoe, J. (1997). *Hydrodynamics around cylindrical structures.* World Scientific Publishing Co. Pte. Ltd.

Umar, A. & Datta, T. (2002). Nonlinear response of a moored buoy. *Ocean Engineering.*

Ursell, F. (1948). On the heaving motin of a circular cylinder on the surface of a fluid. *University Manchester, department of Mathematics.*

van Dalen, A. M. . K. (2018). *Lecture notes dynamics of systems.* Delft university of technology.

Venugopal, V., Varyani, K. & Westlake, P. (2008). Drag and inertia coefficients for horizontally submerged rectangular cylinders in waves and currents. *University of Edinburgh.*

Vugts, J. (1971). *The hydrodynamic forces and ship motions in oblique waves.* Nederlands scheepsstudie-centrum nederlandse organisatie voor toegepast-Natuurwetenschappelijk onderzoek.

Weoncheol, K. & K.Jun-Dong. (2015). Simplified formulas of heave added mass coefficients at high frequency for various two-dimensional bodies in a finite water depth. *Department of Naval Architecture and Ocean Engineering, Inha University, Incheon, Korea.*

Widnall, S. (2009). *Lecture notes energy methods: Lagrange's equations.* MIT.

X.Chen. (n.d.). Sft load effect assessment-2d wave flume experiment interpretation report (part i). *internal report (to be published).*

Xiang, Y., Chen, Z., Yang, Y., Lin, H. & Zhu, S. (2018). Dynamic response analysis for submerged floating tunnel with anchor-cables subjected to sudden cable breakage. *Marine Structures.*

Xiang, Y. & Yang, Y. (2017). Spatial dynamic response of submerged floating tunnel under impact load. *Marine Structures.*

Yan, H., Luo, Y. & Yu, J. (2016). Dynamic response of submerged floating tunnel in the flow field. *Procedia Engineering*.

Zheng, Y., Liu, P., Shen, Y., Wu, B. & Sheng, S. (2006). On the radiation and diffraction of linear water waves by an infinitely long rectangular structure submerged in oblique seas. *Ocean Engineering*.

A

Wave force module

In this appendix, the wave-current forcing on the restrained submerged floating tunnel (SFT) is elaborated. The wave forcing consist of the Krylov forcing, hydrodynamic forcing, drag forcing and current forcing. All are elaborated in separate sections.

A.1. Parameter definitions
In figure A.1, the parameters which are used in the wave force module, are presented. The restrained tunnel body is attacked by a normal incident linear wave train of wave height H and wave period T. The tunnel is forced by a uniform current with velocity u_c. A reference system is chosen at the water surface.

Figure A.1: Parameter definitions in wave force module.

The wave loading creates a horizontal force $F_{w,x}$, vertical force $F_{w,z}$ and moment $M_{w,y}$ with respect to the centre of the SFT. This centre is indicated with CG. The wave forces and their components are presented in eq A.1. The three equations also show which theory is used to determine each force component.

$$
\begin{aligned}
F_{w,x} &= F_{Krylov,x} + F_{drag,x} + F_{hydrod,x} \\
F_{w,z} &= F_{Krylov,z} + F_{drag,z} + F_{hydrod,z} \\
M_{w,y} &= M_{Krylov,y} + M_{drag,y} + M_{hydrod,y}
\end{aligned}
$$

$$\underbrace{\phantom{F_{Krylov,x}}}_{\text{Velocity potential}} \qquad \underbrace{\phantom{F_{drag,x} + F_{hydrod,x}}}_{\text{Modified Morison}}$$

(A.1)

101

As can be seen in eq A.1, each wave force is described by three force components. These are; Krylov force, drag force and hydrodynamic force. The force components of equation A.1 are elaborated in separate sections. After the wave force components are explained, the calibration of the inertia coefficients is elaborated. Finally the current forcing is treated.

A.2. Krylov forcing

In theory, the Krylov force is caused by a pressure gradient in an undisturbed flow. The Krylov force can thus be expressed as undisturbed pressures integrated over each domain of the tunnel body. An impression of the dynamic pressure in the total domain is given in figure A.2. In this figure, the highest dynamic pressure is indicated with red and the lowest dynamic pressure is indicated with blue.
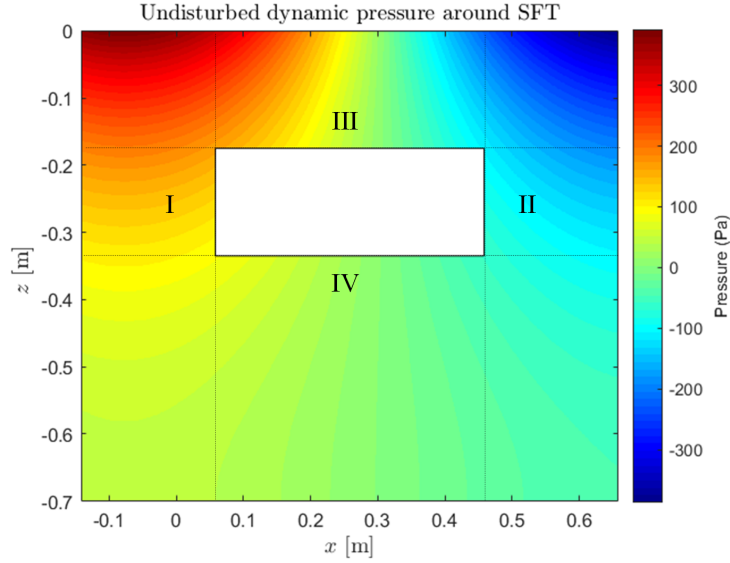
Figure A.2: Undisturbed dynamic pressure around SFT. Four different pressure sections are indicated. $T = 1.0s, H = 0.08m, s1 = 0.175m, t = 1.2s$.

The lowest dynamic pressures are found below the trough of the wave and the highest pressures are found at the crest of the wave. It can be observed that the tunnel structure dimensions are relative large compared to the wave length. The tunnel pressures left of the tunnel (section I) are larger than the pressures at the right side of the tunnel (section II). Also the pressures on top of the tunnel (section III) are smaller than the pressures at the bottom of the tunnel (section IV). The undisturbed dynamic pressure and its derivation can be found in the literature study section 2.1. Integrating the pressures on each section normal to the wet surface will give the forces at each side of the SFT. The forces of each section are elaborated below:

$$F_{Krylov,I} = \iint_{dS} P_I \vec{n} \, dz = \int_{-d_1}^{-s_1} \rho g \frac{H}{2} \frac{\cosh[k(d+z)]}{\cosh(kd)} \sin(\omega t - kx) \Big|_{x=s_0-\gamma} \, dz \tag{A.2}$$

$$F_{Krylov,II} = \iint_{dS} P_{II} \vec{n} \, dz = -\int_{-d_1}^{-s_1} \rho g \frac{H}{2} \frac{\cosh[k(d+z)]}{\cosh(kd)} \sin(\omega t - kx) \Big|_{x=s_0-\gamma+2a} \, dz \tag{A.3}$$

$$F_{Krylov,III} = \iint_{dS} P_{III} \vec{n} \, dx = -\int_{s_0-\gamma}^{s_0-\gamma+2a} \rho g \frac{H}{2} \frac{\cosh[k(d+z)]}{\cosh(kd)} \Big|_{z=-s1} \sin(\omega t - kx) \, dx \tag{A.4}$$

$$F_{Krylov,IV} = \iint_{dS} P_{IV} \vec{n} \, dx = \int_{s_0-\gamma}^{s_0-\gamma+2a} \rho g \frac{H}{2} \frac{\cosh[k(d+z)]}{\cosh(kd)} \Big|_{z=-d1} \sin(\omega t - kx) \, dx \tag{A.5}$$

Combining the sectional forces gives the resultant horizontal and vertical Krylov force described in eq A.6 and eq A.7.

$$F_{Krylov,x} = F_{Krylov,I} + F_{Krylov,II} \tag{A.6}$$

$$F_{Krylov,z} = F_{Krylov,III} + F_{Krylov,IV} \tag{A.7}$$

The rotational moment due to the undisturbed dynamic pressure with respect to the centre fo gravity of the SFT is computed with the simply supported beam model. The rotational moment due to the undisturbed dynamic pressure consist of two components. The first component is the rotational moment caused by the vertical undisturbed pressure and the second component is the rotational moment caused by the horizontal undisturbed pressure. For both components, a simply supported beam model is set-up. This can be seen in figure A.3.

Undisturbed pressure
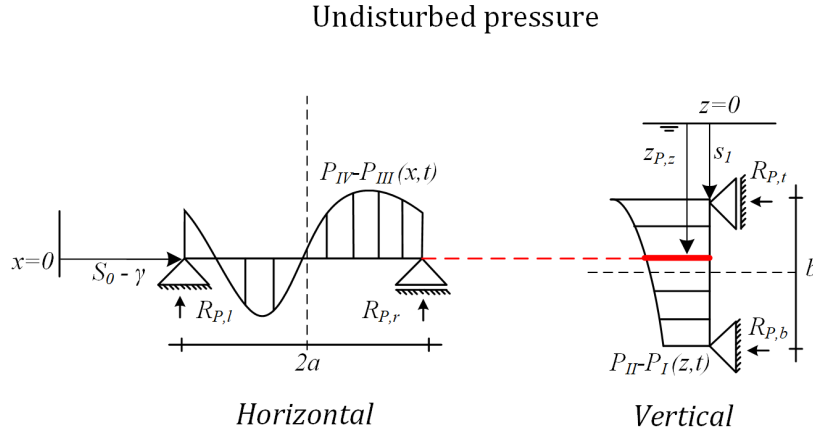
Figure A.3: Undisturbed pressure schematised on simply supported beams

First the support reactions $R_{P,l}, R_{P,r}, R_{P,t}$ and $R_{P,b}$ are computed. These support reaction forces are the resultants of the dynamic pressure. The support reactions are multiplied with their own leaver arm with respect to the CG of the SFT body. For the horizontal beam models this is a and for the vertical beam model this is $\frac{1}{2}b$. The rotational moments obtained from both beam models are summed and the Krylov moment is obtained. The expressions for the Krylov moment are expressed in eq A.8. The dynamic pressure is described by an exponential decay function with respect to the depth. The resultant horizontal force is indicated with red in figure A.3 and is independent of time.

$$M_{Krylov,y} = a \times \left[R_{P,l} - R_{P,r}\right] + \frac{1}{2}b \times \left[R_{P,b} - R_{P,t}\right] \tag{A.8}$$

in which:

$$R_{P,r} = \frac{1}{2a} \int_{s_0 - \gamma}^{s_0 - \gamma + 2a} \left[P_{IV} \times (x - s_0 + \gamma) - P_{III} \times (x - s_0 + \gamma)\right] dx \tag{A.9}$$

$$R_{P,l} = F_{Krylov,IV} + F_{Krylov,III} - R_{P,r} \tag{A.10}$$

$$R_{P,b} = \frac{1}{b} \int_{-s_1}^{-d_1} \left[P_{II} \times (z + d_1) - P_I \times (z + d_1)\right] dz \tag{A.11}$$

$$R_{P,t} = F_{Krylov,I} + F_{Krylov,II} - R_{P,b} \tag{A.12}$$

A.3. Hydrodynamic forcing

The hydrodynamic forcing is proportional to the acceleration of flow along the object. The undisturbed water acceleration in the domain of the SFT is presented in figure A.4.
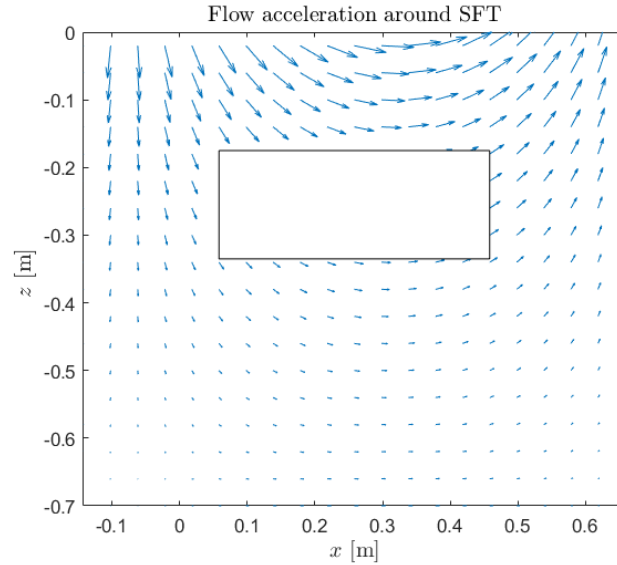
Figure A.4: Undisturbed water acceleration around SFT. $T = 1.0s, H = 0.08m, s1 = 0.175m, t = 1.2s$.

It can be observed that the accelerating flow pattern is far from uniform because the wave length is small compared to the object. The water particles accelerate in orbital motions. Because the structure is large compared to the wave length, it is not correct to compute the acceleration of the water in the centre of the tunnel and implement it in the Morison equation to compute the hydrodynamic force. The hydrodynamic forcing is determined with an modified Morison formulation which takes into account the size of the SFT with respect to the wave length.

The acceleration of water particles is separated in a horizontal and vertical component to compute the vertical and horizontal hydrodynamic force on the submerged object. Both x and z direction are shown in figure A.5.
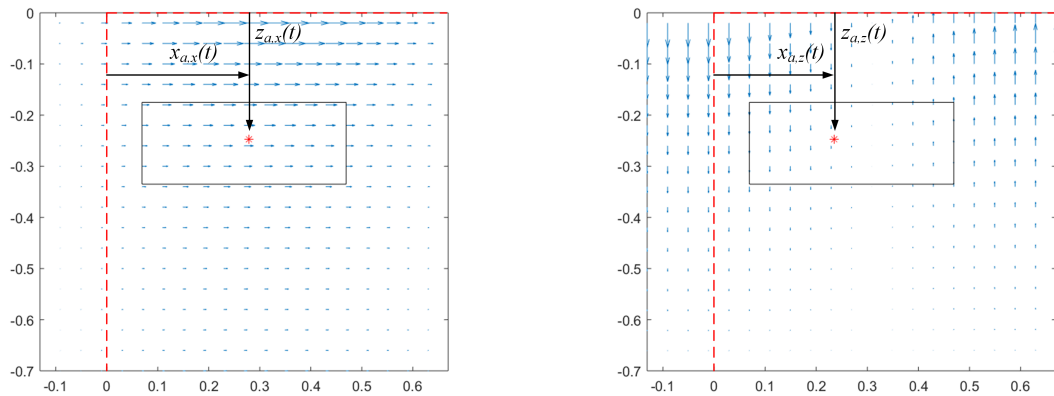
(a) Water acceleration in x direction. In red, the resultant in x, z direction for horizontal acceleration.

(b) Water acceleration in z direction. In red, the resultant in x, z direction for vertical acceleration.

Figure A.5: Horizontal and vertical acceleration due to harmonic wave in domain. $T = 1.0s, H = 0.08m, s1 = 0.175m, t = 1.2s$.

In red, the resultant in x, z direction is plotted for both the horizontal and vertical acceleration. This point represents the centre of gravity of the accelerating flow in time, which implies that this resultant point is moving in time. The location of the resultant for the horizontal and vertical accelerating flow can be computed

with eq A.13 - A.16. Eq A.13 describes the x location of the horizontal resultant accelerating flow and eq A.14 describes the z location of the horizontal resultant accelerating flow. For the vertical acceleration eq A.15 is used for the x location and eq A.16 is used for the z location.

$$x_{a,x}(t) = \frac{1}{\int_{s_0-\gamma}^{s_0-\gamma+2a} |\frac{\partial u_x}{\partial t}| \, dx} \int_{s_0-\gamma}^{s_0-\gamma+2a} |\frac{\partial u_x}{\partial t}| x \, dx \tag{A.13}$$

$$z_{a,x} = \frac{1}{\int_{-d1}^{-s1} |\frac{\partial u_x}{\partial t}| \, dz} \int_{-d1}^{-s1} |\frac{\partial u_x}{\partial t}| z \, dz \tag{A.14}$$

$$x_{a,z}(t) = \frac{1}{\int_{s_0-\gamma}^{s_0-\gamma+2a} |\frac{\partial u_z}{\partial t}| \, dx} \int_{s_0-\gamma}^{s_0-\gamma+2a} |\frac{\partial u_z}{\partial t}| x \, dx \tag{A.15}$$

$$z_{a,z} = \frac{1}{\int_{-d1}^{-s1} |\frac{\partial u_z}{\partial t}| \, dz} \int_{-d1}^{-s1} |\frac{\partial u_z}{\partial t}| z \, dz \tag{A.16}$$

The vertical position of the resultant force will not change in time because this is not a harmonic time dependent function but an exponentially decaying function which shape is independent of time. The horizontal position for the vertical and horizontal acceleration resultant will change in time as mentioned before. This movement is plotted in figure A.6.
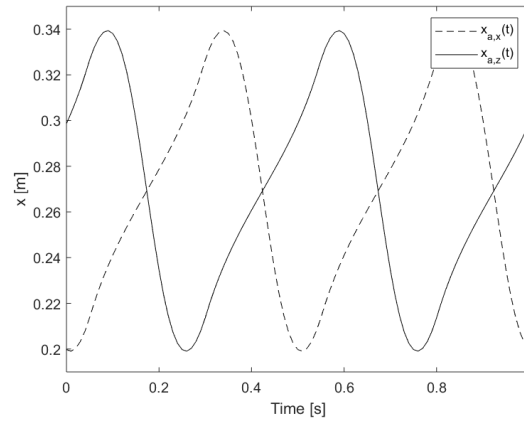
Figure A.6: Horizontal position of the horizontal and vertical resultant of the water acceleration due to harmonic wave in domain. $T = 1.0s$, $H = 0.08m$, $s1 = 0.175m$

The figure clearly shows that for a time interval of one wave period, the horizontal movement makes two cycles. The 'resultant point' will move along with the wave that passes by from left to right. During one wave period, a negative and positive directed accelerating flow passes by the SFT which creates two horizontal cycles in one wave period. The x and z location of the resultant point for water acceleration is used to compute the resultant acceleration for the horizontal and vertical direction. For the horizontal hydrodynamic force, the acceleration should be integrated over the height of the object at the horizontal location $x_{a,x}(t)$, eq A.17. For the vertical hydrodynamic force, the acceleration should be integrated over the width of the object at the vertical location $z_{a,z}$, eq A.18.

$$\overline{\frac{\partial u_x}{\partial t}} = \frac{1}{b} \int_{-d1}^{-s1} \frac{\partial u_x}{\partial t} \bigg|_{x=x_{a,x}(t)} dz \tag{A.17}$$

$$\overline{\frac{\partial u_z}{\partial t}} = \frac{1}{2a} \int_{s_0-\gamma}^{s_0-\gamma+2a} \frac{\partial u_z}{\partial t} \bigg|_{z=z_{z,z}(t)} dx \tag{A.18}$$

Now that the resultant accelerations in the x,z plane are computed in time, it is possible to determine the hydrodynamic force according to eq A.19 and eq A.20.

$$F_{hydrod,x} = \rho A_x C_{mx} \overline{\frac{\partial u_x}{\partial t}} \tag{A.19}$$

$$F_{hydrod,z} = \rho A_z C_{mz} \overline{\frac{\partial u_z}{\partial t}} \tag{A.20}$$

For the horizontal hydrodynamic Morison coefficient a value of $C_{mx} = 1.35$ is used. For the vertical hydrodynamic Morison coefficient a value of $C_{mz} = 1.45$ is used. The calibration of the hydrodynamic Morison coefficients C_{mx} and C_{mz} can be found in appendix A.5. A detailed elaboration of the hydrodynamic force components can be found in appendix A.3.

For the classical Morison equation, the accelerations at the centre of the structure are used to determine the hydrodynamic force on the structure because the structure is small compared to the wave length, In case the structure becomes large with respect to the wave length, an average acceleration is used. The ratio between the average acceleration and the acceleration at the centre of the structure can be seen as a reduction coefficient. This is illustrated in figure A.7.
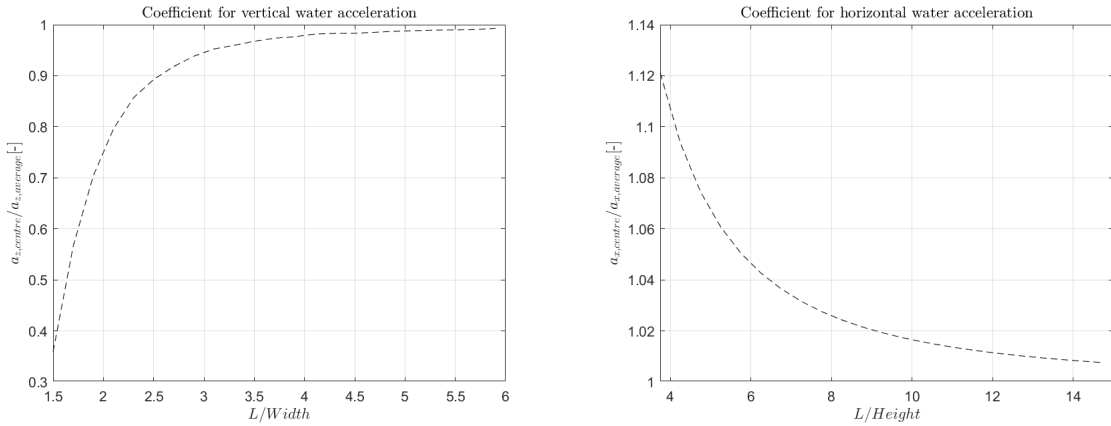
(a) Coefficient for the vertical water acceleration as function of the wave length structure length ratio.

(b) Coefficient for the horizontal water acceleration as function of the wave length structure height ratio.

Figure A.7: Correction coefficients for the vertical and horizontal water acceleration for short waves. These curves are independent on the submerged depth and the wave height and can be used to correct for short waves.

For the vertical water acceleration coefficient it can be observed that with a ratio of $L/(2a)$ of around 5, the ratio approaches 1. This means that the structure is relative small compared to the wave length. In case the wave becomes shorter, the object size cant be neglected. The water acceleration, taken at the centre of the object, should be multiplied with the acceleration coefficient. For very short waves, hardly any acceleration takes place. The horizontal coefficient works the other way around. In case of short waves, the coefficient becomes larger than 1. If the structure height is large with respect to the wave length, the centre of gravity of the horizontal accelerating flow is higher located in the water column. This means higher averaged accelerations and thus an increase in the coefficient. However the influence of this coefficient is small (maximal 10 %).

The hydrodynamic moment is determined based on the two hydrodynamic forces from eq A.19 and A.20. The hydrodynamic moment which is caused by the horizontal hydrodynamic force is presented in eq A.21.

$$M_{hydrod,\overrightarrow{x}} = F_{hydrod,x} \times \left[z_{a,x}(t) - s_0 - \frac{1}{2}b \right] \tag{A.21}$$

The moment due to vertical wave forces is more difficult to determine because of the limitations of the Morison equation. The moment due to the hydrodynamic force is maximum when the node of the wave is at the same horizontal location as the metric centre of the SFT. This situation is illustrated in figure A.8.

Computing this rotational moment due to inertia is limited by Morison's equation. The resultant accelerating flow in the vertical direction will become zero because the acceleration left of the metric centre will be the same as the acceleration right of the metric centre. According to Morison, this will give a zero vertical force, and thus no moment will occur. This can not be the case because the moment due inertia should be maximal with the situation illustrated in figure A.8. The rotational moment due to the vertical inertia can not be neglected and thus an alternative solution needs to be found.

This alternative solution is found by introducing fictive ratio parameters $\rho_{a,r}$ and $\rho_{a,l}$. These ratio parameters are determined with the simply supported beam model, presented in figure A.9.
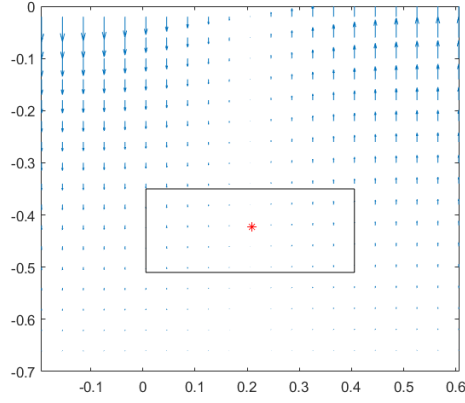
Figure A.8: Acceleration of water particles due to harmonic wave $T = 1.0s, H = 0.16m, s1 = 0.35m$ at $t = 1.13$
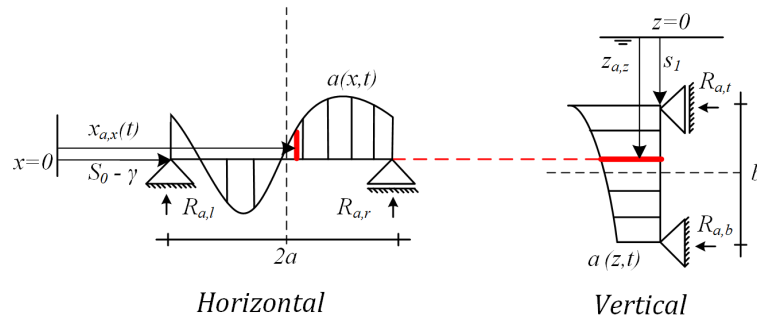
Figure A.9: Flow acceleration profile schematised on simply supported beams

The load on the simply supported beam is described by the vertical acceleration at depth $z_{a,z}$. In the same way as the Krylov forcing, reaction forces can be determined. These acceleration reaction forces are elaborated in eq A.22 and A.23.

$$R_{a,r} = \frac{1}{2a} \int_{s_0-\gamma}^{s_0-\gamma+2a} \frac{\partial u_z}{\partial t} \times (x - s_0 + \gamma) dx \tag{A.22}$$

$$R_{a,l} = \int_{s_0-\gamma}^{s_0-\gamma+2a} \frac{\partial u_z}{\partial t} dx - R_{a,r} \tag{A.23}$$

The acceleration reaction forces can be translated to a percentile of the total acceleration, which is elaborated in eq A.24 and in eq A.25.

$$\rho_{a,r} = \frac{R_{a,r}}{R_{a,r} + R_{a,l}} \tag{A.24}$$

$$\rho_{a,l} = \frac{R_{a,l}}{R_{a,r} + R_{a,l}} \tag{A.25}$$

Multiplying the percentile of the total acceleration with the resultant vertical hydrodynamic force gives the hydrodynamic force at the right and left support. The rotational moment due to the vertical hydrodynamic force is elaborated in eq A.26.

$$M_{hydrod,\vec{z}} = a \times \rho_{a,r} F_{hydro,z} - a \times \rho_{a,l} F_{hydrod,z} \tag{A.26}$$

In figure A.10, the rotational moment due to the vertical accelerating flow is plotted. The top figure shows the vertical hydrodynamic force and the ratio parameters. The bottom graph shows the vertical hydrodynamic force and the hydrodynamic rotational moment due to this vertical hydrodynamic force.
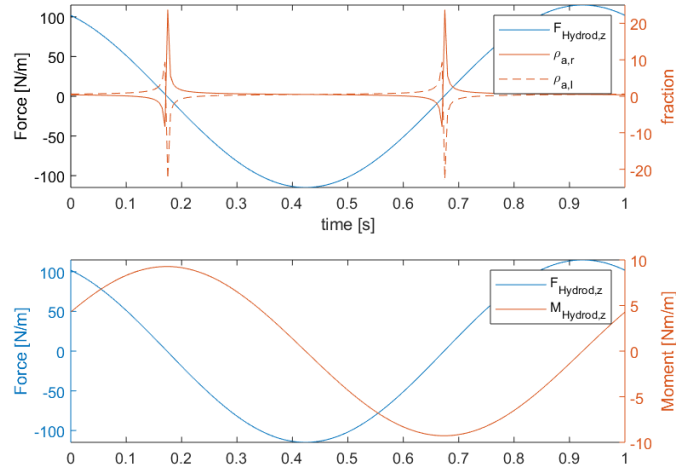
Figure A.10: Hydrodynamic moment as function of the vertical hydrodynamic force.

The total hydrodynamic moment is the summation of the moment due to vertical and horizontal accelerating flow presented in eq A.27.

$$M_{hydrod,y} = M_{hydrod,\overrightarrow{z}} + M_{hydrod,\overrightarrow{x}} \tag{A.27}$$

A.4. Drag forcing

The forcing due to drag is found in a similar way as the hydrodynamic forcing. The largest difference is the method of integration. The hydrodynamic forcing is proportional to the water acceleration while the drag is proportional to the water velocity squared. All components on which the drag force is based on, should be integrated with respect to the water velocity squared. A visualization of the water velocity in the SFT domain is presented in figure A.11.
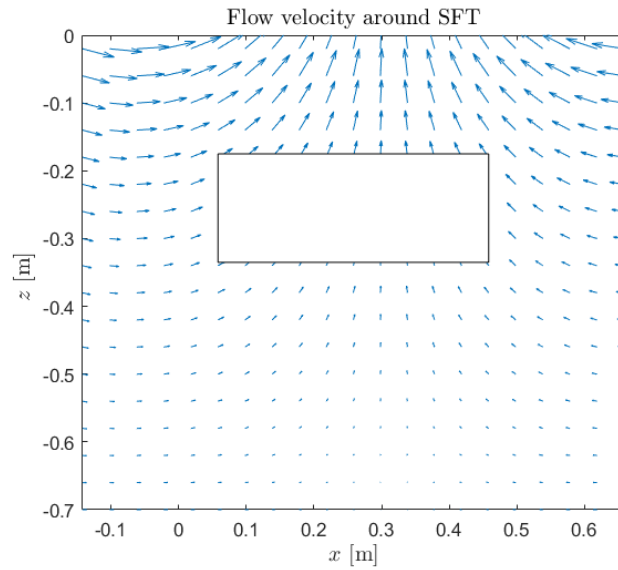
Figure A.11: Undisturbed water velocity around SFT. $T = 1.0s$, $H = 0.08m$, $s1 = 0.175m$, $t = 1.2s$.

The water velocity is divided in horizontal and vertical components presented in figure A.12.
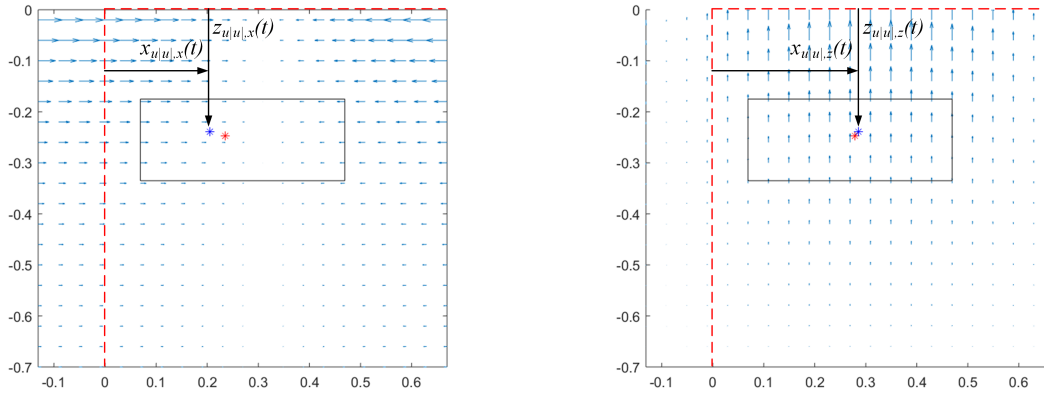
(a) Water velocity in x direction. In red, the resultant in x, z direction for horizontal water velocity. In blue, the resultant in x, z direction for horizontal water velocity squared.

(b) Water velocity in z direction. In red, the resultant in x, z direction for vertical water velocity. In blue, the resultant in x, z direction for vertical water velocity squared.

Figure A.12: Horizontal and vertical water velocity due to harmonic wave in domain. $T = 1.0 s$, $H = 0.08 m$, $s1 = 0.175 m$, $t = 1.2 s$

In red, the resultant in x, z direction is plotted for both the horizontal and vertical water velocity. Because the drag force is proportional to the water velocity squared, the resultant of the water velocity squared is determined and visualized by a blue marker in both plots. The location of the resultant for the horizontal and vertical water velocity squared can be found in eq A.28 - A.31.

$$x_{u|u|,x}(t) = \frac{1}{\int_{s_0-\gamma}^{s_0-\gamma+2a} |u_x u_x| \, dx} \int_{s_0-\gamma}^{s_0-\gamma+2a} |u_x u_x| x \, dx \tag{A.28}$$

$$z_{u|u|,x} = \frac{1}{\int_{-d1}^{-s1} |u_x u_x| \, dz} \int_{-d1}^{-s1} |u_x u_x| z \, dz \tag{A.29}$$

$$x_{u|u|,z}(t) = \frac{1}{\int_{s_0-\gamma}^{s_0-\gamma+2a} |u_z u_z| \, dx} \int_{s_0-\gamma}^{s_0-\gamma+2a} |u_z u_z| x \, dx \tag{A.30}$$

$$z_{u|u|,z} = \frac{1}{\int_{-d1}^{-s1} |u_z u_z| \, dz} \int_{-d1}^{-s1} |u_z u_z| z \, dz \tag{A.31}$$

Likewise the resultant point for the acceleration of water, the resultant point of the water velocity squared oscillates from left two right. This cycle also takes place two times in one period. The x and z location of the resultant point for the velocity squared flow is used to compute the resultant water velocity for the horizontal and vertical direction. For the horizontal drag force, the water velocity should be integrated over the height of the object at the horizontal location $x_{u|u|,x}(t)$, eq A.32. For the vertical drag force, the water velocity should be integrated over the width of the object at the vertical location $z_{u|u|,z}$, eq A.33.

$$\overline{u_x} = \frac{1}{b} \int_{-d1}^{-s1} u_x \bigg|_{x=x_{u|u|,x}(t)} dz \tag{A.32}$$

$$\overline{u_z} = \frac{1}{2a} \int_{s_0-\gamma}^{s_0-\gamma+2a} u_z \bigg|_{z=z_{u|u|,z}(t)} dx \tag{A.33}$$

Now that the resultant water velocities in the x, z plane are computed in time, it is possible to determine the drag force according to eq A.34 and eq A.35.

$$F_{drag,x} = \frac{1}{2} \rho b C_d \overline{u_x} |\overline{u_x}| \tag{A.34}$$

$$F_{drag,z} = \frac{1}{2} \rho 2 a C_d \overline{u_z} |\overline{u_z}| \tag{A.35}$$

In the same way as figure A.7, coefficients can be computed to correct in case of short waves. Because the drag force is proportional to the water velocity squared, the coefficient needs to be proportional to the water velocity squared as well. The result is presented in figure A.13.
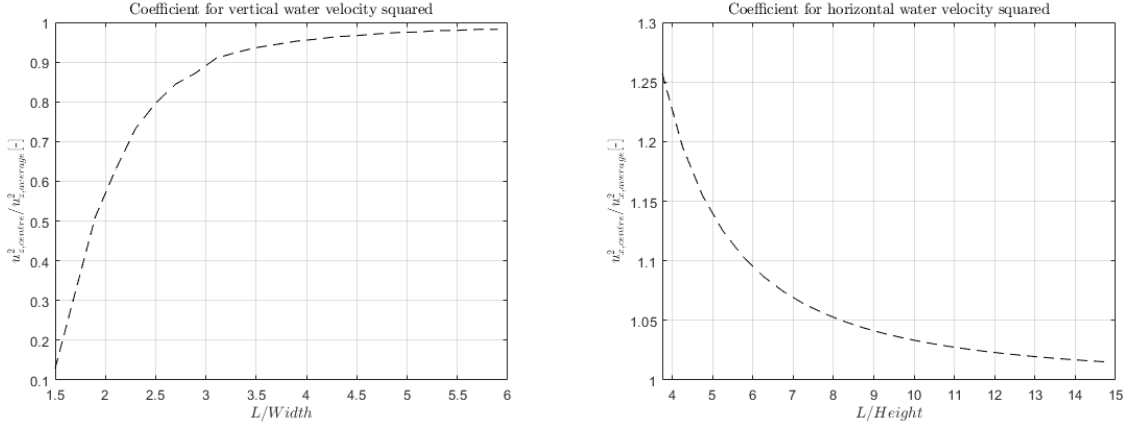
(a) Coefficient for the vertical water velocity squared as function of the wave length structure length ratio.

(b) Coefficient for the horizontal water velocity squared as function of the wave length structure height ratio.

Figure A.13: Correction coefficients for the vertical and horizontal water velocity squared for short waves. These curves are independent on the submerged depth and the wave height and can be used to correct for short waves.

The drag rotational is determined based on the two drag forces from eq A.34 and A.35. The drag moment which is caused by the horizontal drag force is presented in eq A.36.

$$M_{drag,\vec{x}} = F_{drag,x} \times \left[z_{u|u|,x}(t) - s_0 - \frac{1}{2}b \right] \tag{A.36}$$

To compute the drag moment due to the vertical drag force, fictive ratio parameters are introduced. These are computed with a simple supported beam model presented in figure A.14.
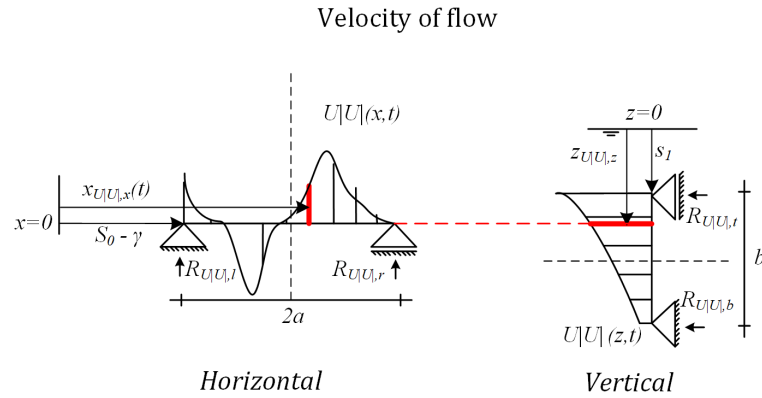
Figure A.14: Flow velocity profile squared schematised on simply supported beams

The load on the simply supported beam is described by the vertical water velocity squared at depth $z_{u|u|,z}$. The water velocity squared reaction forces are determined and elaborated in A.37 and A.38.

$$R_{u|u|,r} = \frac{1}{2a} \int_{s_0-\gamma}^{s_0-\gamma+2a} u_z |u_z|(x - s_0 + \gamma) dx \tag{A.37}$$

$$R_{u|u|,l} = \int_{s_0-\gamma}^{s_0-\gamma+2a} u_z |u_z| dx - R_{u|u|,r} \tag{A.38}$$

The fictive water velocity squared reaction forces can be translated to a percentile of the total water velocity squared, which is elaborated in eq A.39 and in eq A.40.

$$\rho_{u|u|,r} = \frac{R_{u|u|,r}}{R_{u|u|,r} + R_{u|u|,l}} \tag{A.39}$$

$$\rho_{u|u|,l} = \frac{R_{u|u|,l}}{R_{u|u|,r} + R_{u|u|,l}} \tag{A.40}$$

Multiplying the percentile of the total velocity squared with the resultant vertical drag force will give the drag force at the right and left connection point. The moment due to the vertical drag is elaborated in eq A.41.

$$M_{drag,\overrightarrow{z}} = a \times \rho_{u|u|,r} F_{drag,z} - a \times \rho_{u|u|,l} F_{drag,z} \tag{A.41}$$

The total drag moment is the summation of the moment due to vertical and horizontal velocity flow presented in eq A.42.

$$M_{drag,y} = M_{drag,\overrightarrow{z}} + M_{drag,\overrightarrow{x}} \tag{A.42}$$

A.5. Calibration of force prediction coefficients

In this section, the vertical and horizontal inertia coefficients are calibrated. The loading condition is without current. In figure A.15, the wave forces on the restrained SFT are plotted as function of the wave number k. The red line shows the theoretical value of the inertia coefficient. The dashed line shows the upper and lower bound of the wave force. The upper boundary is determined with an inertia coefficient of 2.0 and the lower bound is determined with an inertia coefficient of 1.0. The green line is tuned to fit the measured data the best.
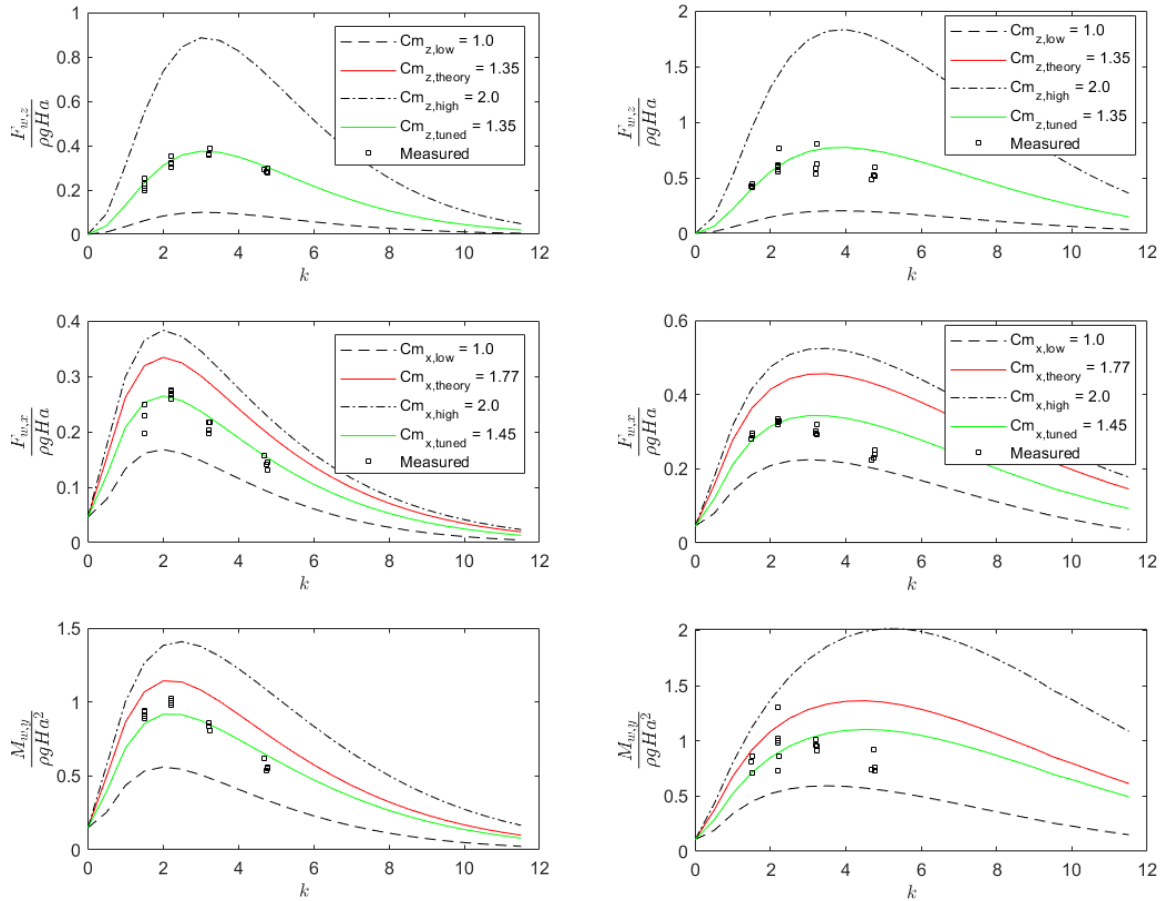
(a) Submergence depth of $s_1 = 0.35m$.   (b) Submergence depth of $s_1 = 0.35m$.

Figure A.15: Calibration of inertia coefficients C_{mx} and C_{mz}. To calibrate the coefficients, data from physical model experiments is used Drost (2019).

In table A.1, the tuned values of the vertical and horizontal inertia coefficients are presented. These will be used for the wave force prediction in a wave current environment without the presents of current.

Table A.1: Calibrated inertia coefficients based on physical experiments.

Inertia coefficient	Value
$C_{mz,tuned}$	1.35
$C_{mx,tuned}$	1.45

A.6. Current forcing

The current forcing is separated from the wave forcing. The current forcing $F_{cur,x}$ is determined with eq A.43.

$$F_{cur,x} = \frac{1}{2}\rho b C_{d,c} U_c |U_c| \tag{A.43}$$

In eq A.43, C_d, c is determined based on physical experiments of which the results are presented in figure A.16a. The presence of the current does not influence the wave velocity potential. Instead of changing the velocity potential, the inertia coefficients, which are used for the force determination in the wave force module, are adapted. The value of C_{mz} and C_{mx} is determined with KC dependent functions which are presented in eq A.44 and in eq A.45. Both functions are obtained from physical experiments of which the he results are presented in figure A.16b and in figure A.16c.

$$C_{mz} = 3.65 - 0.2(KC)^2 \tag{A.44}$$

$$C_{mx} = 1.557 - 0.09(KC)^2 \tag{A.45}$$
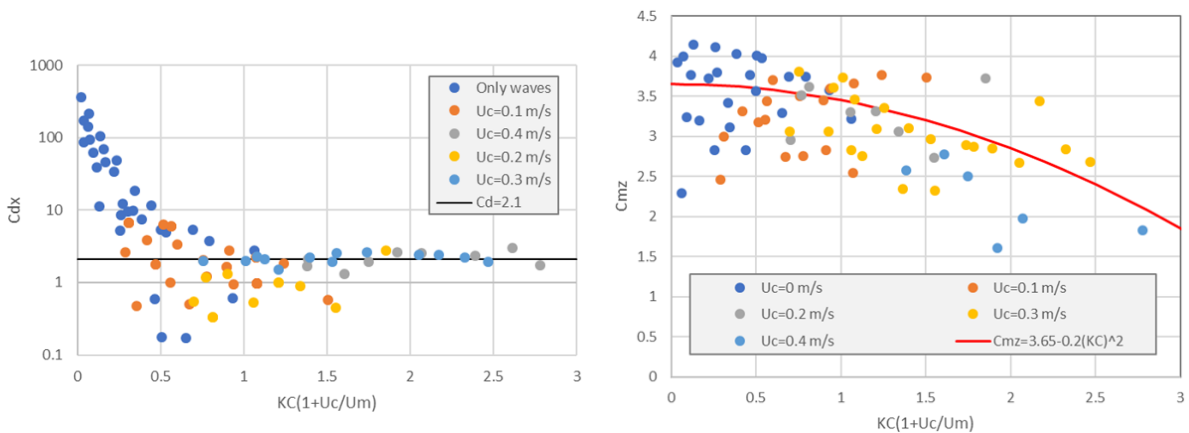
(a) Effect of current on Morison's drag coefficient C_d.

(b) Effect of current on Morison's vertical inertia coefficient C_{mz}.
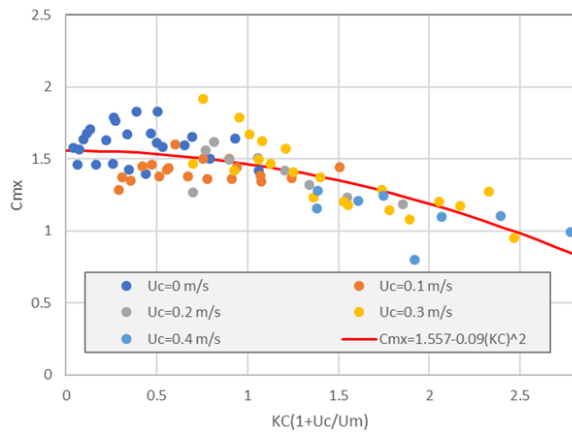
(c) Effect of current on Morison's horizontal inertia coefficient C_{mx}

Figure A.16: Influence of current on hydrodynamic coefficients (X.Chen, n.d.).

B

Dynamic module

**In this appendix, the dynamic module is elaborated in detail. The dynamic module describes the oscilla-
tions of the submerged floating tunnel (SFT) in still water. Parameter definitions are given in the first sec-
tion followed by the procedure to obtain the moment of inertia of the SFT. Subsequently, the stabilising
moment is derived. This stabilizing moment is not taking into account wave loading. Finally he damping
and added mass of the dynamic system is explained, followed by the equation of motion (EOM) of the SFT
oscillating in still water.**

B.1. Parameter definitions

The parameters that are used are introduced in figure B.1. The tunnel has a width of $2a$ and a height of b.
The submergence depth is s_1 below the still water level. The water depth is denoted by h_1. The tunnel is
connected with the tethers at a γ from the sides and ϵ from the bottom. The distance between the tunnel
bottom and the bottom in which the tethers are anchored is denoted by h_2. The distance between the tunnel
connection and the still water level is indicated by d_1. The distance between the tether anchorage point and
the sides of the tunnel is s_0.
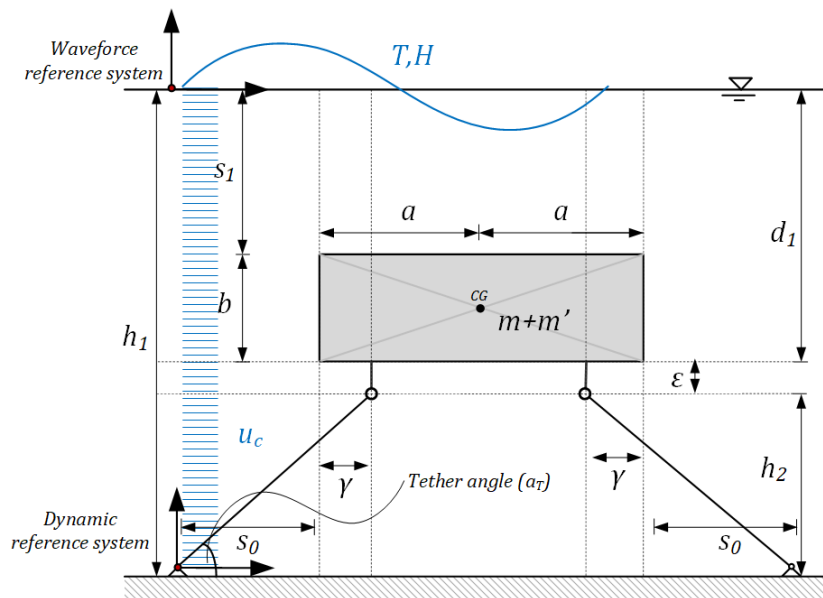
Figure B.1: Parameter definitions in dynamic module.

The tunnel has two ridged in-extensible tethers which are located under an angle. This angle is named
the tether angle. In the computations, the symbol α_T is used.

B.2. Moment of inertia

To obtain the moment of inertia, the system is schematized which can be seen in figure B.2. Let us first introduce a reference system. Since the sea bed is not moving, it is convenient to choose a fixed reference system at the left tether anchor points. The origin of this fixed reference system is indicated with $O\{X, Z\}$. The left tether is chosen because this is at the same horizontal location as the reference system for the hydraulic loads. The system is displaced in the positive X direction. Furthermore a local reference system is used which origin moves, located at the connection of the left eye of the tunnel body and the left tether. This local reference system is indicated by $O\{x_1, z_1\}$. The tethers will make an angle with θ_1 and the body starts to rotate with θ_2. The location of the submerged body with respect to the fixed coordinate system is indicated with $\{X_B, Z_B\}$. Note that each point of the tunnel body moves differently with respect to the fixed reference system. Therefore the vertical and horizontal coordinate of an arbitrary point of the tunnel body is dependent on x_1 and z_1. The equation of motion is obtained by using the assumption of small vibrations. The rotation of the submerged body is small and therefore it can be assumed that, for both θ_1 and θ_2, $\sin(\theta)) \approx \theta$ and $\cos(\theta) \approx (1 - \frac{\theta^2}{2})$.
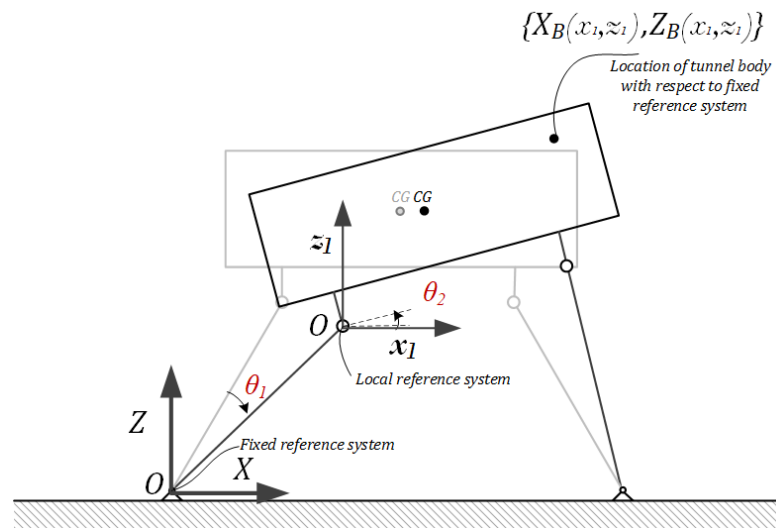
Figure B.2: Schematic of geometry in displaced position

A free floating tunnel has three degrees of freedom which are roll, sway and heave. This dynamic system assumes the tunnel is connected with two in-extensible tethers. Adding two rigid constrains to the free floating tunnel reduces the SFT to a single degree of freedom (SDOF) system. The equation of motion for this SDOF system can be obtained by using the Lagrangian formalism (Metrikine, 2006). This formalism is based on the Lagrangian equations which can be found in eq B.1.

$$\frac{d}{dt}\frac{\partial L}{\partial \dot{q}_s} - \frac{\partial L}{\partial q_s} = Q_s \tag{B.1}$$

where

$$L = E_K - E_P \tag{B.2}$$

in which

L	=	Lagrange function
q_s	=	generalized coordinates
Q_s	=	generalized forces acting on the system
E_k	=	Kinetic energy
E_p	=	Potential energy

The kinetic energy E_k of the system, presented in eq B.3, and potential energy E_p of the system, presented in eq B.4, can be written. Note that the contribution of the potential energy is zero because the centre of gravity

of the tunnel stays at the same height during its movement. This can be observed in figure B.2, in which the centre of gravity of the tunnel body is indicated with *CG*.

$$E_k = \frac{m}{4a} \int_{-\gamma}^{2a-\gamma} \dot{Z_b}^2 dx_1 + \frac{m}{2b} \int_{\epsilon}^{b+\epsilon} \dot{X_B}^2 dz_1 \tag{B.3}$$

$$E_p = \frac{m}{2a} g \int_{-\gamma}^{2a-\gamma} (Z_b - Z_b(\theta_1 = 0, \theta_2 = 0)) dx_1 = 0 \tag{B.4}$$

To determine the kinetic energy E_k, the velocity of the tunnel needs to be determined with respect to the fixed reference system as function of θ_1 and θ_2. The velocity of the SFT can be obtained by taking the derivative of the location of the SFT. The horizontal and vertical location of each part of the tunnel is indicated with the coordinate $\{X_B, Z_B\}$. First the position of the local reference system $O\{x_1, z_1\}$, with respect to the fixed reference system, is determined as function of θ_1. The horizontal location of the origin, with respect to the fixed reference system, is indicated with $O_x\{x_1, z_1\}$ and the vertical location of the origin, with respect to the fixed reference system, is indicated with $O_z\{x_1, z_1\}$.

$$O_x\{x_1, z_1\} = s_0 + h_2 \sin(\theta_1) - s_0(1 - cos(\theta_1)) \approx s_0 + h_2 \theta_1 - s_0 \frac{\theta_1^2}{2} \tag{B.5}$$

$$O_z\{x_1, z_1\} = h_2 - h_2(1 - cos(\theta_1)) - s_0 \sin(\theta_1) \approx h_2 - h_2 \frac{\theta_1^2}{2} - s_0 \theta_1 \tag{B.6}$$

Now the location of the local reference system is determined with respect tot the fixed reference system, it is possible to formulate an expression which describes each point of the tunnel body with respect to the fixed reference system $O\{X, Z\}$ as function of θ_1 and θ_2. The expression for the horizontal coordinate of each point of the tunnel is elaborated in eq B.7. The expression for the vertical coordinate of each point of the tunnel is elaborated in eq B.8.

$$X_B(x_1, z_1) = O_x\{x_1, z_1\} + x_1 \cos(\theta_2) - z_1 \sin(\theta_2) \approx O_x\{x_1, z_1\} + x_1(1 - \frac{\theta_2^2}{2}) - z_1 \theta_2 =$$
$$s_0 + h_2 \theta_1 - s_0 \frac{\theta_1^2}{2} + x_1 - x_1 \frac{\theta_2^2}{2} - z_1 \theta_2 \tag{B.7}$$

$$Z_B(x_1, z_1) = O_z\{x_1, z_1\} + z_1 \cos(\theta_2) + x_1 \sin(\theta_2) \approx O_z\{x_1, z_1\} + z_1(1 - \frac{\theta_2^2}{2}) + x_1 \theta_2 =$$
$$h_2 - h_2 \frac{\theta_1^2}{2} - s_0 \theta_1 + z_1 - z_1 \frac{\theta_2^2}{2} + x_1 \theta_2 \tag{B.8}$$

Because the SFT tunnel is connected with two rigid constrains, θ_1 and θ_2 are proportional to each other. In case of small vibrations, this proportionality is linear. This can be observed in figure B.3.
Because of small rotations, the following relation between θ_1 and θ_2 derived:

$$\theta_1 = \lambda \theta_2 = \frac{\sqrt{(a-\gamma)^2 + (\frac{(a-\gamma)}{s_0} h_2)^2}}{\sqrt{h_2^2 + s_0^2}} \theta_2 \tag{B.9}$$

Now the horizontal and vertical location of the tunnel is described, the horizontal and vertical velocity can be determined by taking the derivative. Additionally, the relation between θ_1 and θ_2 is used. The velocity in X and Z direction of the SFT body reads:

$$\dot{X}_B(x_1, z_1) = h_2 \lambda \dot{\theta}_2 - s_0 \lambda^2 \dot{\theta}_2 \theta_2 - x_1 \theta_2 \dot{\theta}_2 - z_1 \dot{\theta}_2 \tag{B.10}$$

$$\dot{Z}_B(x_1, z_1) = s_2 \lambda \dot{\theta}_2 - h_0 \lambda^2 \dot{\theta}_2 \theta_2 - z_1 \theta_2 \dot{\theta}_2 + x_1 \dot{\theta}_2 \tag{B.11}$$

The non linear terms are removed from eq B.10 and eqB.11 and than squared. The result can be found in eq B.12 and eq B.13

$$\dot{X}_B^2 = (h_2 \lambda \dot{\theta}_2 - z_1 \dot{\theta}_2)^2 \tag{B.12}$$

$$\dot{Z}_B^2 = (-s_2 \lambda \dot{\theta}_2 + x_1 \dot{\theta}_2)^2 \tag{B.13}$$
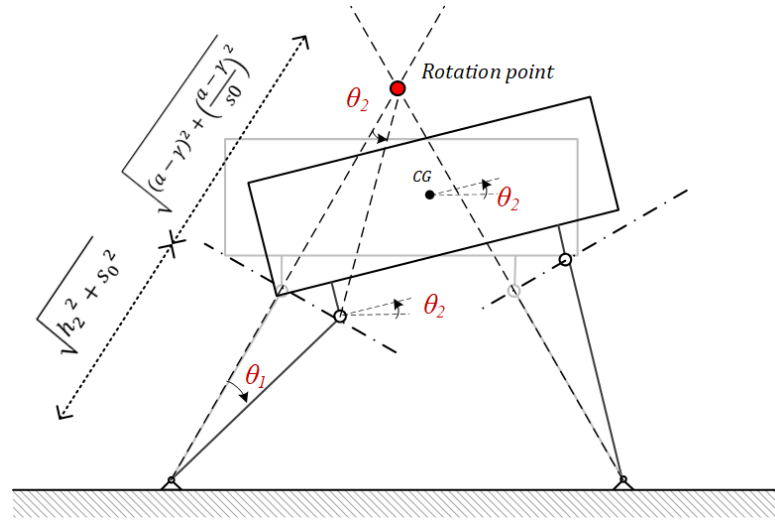
Figure B.3: Visualization of linear proportionality between θ_1 and θ_2.

The squared horizontal and vertical velocity of the submerged body are now inserted in eq B.3 and the total kinetic energy can be formulated.

$$E_k = \frac{m}{4a} \int_{-\gamma}^{2a-\gamma} (-s_2 \lambda \dot{\theta}_2 + x_1 \dot{\theta}_2)^2 \, dx_1 + \frac{m}{2b} \int_{\epsilon}^{b+\epsilon} (h_2 \lambda \dot{\theta}_2 - z_1 \dot{\theta}_2)^2 \, dz_1$$

Employing the Lagrangian formalism gives the following expression:

$$\frac{d}{dt} \frac{d}{d\dot{\theta}_2} (E_k - E_p) - \frac{d}{d\theta_2} (E_k - E_p) = \frac{d}{dt} \frac{dE_k}{d\dot{\theta}_2} =$$

$$\frac{d}{dt} \frac{dE_k}{d\dot{\theta}_2} = \frac{d}{dt} \frac{d}{d\dot{\theta}_2} \left(\frac{m}{4a} \int_{-\gamma}^{2a-\gamma} (-s_2 \lambda \dot{\theta}_2 + x_1 \dot{\theta}_2)^2 \, dx_1 + \frac{m}{2b} \int_{\epsilon}^{b+\epsilon} (h_2 \lambda \dot{\theta}_2 - z_1 \dot{\theta}_2)^2 \, dz_1 \right) =$$

$$\frac{m}{4a} \int_{-\gamma}^{2a-\gamma} 2(-s_2 \lambda \ddot{\theta}_2 + x_1 \ddot{\theta}_2)(-s_2 \lambda + x_1) \, dx_1 + \frac{m}{2b} \int_{\epsilon}^{b+\epsilon} 2(h_2 \lambda \ddot{\theta}_2 - z_1 \ddot{\theta}_2)(h_2 \lambda - z_1) \, dz_1 =$$

$$\frac{m}{2a} \int_{-\gamma}^{2a-\gamma} (x_1^2 \ddot{\theta}_2 - 2 s_0 \lambda x_1 \ddot{\theta}_2 + s_0^2 \lambda^2 \ddot{\theta}_2) \, dx_1 + \frac{m}{b} \int_{\epsilon}^{b+\epsilon} (z_1^2 \ddot{\theta}_2 - 2 h_2 \lambda z_1 \ddot{\theta}_2 + h_2^2 \lambda^2 \ddot{\theta}_2) \, dz_1 =$$

$$\frac{m}{2a} \left[\frac{1}{3} x_1^3 \ddot{\theta}_2 - s_0 \lambda x_1^2 \ddot{\theta}_2 + s_0^2 \lambda^2 x_1 \ddot{\theta}_2 \right]_{-\gamma}^{2a-\gamma} + \frac{m}{b} \left[\frac{1}{3} z_1^3 \ddot{\theta}_2 - h_2 \lambda z_1^2 \ddot{\theta}_2 + h_2^2 \lambda^2 z_1 \ddot{\theta}_2 \right]_{\epsilon}^{b+\epsilon} =$$

$$\ddot{\theta}_2 m \left(\frac{4a^2 + b^2}{3} - 2 s_0 \lambda a - h_2 \lambda b + s_0^2 \lambda^2 + h_2^2 \lambda^2 + 2\gamma \lambda s_0 - \gamma^2 - 2a\gamma - 2\epsilon h_2 \lambda + b\epsilon + \epsilon^2 \right) = Q_s$$

The equation of motion with a generalized force acting on the system is described in eq B.14. In this equation, J is the moment of inertia of the rotating tunnel body around the rotation point.

$$\frac{d^2\theta_2}{dt^2} J = Q_s \tag{B.14}$$

in which:

$$J = m \times \left(\frac{4a^2 + b^2}{3} - 2 s_0 \lambda a - h_2 \lambda b + s_0^2 \lambda^2 + h_2^2 \lambda^2 + 2\gamma \lambda s_0 - \gamma^2 - 2a\gamma - 2\epsilon h_2 \lambda + b\epsilon + \epsilon^2 \right) \tag{B.15}$$

In case the tunnel is submerged in water, added mass needs to be taken into account. The moment of inertia, taking into account added mass, is presented in eq B.16.

$$J = (m + m') \times \left(\frac{4a^2 + b^2}{3} - 2 s_0 \lambda a - h_2 \lambda b + s_0^2 \lambda^2 + h_2^2 \lambda^2 + 2\gamma \lambda s_0 - \gamma^2 - 2a\gamma - 2\epsilon h_2 \lambda + b\epsilon + \epsilon^2 \right) \tag{B.16}$$

in which

m' = added mass

B.2.1. Rotational point

As indicated in figure B.3, the rotational point can be found at the intersection of the two tether axis when the SFT is at rest. However it should be noted that during the rotation of the SFT, a horizontal motion is involved and the centre of gravity remains on the same height. This horizontal motion in combination with a constant height of the centre of gravity causes that the rotation of the tunnel body is not exact around the fixed rotational point. This is illustrated in figure B.4a. In this figure, the tunnel body is visualized for a set of rotations. The maximal tunnel rotation is for $|\theta_2| = 0.5$ [rad]. For each tunnel rotation, a line from the centre of gravity, perpendicular to the top of the tunnel, has been plotted. In case the tunnel is at rest, this line goes exact trough the fixed rotational point. However when θ_2 becomes larger, this rotational line has a slight error with respect to the fixed rotational point. This means that the rotation of the tunnel is not exact around the fixed rotational point. The error which is made is plotted as function of θ_2 and presented in figure B.4b. It can be observed that for small rotations, e.g. 0.2 [rad], errors are less than 2 %. In case of small vibrations, the location of this rotation point can be assumed fixed.

(a) Rotation of SFT body around rotational point.

(b) Rotation point error.
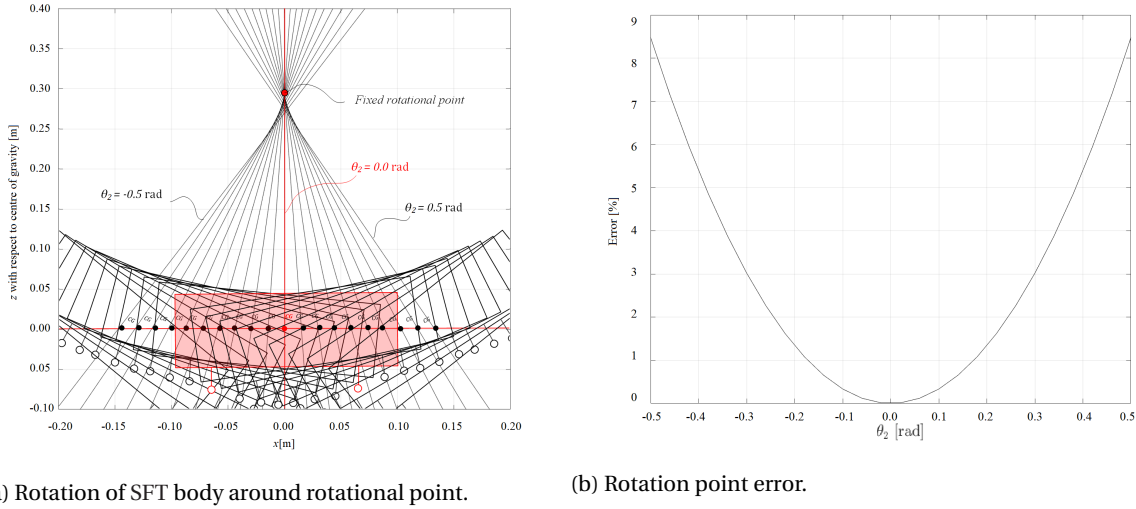
Figure B.4: Plotting the rotation of the SFT body for various angles of θ_2 shows that the fixed rotational point is not the exact rotational point. For large rotations, the error becomes large.

B.2.2. Generalized force

The generalized force Q_s, presented in eq B.15, is a moment around the fixed rotational point. The generalized moment Q_s consists of three parts, the stabilizing moment M_s, the damping moment M_c and the external wave-current moment M_w. The stabilizing moment ensures the stiffness of the system. The forces in the tethers cause a moment which counteracts the rotation of the SFT. The damping force ensures the damping due to the water around the SFT and the external moment is due to waves and current. The external moment has impact on the tether forces and thus on the stiffness of the system. In this appendix, the dynamic module does not take into account waves and currents. The coupling of the external wave-current moment with the dynamic system is elaborated in appendix C.

B.3. Stabilizing moment independent of external forcing

The stabilizing moment is due to the buoyancy force and the tether forces. The tether forces can be computed based on force equilibrium. To determine the outer tether force, the sum of moments around the left tether anchorage point is taken, not taken into account the damping forces. A schematization of the forces is given in figure B.5.

The equation to determine the outer tether force T_{outer} is presented in eq B.17. Please note, α_T is the tether angle defined as the angle between the tether axis and the seabed when the tunnel is in equilibrium position.

$$T_{outer} = \frac{F_b \times \left[x(t) + s_0 + a - \gamma \right]}{P_r} \qquad (B.17)$$
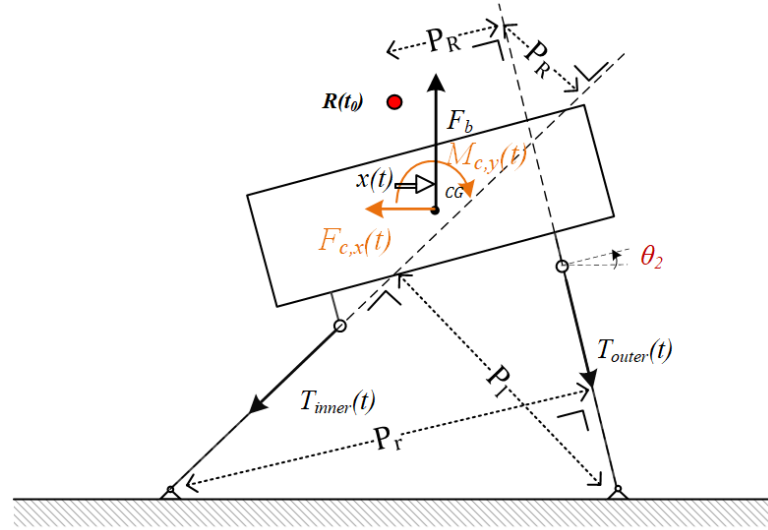
Figure B.5: Schematization of dynamic system with buoyancy force and tether forces in black and damping forces in orange.

In the same way, the inner tether force T_{inner} can be determined by taking the sum of moments around the right tether anchorage point, not taking into account the damping forces. This equation is presented in eq B.18.

$$T_{inner} = \frac{F_b \times \left[-x(t) + s_0 + a - \gamma \right]}{P_l} \tag{B.18}$$

in which

$$P_r = \sin\left(\alpha_T + \lambda\theta_2\right)\right)(2s_0 + 2a - 2\gamma) \tag{B.19}$$
$$P_l = \sin\left(\alpha_T - \lambda\theta_2\right)\right)(2s_0 + 2a - 2\gamma) \tag{B.20}$$

It should be noted that eq B.19 and eq B.20 are non-linear equations. Both equations are rewritten, with trigonometric identities, and than made linear by taking the advantage of small vibrations. Taking the Taylor series with an expansion order of 2 gives the same result. The linearized eq B.19 and eq B.20 are presented in eq B.21 and eq B.22.

$$
\begin{aligned}
P_r &= \sin\left(\alpha_T + \lambda\theta_2\right)\right)(2s_0 + 2a - 2\gamma) \\
&= \left[\sin\left(\alpha_T\right)\cos\left(\lambda\theta_2\right) + \cos\left(\alpha_T\right)\sin\left(\lambda\theta_2\right) \right] \times (2s_0 + 2a - 2\gamma) \\
&\approx \left[\sin\left(\alpha_T\right) + \cos\left(\alpha_T\right)\lambda\theta_2 \right] \times (2s_0 + 2a - 2\gamma) \\
P_l &= \sin\left(\alpha_T - \lambda\theta_2\right)\right)(2s_0 + 2a - 2\gamma) \\
&= \left[\sin\left(\alpha_T\right)\cos\left(\lambda\theta_2\right) - \cos\left(\alpha_T\right)\sin\left(\lambda\theta_2\right) \right] \times (2s_0 + 2a - 2\gamma) \\
&\approx \left[\sin\left(\alpha_T\right) - \cos\left(\alpha_T\right)\lambda\theta_2 \right] \times (2s_0 + 2a - 2\gamma)
\end{aligned}
$$

$$\tag{B.21}$$
$$\tag{B.22}$$

The stabilizing moment due to the buoyancy force and the tether forces with respect to the fixed rotation point is elaborated in eq B.23.

$$M_s = 2P_R(T_{inner} + T_{outer}) - x(t)F_b \tag{B.23}$$

in which

$$P_R = \theta_2 \lambda \sqrt{\left[s_0 + 2a - 2\gamma\right]^2 + \left[h_2 + \frac{h_2}{s_0}(a-\gamma)\right]^2} \tag{B.24}$$

It can be observed both from figure B.5 and eq B.23 that the contribution of the buoyancy force is destabilizing and the contribution of the tether forces is stabilizing. The resultant moment is always stabilizing and therefore the moment is indicated with 'stabilizing moment'.

B.4. Damping moment + added mass

The rotational damping moment is presented in eq B.25. The horizontal damping force is presented in eq B.26.

$$M_{c,y} = C_s \dot{\phi}(t) |\dot{\phi}(t)| \tag{B.25}$$

$$F_{c,x} = C_r \dot{x}(t) |\dot{x}(t)| \tag{B.26}$$

in which

C_r	=	roll damping coefficient
C_s	=	sway damping coefficient

The damping forces creates a damping moment around the fixed resultant point. The damping moment is expressed in eq B.27 in which z_R is the vertical distance between centre of gravity and fixed rotational point. The distance z_R is indicated in figure B.5.

$$M_c = z_R F_{c,x} + M_{c,y} \tag{B.27}$$

$$z_R = \frac{h_2}{s_0}(a-\gamma) - \epsilon - \frac{1}{2}b \tag{B.28}$$

Vibrations of the structure causes the fluid around the structure to accelerate as well. The water moves along with the structure which gives extra mass to the system. If mass is added to the system, the rotational moment of inertia J of the system becomes larger. This can be observed in eq B.29. A larger moment of inertia gives a lower natural frequency. The added mass m' should be between 0 and 100 %.

$$J = (m + m') \times \left(\frac{4a^2 + b^2}{3} - 2s_0 \lambda a - h_2 \lambda b + s_0^2 \lambda^2 + h_2^2 \lambda^2 + 2\gamma \lambda s_0 - \gamma^2 - 2a\gamma - 2\epsilon h_2 \lambda + b\epsilon + \epsilon^2 \right) \tag{B.29}$$

B.4.1. Tuning damping coefficients and added mass

Two different decay tests are used to tune the damping coefficients and added mass.

- The **roll damping coefficient** is tuned on model experiments with the following configuration:
  $\alpha = 30°$, $s_1 = 0.175m$.

- The **sway damping coefficient** is tuned on model experiments with the following configuration:
  $\alpha = 70°$, $s_1 = 0.35m$.

- The **added mass** is tuned on model experiments with the following configuration:
  $\alpha = 70°$, $s_1 = 0.35m$.

The roll damping coefficient is tuned with a 30° tether angle because this configuration gives a pure roll motion. In this way the roll damping can be tuned based on pure roll. The sway damping is tuned with the 70° tether angle because this configuration gives the largest sway motion and the smallest roll motion. The added mass is tuned with the 70° tether angle because this configuration gives the largest motions. Added mass becomes important when osculations become large. The free decay tests for both tether configurations are presented in figure B.6. The tuned hydro dynamic coefficients are obtained and stored in table B.1.

For both tether configurations the damping is tuned which results in a corresponding decay of the data set with the model prediction for both decay tests. The added mass is tuned on the decay test with tether
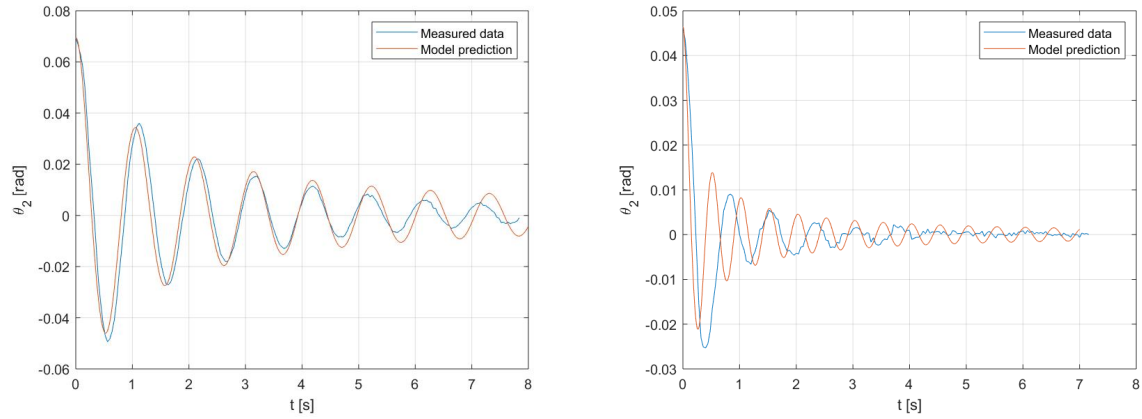
(a) Free decay test. $\alpha = 70°$, $s_1 = 0.35m$. Tuned sway damp- ing coefficient $C_h = 750$, tuned added mass $m' = 0.55 \times m$.

(b) Free decay test. $\alpha = 30°$, $s_1 = 0.175m$. Tuned roll damp- ing coefficient $C_r = 8$.

Figure B.6: Tuning of C_r, C_s and M_a with free decay tests.

Table B.1: Hydrodynamic coefficient

Hydrodynamic coefficient	Value	Unit
C_r	8	$[Nms^2/\,\mathrm{rad}^2]$
C_s	750	$[Ns^2/m]$
m'	$0.55 \times m$	[-]

angle $\alpha = 70°$ and submerged depth $s_1 = 0.35m$. The natural period of the model and the data are matching well. The model takes into account a total added mass and does not make a distinction between roll added mass and sway added mass. This causes that the natural frequency of the $\alpha = 30°$ tether configuration is under predicted by the model.

B.5. Equation of motion dynamic module

The elaboration of eq B.14, gives the following equation of motion presented in eq B.30. A clarification of EOM describing the oscillation of a SFT in still water is given in figure B.7.

$$\frac{d^2\theta_2}{dt^2}J + M_c + M_s = 0 \tag{B.30}$$

in which

J	=	Moment of inertia
M_c	=	Damping moment
M_s	=	Stabilizing moment independent of external forcing
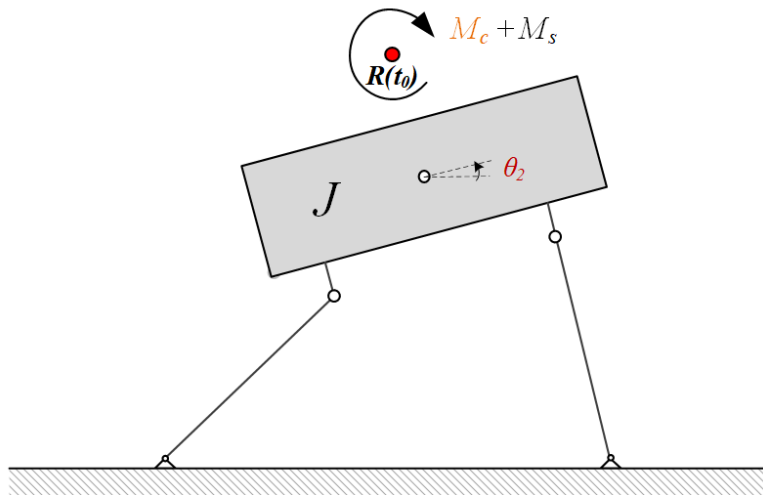
Figure B.7: Clarification of the EOM describing the oscillation of a SFT in still water.

C

Coupling module

In this appendix, the coupling module is elaborated in detail. The coupling module describes the oscillations of the submerged floating tunnel (SFT) forced by waves and current. The coupling module combines the wave force module with the dynamic module. The equation of motion (EOM), derived in appendix B, needs some adaptations due to the addition of the wave forces. The stabilizing moment is affected by the external forces. First the stabilizing moment is modified. Subsequently, the external wave-current forces are inserted in the EOM. Finally the full EOM, describing the oscillations of the SFT forced by waves and current, is given.

C.1. Stabilizing moment dependent on external forcing

The stabilizing moment is due to the tether forces and the buoyancy force. Different from the dynamic module is the presence of wave-current forces. These wave-current forces influence the tether forces and thus also the stabilizing moment. The stabilizing moment, and thus the stiffness of the system, is thus dependent on the tether forces, buoyancy force and wave-current forces. The tether forces can be computed based on force equilibrium. To determine the outer tether force, the sum of moments around the left tether anchorage point is taken. This also includes the wave forces. A schematization of the forces is given in figure C.1. The damping forces do not contribute to forces is the tethers. It can be observed that the wave forces are attached to the centre of gravity of the SFT. In case the SFT moves, the forces move with the tunnel.
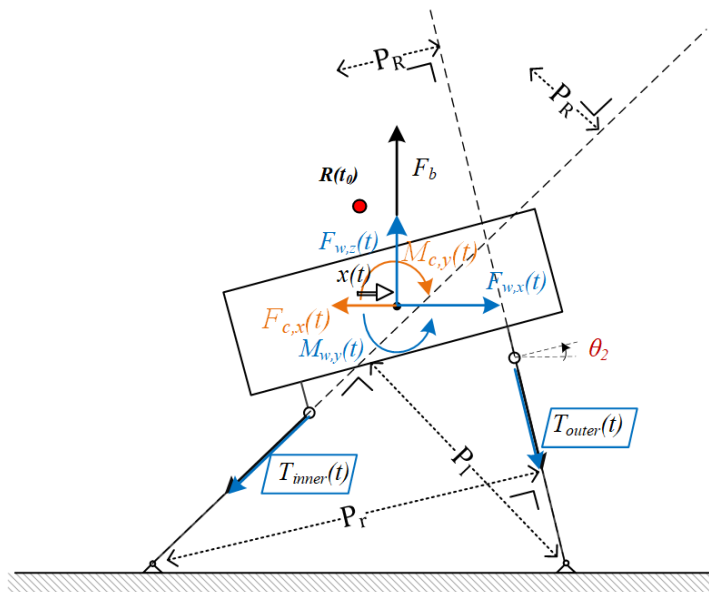
Figure C.1: Schematization of dynamic system with forces from dynamic module and wave force module.

The equation to determine the right tether force T_{outer} is presented in eq C.1. Please note, α_T is the tether angle defined as the angle between the tether axis and the seabed when the tunnel is in equilibrium position.

$$T_{outer} = \frac{(F_b + F_{w,z}(t)) \times \left[x(t) + s_0 + a - \gamma\right] - (F_{w,x}(t) + F_{cur,x}(t)) \times [h_2 + \epsilon + 0.5b] + M_{w,y}(t)}{P_r} \tag{C.1}$$

In the same way, the left tether force T_{inner} can be determined by taking the sum moments around the right tether anchorage point, not taking into account damping forces. This equation is presented in eq C.2.

$$T_{inner} = \frac{(F_b + F_{w,z}(t)) \times \left[-x(t) + s_0 + a - \gamma\right] + (F_{w,x}(t) + F_{cur,x}(t)) \times [h_2 + \epsilon + 0.5b] - M_{w,y}(t)}{P_l} \tag{C.2}$$

in which the linearized parameters P_r and P_l are defined by

$$P_r = \left[\sin(\alpha_T) + \cos(\alpha_T)\lambda\theta_2\right] \times (2s_0 + 2a - 2\gamma) \tag{C.3}$$

$$P_l = \left[\sin(\alpha_T) - \cos(\alpha_T)\lambda\theta_2\right] \times (2s_0 + 2a - 2\gamma) \tag{C.4}$$

The stabilizing moment due to the tether forces and the buoyancy force, with respect to the fixed rotation point, is elaborated in eq C.5. Please note that the tether forces are dependent on the wave-current forces. In other words, the stiffness of the system is affected by the presence of waves and current.

$$M_s = -x(t)F_b + 2P_R(T_{inner} + T_{outer}) \tag{C.5}$$

in which

$$P_R = \theta_2\lambda\sqrt{\left[s_0 + 2a - 2\gamma\right]^2 + \left[h_2 + \frac{h_2}{s_0}(a - \gamma)\right]^2} \tag{C.6}$$

C.2. Wave moment

The wave-current forces, which are determined in the wave force module, are attached to the tunnel body. This can be observed in figure C.1. All wave-current forces are transformed into one wave moment around the fixed rotation point. The wave moment with respect to the fixed rotation point is elaborated in eq C.7. This includes only the wave-current forces computed in the wave module.

$$M_w = x(t)(F_{w,z}(t) + z_R \times [F_{w,x}(t) + F_{cur,x}(t)] + M_{w,y}(t) \tag{C.7}$$

in which z_R is the vertical distance between the centre of gravity of the SFT and the fixed rotational point given by

$$z_R = \frac{h_2}{s_0}(a - \gamma) - \epsilon - \frac{1}{2}b \tag{C.8}$$

C.3. Equation of motion coupling module

The elaboration of eq B.14, gives the following equation of motion presented in eq C.9. A clarification of the EOM describing the oscillation of a SFT forced by waves and current is given in figure B.7.

$$\frac{d^2\theta_2}{dt^2}J + M_c + M_s = M_w \tag{C.9}$$

in which

J	=	Moment of inertia
M_c	=	Damping moment
M_s	=	Stabilizing moment dependent on external forcing
M_w	=	Wave moment

Please note that the damping moment, elaborated in appendix B section B.4, remains unchanged. The equation to determine the damping moment can be found in eq B.27.
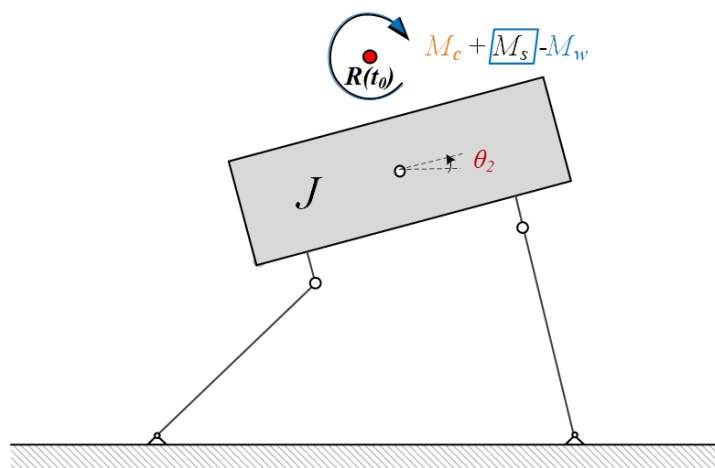
Figure C.2: Clarification of the EOM describing the oscillation of a SFT forced by waves and current.

D

Physical model experiments on SFT (Drost, 2019)

D.1. Model description

An experimental study on the hydrodynamics and kinematics of a submerged rectangular cylinder in a wave-current environment have been performed recently by Lisanne Drost in 2019. A part of this research will be used to validate the wave force module and the dynamic module.

The first part of the study consist of multiple flume experiments on a submerged rectangular cylinder subjected to a current, regular wave and combined wave-current environment. Several parameters are varied during the tests, these are shown in table D.1.

Table D.1: Parameters used in physical flume experiments (Drost, 2019).

Parameter	Symbol [Unit]	Values Tested	Model type
Model variables			
Tether angle	α_T [$\circ$]	30 70	tether
Submergence depth	s_1 [m]	0.00 0.175 0.35	tether + fixed
Environmental conditions			
Wave height	H [m]	0.02 0.08 0.12 0.16	tether + fixed
Wave period	T [s]	0.92 1.13 1.41 1.84	tether + fixed
Current velocity	u_c [m/s]	0.10 0.20 0.30 0.40	tether + fixed

In total three different flume set-ups were used presented in figure D.1. These are: A flume with passive wave absorber in combination with a wave generator to simulate regular waves, a flume with weir in combination with a current inflow and a flume with weir in combination with a wave generator and current inflow to simulate a wave-current environment.

The dimensions of the scale model set-up and specific information is shown in table D.2.

Table D.2: Model test dimensions and full scale indication. The buoyance to weight ratio (BWR) of the scale model is presented as well (Drost, 2019).

	Model Dimensions	Full scale indication
Width [m]	0.40	20
Height [m]	0.16	8
Length [m]	0.792	40
Max submerged floating tunnel (SFT) depth [m]	0.35	17.5
Weight [kg]	33.7	-
BWR	1.51	-

(a) Regular wave set-up

(b) Current set-up

(c) Combined wave-current set-up
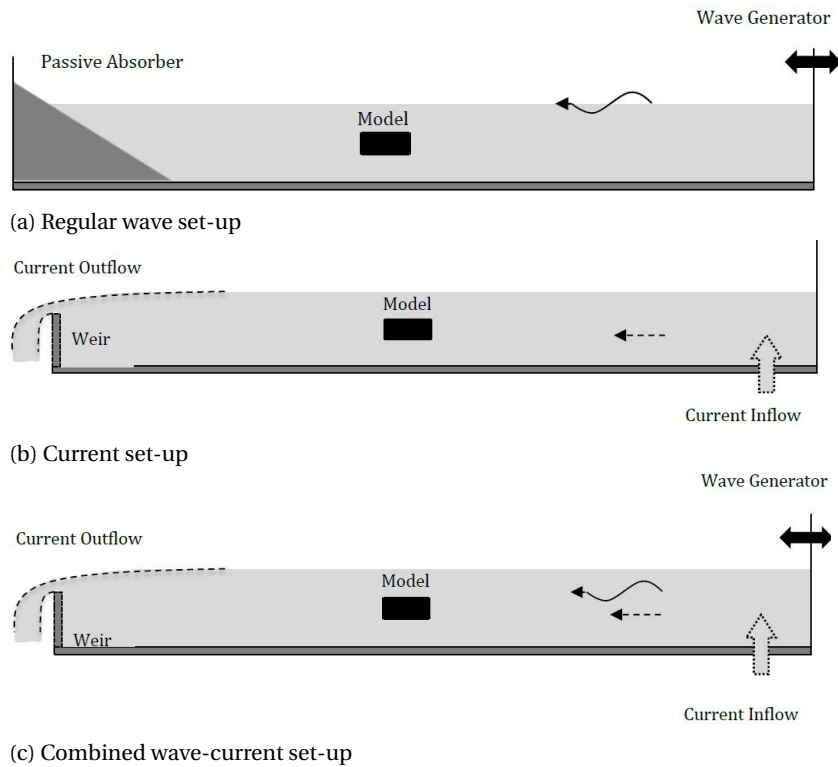
Figure D.1: 2D side view flume experiments set-up

D.2. Results

Combining all model variables to all environmental conditions leads to almost 1100 unique tests. A database is available containing the following information:

- Displacements
- Acceleration of tethers
- Tether forces
- Wave height in front and after SFT cross section
- Flow velocities in front of the SFT cross section

From these experiments, the Morison inertia and drag coefficients are determined and presented in D.3. These coefficients can be used to determine the forcing on the SFT model.

Table D.3: Morison inertia and drag coefficients (Drost, 2019).

Submerged depth	Regular Waves	Combined wave-current
Inertia (x and z)		
$d_s = 0.175$	$C_{Mx} = 0.794KC + 1.062$	$C_{Mx} = 1.21$
$d_s = 0.35$	$C_{Mx} = 1.095KC + 0.681$	$C_{Mx} = 1.21$
$d_s = 0.175$	$C_{Mz} = 3.818KC + 1.281$	$C_{Mz} = 2.68$
$d_s = 0.35$	$C_{Mz} = 2.079KC + 2.570$	$C_{Mz} = 2.68$
Drag (x and z)		
-	$C_{dx} = 1.18$	$C_{dx} = 1.18$
-	$C_{dz} = 2.30$	$C_{dz} = 2.30$

An impression of a flume tests for a tethered SFT is given in figure D.2. In this figure, three photos are made while a wave passes over the small scale SFT. The wave is moving from left to right. At the first time frame it can be observed that the crest of the wave moves the right side of the object downward. When the crest of the wave is at the middle of the object, it starts to tilt back to its 'equilibrium'. When the wave passes the left side of the object, the object is pushed down. Note that the wave breaks at the end.
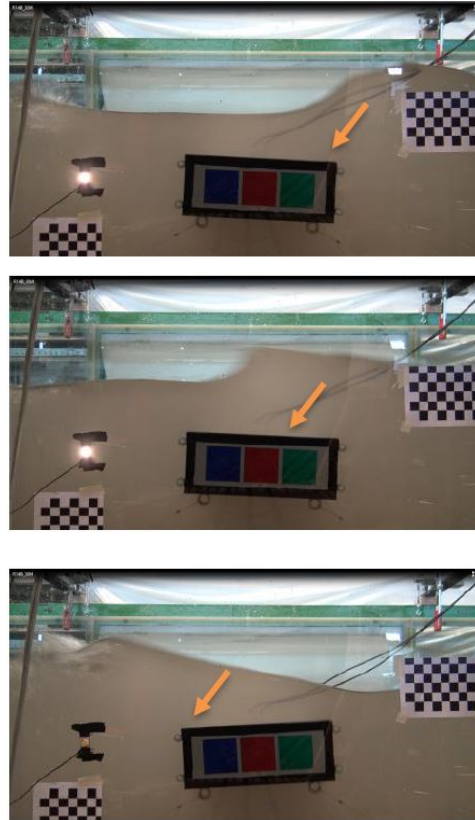
Figure D.2: Wave passing the SFT (from right to left). $T_{in} = 0.92s$, $H_{in} = 0.16s$, $\alpha_T = 30\circ$